Processing and Optical Engineering of Polymer-Fullerene Solar Cells Towards High Efficiency and Environmentally Friendly Fabrication for Real-Life Applications

Kung-Shih Chen

A dissertation
submitted in partial fulfillment of the
requirements for the degree of

Doctor of Philosophy

University of Washington
2014

Reading Committee:
Alex K-Y. Jen, Chair
Christine K. Luscombe
Marco Rolandi

Program Authorized to Offer Degree:
Materials Science and Engineering

University of Washington

Abstract

Processing and Optical Engineering of Polymer-Fullerene Solar Cells Towards High Efficiency and Environmentally Friendly Fabrication for Real-Life Applications

Kung-Shih Chen

Chair of the Supervisory Committee:
Chair & Boeing/Johnson Chair Professor Alex K-Y. Jen
Materials Science and Engineering

Facing the tremendous challenges of energy shortage and global warming, embracing renewable energies is an obvious choice and necessary action. Solar energy is arguably the most important source of renewable energy. Organic photovoltaics (OPV) has the potential to make the solar energy much more affordable. However, OPV technology is still relatively new and immature and requires substantial improvements on device performance, stability, fabrication, and many other aspects to make OPV actually useful. The studies described in this dissertation are aimed to address some of the critical challenges and provide ideas for future developments.

In chapters 1 and 2 the motivations and current developments of OPV research are briefly overviewed. In chapter 3, two high performance polymer:fullerene bulk-heterojunction solar cells used in the works of this dissertation are described. Chapter 4 describes our developments of a device processing approach that involves completely halogen-free solvents, which is desirable to achieve sustainable large-scale fabrication of OPV cells. The solvent system, consisting of small amount of a novel solvent additive 1-methylnaphthalene (Me-naph) in common halogen-free solvent matrix, can drastically improve phase-separated morphology of OPV devices to achieve efficient charge separation and yield high-performance.

In Chapter 5, OPV devices in a novel optical resonant cavity structure are systematically investigated. Such structure has exhibited several advantages: first, light trapping of thin film OPV devices can be boosted by carefully tuning the optical field in the resonant cavity. Second, replacing the typical transparent ITO electrode with semi-transparent TeO_2/Ag electrode simultaneously solves or ameliorates multiple problems associated with the ITO electrode such as high cost, brittleness, and limited conductance, making the cavity structure viable for making flexible and large-area device.

In Chapter 6, semi-transparent organic photovoltaic (OPV) cells with high device performance and tunable transparency are demonstrated. The devices not only possess high performance to transparency ratio but also close to perfect color rendering index (nearly 100), making it a strong candidate for power-generating window applications.

TABLE OF CONTENTS

LIST OF FIGURES

LIST OF TABLES

ACKNOWLEDGEMENTS

I would like to show my gratitude to people whom I worked with during my studying period here in the University of Washington. First, I would like to express my thanks to my advisor and dissertation committee chair, Prof. Alex Jen, for his guidance, constructive criticism, and financial support for the entire period of my study. I would like to thank Dr. Hin-Lap Yip and Dr. Steven Hau for their guidance and discussions on improving the quality of my research projects. I would like to acknowledge Prof. David Ginger, Dr. Cody Schlenker, and Dr. Michael Salvador from the Department of Chemistry for letting me work on their facilities and for providing professional discussions and collaboration opportunities.

I am also grateful to my colleagues Dr. Jingyu Zou, Dr. Kevin O'Malley, Dr. Orb Acton, Namchul Cho, Dr. Kirsty Leong, Dr. Pingyi Yang, Dr. Shang-Chieh Chien, Dr. José-Francisco Salinas, Dr. Chang-Zhi Li, Dr. Yunxiang Xu, Dr. Yong Zhang, Dr. Chu-Chen Chueh, Nathan Cernetics, Dr. Yen-Ju Cheng, Dr. Shane Boyd, Guy Ting, Dr. Su Huang, Dr. Jingdong Luo, Dr. Sei-Hum Jang, Dr. Hong Ma, Dr. Zhengwei Shi, Dr. Joshua Davies, Dr. Tae-Wook Kim, Dr. Zhongan Li, Kai Yao, Dr. Ying Wang, Dr. Chih-Yu Chang, You-Jung Cheng, Dr. Jeremy Intemann, Ying Sun, Yongxi Li, Xi Yang, Lijian Zuo, Dr. Jong Hyun Kim, Yue Zhang, Shengqiang Liu, Po-Wei Liang, Spencer Williams, Jeffrey Yang, and Ting Zhao for their professional and personal supports and assistance along the process of my Ph.D. study.

Thank my friends Bingyi Lin, Yu-Jung Chang, Joe Chang, Danny Huang, Mollie Ma, Emily Huang, Chi-Han Hsieh, Christina Wang, and Steven Wu, who have made my journey in Seattle much more joyful and meaningful. I would also like to thank my parents Chao-Wen Chen and Yen-Yun Chen and my sister Chien-Tung Chen for always giving me unconditional love and supports. Special thanks go to my girlfriend Rachel Hung. Her love, company, encouragements, and understanding are the strongest support for me throughout the entire process of graduate school.

Chapter 1. INTRODUCTION

1.1 MOTIVATION

Reliable energy supply has been an important support to the social and economic development. Since the Industrial Revolution the human energy demand has been continuously growing and currently reached 18 TW. **Figure 1-1** shows the makeup of current global energy supply. More than 80% of the energy supply is based on burning fossil fuels, 8% from hydropower, 6% from nuclear fission, and less than 3% from alternative energies. The demand is expected to keep increasing rapidly. By 2050 the energy demand is projected to reach 30TW due to the growing human population and the industrialization of the developing countries. Whether and how such enormous energy demand can be fulfilled will have drastic impact to the future of human beings and our ecosystem.

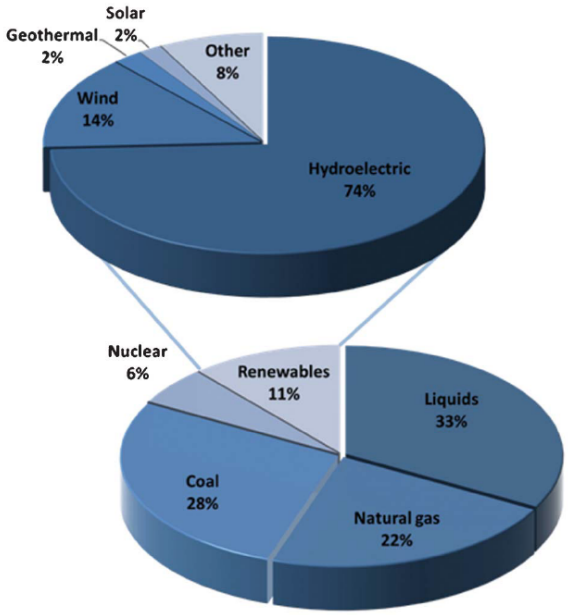

Figure 1-1. Global energy consumption breakdown by energy source in 2013 derived from the EIA reference case.[1]

Fossil fuels have always been the dominant energy source due to their low cost, high abundance, and long-term government subsidies. However, fossil fuels are limited resources that will eventually be depleted. Furthermore, the pollutants (e.g. SO_2, CO, NO_X, hydrocarbons, and CO_2) emitted from burning fossil fuels have been causing serious environmental problems. The worst threats among all pollutants are probably the greenhouse gases such as CO_2 and methane. The massive amount of greenhouse gases getting into the atmosphere can cause sea level elevation, global temperature rise, biodiversity decline, and destructive climate disruptions such as frequent drought, wild fire, storm, and flood. These potential damages are hidden costs of fossil fuels that we cannot further ignore.

Nuclear energy has the potential to satisfy much larger fraction of human energy demand while significantly reducing the generation of greenhouse gases, but the lack of secure and long-term means to store the high level radioactive wastes and the occurrences of disastrous nuclear accidents such as in Chernobyl and Fukushima have aroused serious concerns about expanding the use of nuclear power.

To meet the foreseeable energy demands and ensure environmental sustainability, timely shifting our high dependence on fossil fuels to renewable energies is absolutely vital. Among all energy sources, solar energy is the most abundant (23,000 TW), which largely exceeds the combination of all other renewable resources (**Figure 1-2**).[2] The following statement can help us to comprehend the ampleness of solar energy: “The amount of solar energy that falls on the earth’s surface in 40 minutes equals the total annual energy consumption of all the world’s people.” In other words, covering 2% of the land of the earth with 12% efficient solar conversion systems would provide 67 TW of power, which is more than twice of our 30 TW energy demand in year 2050. It is also estimated that the combination of the acquirable energy from hydropower,

wind, biomass, geothermal and ocean is probably below 10 TW, so solar energy is clearly essential for reducing our dependence on fossil fuels and nuclear energy and meet the growing energy demand.

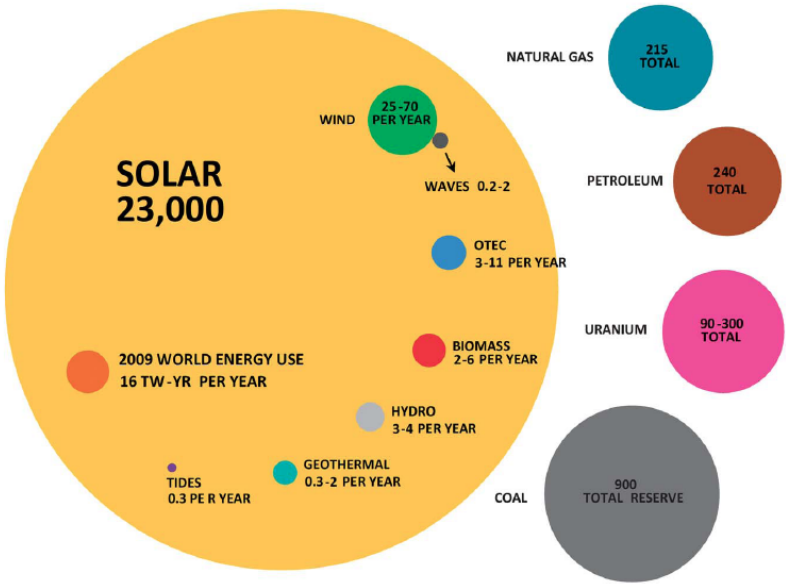

Figure 1-2. Comparison of non-renewable and renewable energy reserves in terawatt-years (TW-Yr). Total extractable reserves are shown for the non-renewable resources, and yearly potential is shown for the renewables.[2]

Solar energy can be transformed in several ways such as solar thermal (concentrated solar power and solar water and/or air heating), solar cells (photovoltaic), and solar fuels. Among all, photovoltaic (PV) is very attractive because of multiple advantages: (1) the operation is environmentally benign and does not involve generating noise, pollutants, or radioactivity. (2) No unexpected fuel cost and little maintenance requirement. (3) PV is modular and therefore ideal to serve any scale of demands. The organization of electricity generation can be highly flexible, e.g. stand-alone usage or connection to local/central grids. However, currently photovoltaics cost roughly 2 – 3 times higher than electricity generated from traditional fuels and

therefore occupy marginal market share (~0.2%) as revealed by **Figure 1-1**. Nevertheless, the PV market has been growing rapidly in a rate of 40% every year in the past decade.

From the discovery of photovoltaic effect in 1839 by Becquerel, various semiconducting materials have been applied for fabricating photovoltaic devices. Crystalline silicon (c-Si) solar cells, including monocrystalline silicon and polycrystalline silicon solar cells, are the most mature PV technology, partially attributed to the advance of the semiconductor electronics industry. Record monocrystalline silicon solar cells have reached about 90% of their theoretical Shockley-Queisser limit, and the module efficiency of c-Si cells is also among the leaders of the industry, which is approaching 23% power conversion efficiency.[3] Over 85% of the installed PV modules are currently based on by c-Si solar cells. In addition, silicon is the most abundant inorganic semiconductor, making c-Si solar cells realistic options for generating electricity in tens of TW capacity. However, silicon exists in the silica state rather than in elemental state in the earth crust, so the cost and the production rate of solar grade silicon feedstock is a challenge for c-Si solar cells. The second largest share of the PV market is the cadmium telluride (CdTe) thin film technology. CdTe solar cells rapidly capture ~13% of the PV market in the past few years due to the success in lowering manufacturing cost. However, tellurium is one of the least abundant elements in the earth's crust, which can seriously impacts the cost as well as the total attainable power generated by this technology.

Organic solar cells or organic photovoltaics (OPV) represent one of the new PV technologies. Due to the use of organic semiconductors, OPV features several advantages including abundant feedstock materials, low material consumption, lightweight (high power to weight ratio), flexible, low temperature processing, and compatible to high throughput, low cost, and environmental friendly fabrication. OPV has also been one of the fastest improved PV

technologies (**Figure 1-3**). However, for OPV technology to be useful for not just the niche applications, there are still tremendous challenges need to be conquered in various research aspects in order to improve the device performance and stability, reduce the cost, and realize modulization and up-scaling.

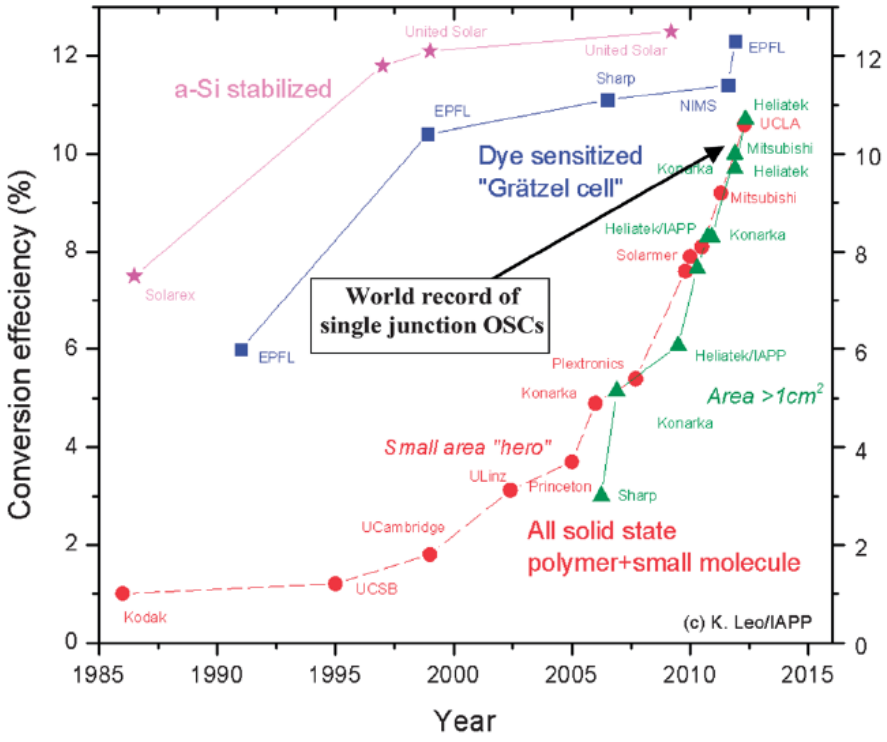

Figure 1-3. World records of organic solar cells (circles and triangles) and other thin-film PV technologies from 1985 to present [source of picture: http://www.orgworld.de].[4]

1.2 Dissertation Structure

In this dissertation, I focused on several aspects of OPV developments towards the realization of high efficiency, large-area, environmental benign, lightweight, and flexible organic solar cells. In Chapter 2, the working principles and developments of OPV devices are briefly overviewed. In Chapter 3, the properties and device characterizations of two semiconducting

polymers developed in the Jen group that are used in the works in this thesis are described. In Chapter 4, a novel and more environmental friendly solvent system for OPV device processing are introduced. Such halogen-free solvent systems incorporate a novel solvent additive that can drastically improve the morphology and device performance of the donor-acceptor blend. In Chapter 5, an ITO-free device architecture utilizing optical cavity to enhance light harvesting and device performance are discussed. The system uses an ITO-free bi-functional electrode that not only modulates the electric field within the device but also improve the conductance of the electrode, which can potentially be utilized the fabrication of large area device with lower translation loss. In Chapter 6, a highly efficient semitransparent OPV device with tunable shade and close to perfect color rendering properties is demonstrated. The demonstration of the high optical quality confirms the ideality of the semitransparent OPV device for the application of power generating tinted windows.

Chapter 2. INTRODUCTION TO POLYMER-FULLERENE BASED ORGANIC SOLAR CELLS

2.1 Basic Characterizations of a Photovoltaic Device

The performance of a solar cell can be determined by performing a current density-voltage (*J-V*) measurement under solar illumination. Typical *J-V* characteristics of a solar cell in the dark (blue line) and under illumination (red line) are shown in **Figure 2-1**. In the dark, the *J-V* curve shows rectifying behavior, i.e. current barely flows under negative or reversed bias and increases exponentially under positive or forward bias. Illumination on solar cells creates photocurrent and downshifts the *J-V* curve. The forth quadrant in **Figure 2-1** represents the power generation region because current flows in the direction opposite to the applied voltage bias. The maximum power density (P_{max}) extractable from a solar cell can be found at the maximum power point (MPP) where the product of V and J maximizes. The current density at zero bias (V = 0 V) is called short-circuit current density (J_{sc}). The intercept of the *J-V* curve with the *x*-axis is called the open-circuit voltage (V_{oc}), where the photocurrent cancels the dark current. Ideally, the *J-V* curve is perpendicular at $V = V_{oc}$, and the P_{max} equals to the product of the J_{sc} and the V_{oc} as represented by the area of the yellow rectangle in **Figure 2-1**. The *J-V* curves of real devices, however, deviate from perpendicularity and the P_{max}, which is represented by the area of the green rectangle in **Figure 2-1**, is always lower than the product of J_{sc} and V_{oc}. A measure of the ideality of a solar cell can thus be expressed by the ratio of the green rectangle to the yellow rectangle, which is known as fill factor (*FF*): $FF = V_{mpp} \times J_{mpp}/V_{oc} \times J_{sc}$.

Power conversion efficiency (PCE), which is the most important figure of merit on evaluating photovoltaic devices, is defined as the ratio of P_{max} to the intensity of the incident light power (P_{in}). The PCE can also be described by the equation with output parameters J_{sc}, V_{oc}, and *FF* as:

$$\mathrm{PCE} = \frac{\mathrm{P_{max}}}{\mathrm{P_{in}}} = \frac{V_{\mathrm{mpp}} \times J_{\mathrm{mpp}}}{\mathrm{P_{in}}} = \frac{V_{\mathrm{oc}} \times J_{\mathrm{sc}} \times \mathrm{FF}}{\mathrm{P_{in}}}$$

Since all the three output parameters J_{sc}, V_{oc}, and *FF* are proportional to PCE, the optimization of individual parameter often contributes to the overall increase of device performance.

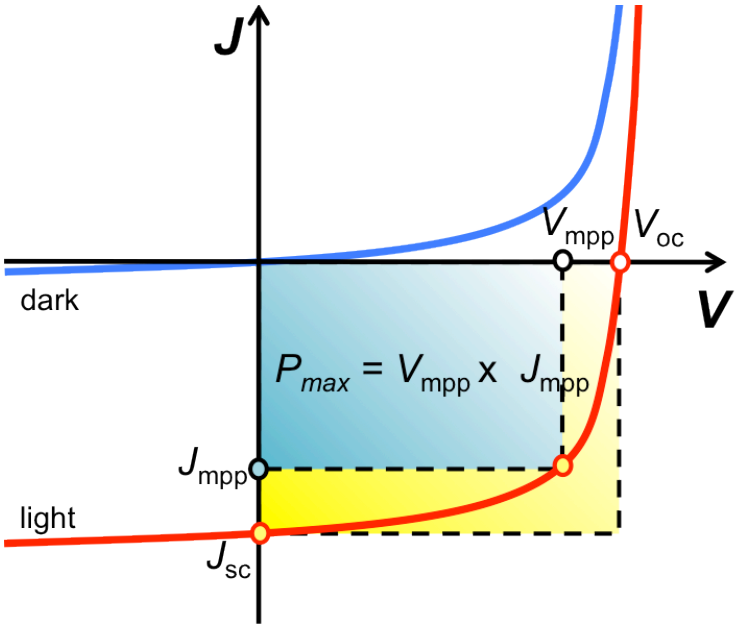

Figure 2-1. Typical current-voltage characteristics of solar cells in dark and under illumination.

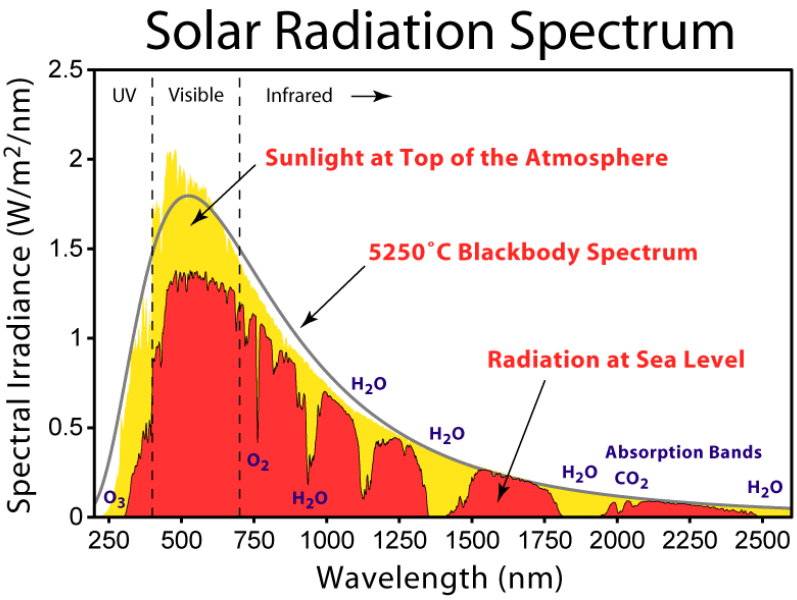

Figure 2-2. Solar radiation spectrum. [source of figure: http://en.wikipedia.org/wiki/Air_mass_%28solar_energy%29#mediaviewer/File:Solar_Spectrum.png]

The *J-V* testing of a solar cell is often measured under real sunlight or certain simulated solar illuminations. The sun emits radiation at all frequencies and the solar spectrum is close the black body radiation at temperature ~ 5,250 K as shown in **Figure 2-2**. The multiple dips in the near infrared region of the solar radiation curve measured at sea level are from absorptions of the air (e.g. O_2 and H_2O). Depending on the zenith angle of the sun (**Figure 2-3**), the solar radiation spectrum changes accordingly due to the change of atmosphere absorption path length. Therefore, the solar irradiance spectrum at a specific zenith angle can be represented by the AM number, which is defined by the ratio of the path length at the zenith angle (P) to the zenith path length (P_0), where AM = P/Po ≈ sec θ_z, and θ_z is the zenith angle in degrees. For example, the commonly used standard AM 1.5 spectrum represents the solar radiation at zenith angle of 48.2°.

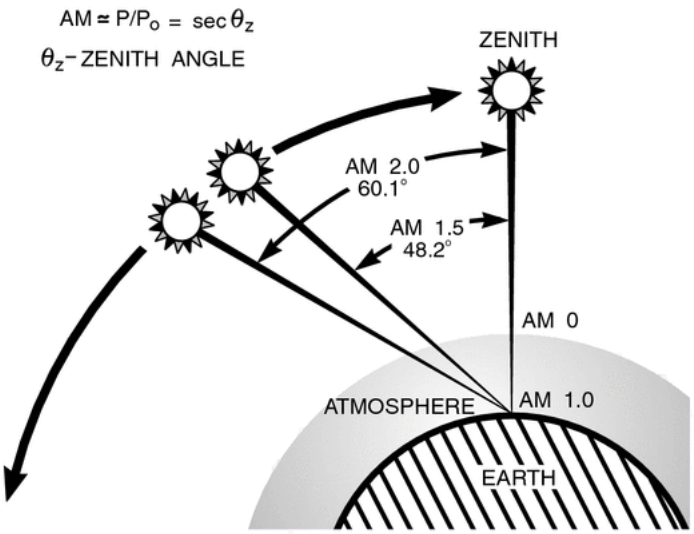

Figure 2-3. The path length in units of Air Mass, changes with the zenith angle. [source of figure: http://www.newport.com/Introduction-to-Solar-Radiation/411919/1033/content.aspx]

Besides PCE, external quantum efficiency (EQE) and internal quantum efficiency (IQE) are important figures of merit for solar cells. EQE is a spectral measurement of the ratio of the output electrons to the input photons at specific wavelength, which can be expressed as:

$$EQE(\lambda) = \frac{number\ of\ collectd\ electrons/sec}{number\ of\ incident\ photons/sec} \times 100\ \% = \frac{hc}{q}\frac{J_{sc}(\lambda)}{\lambda \cdot P_{in}(\lambda)}$$

where λ is the wavelength of interest, h is the Planck's constant, c is the speed of light, q is the elementary charge, $J_{sc}(\lambda)$ is the short-circuit current density, and $P_{in}(\lambda)$ is the incident power density. Therefore, J_{sc} and EQE are correlated by the equation:

$$J_{sc} = \frac{q}{hc}\int P_{in}(\lambda) \cdot EQE(\lambda) \cdot \lambda \cdot d\lambda$$

The internal quantum efficiency (IQE) equals to EQE normalized by the number of photons absorbed within the active layer as:

$$IQE(\lambda) = \frac{number\ of\ collectd\ electrons/sec}{number\ of\ absorbed\ photons/sec} \times 100\ \% = EQE(\lambda)/Abs_{AL}(\lambda)$$

with $Abs_{AL}(\lambda)$ being the ratio of absorbed photons in the active layer.

2.2 FUNDAMENTALS OF ORGANIC SOLAR CELLS

2.2.1 *Introduction of Organic Semiconductors*

The semiconducting properties of the conjugated organic materials come from the alternation of single and double carbon-carbon bonds. Each carbon atom is bound with three neighboring atoms and leaves one electron in its p_z orbital. These p_z orbitals mutually overlap and form π bonds. The conjugation of the π bonds allows electrons to delocalize over the backbone, giving the electric conductivity to the conjugated molecule. Charges transport via hopping process between the conjugated molecules. Due to the lack of long-range order structure and limited intermolecular overlap, charge carrier mobility of organic semiconductors is several orders lower than their inorganic counterparts. Hence, organic semiconductors are not the best choices for high speed applications but more suitable for applications where their strengths like ease of processing and flexibility matter the most. Another important distinction between organic and inorganic semiconductors is their dielectric properties. Organic conjugated molecules are also known for relatively low dielectric constants (generally ~3-4) compared with inorganic semiconductors. As a result, electrically neutral excited states called excitons generated in organic semiconductors upon photo-excitation cannot be readily dissociated into free charge carriers due to poor charge screening and thus large exciton binding energy (hundreds of meV). These fundamental differences between organic and inorganic semiconductors thus have significantly affected the design of organic solar cells.

2.2.2 *Donor-Acceptor Heterojunction*

In order to efficiently dissociate excitons and generate photocurrents, organic solar cells often employ two photoactive semiconductors that differ in electron donating and accepting properties. The energy difference between the two semiconductors promotes photo-induced charge transfer at the heterojunction interface to overcome the high exciton binding energy. **Figure 2-4** explains the complete charge dissociation process at the presence of the energy offset of the heterojunction: (1) an exciton is created upon light absorption. (2) The exciton diffuses to the donor/acceptor interface of the two components where charge transfer takes place. (3) The electron is transferred to the material with the larger electron affinity, or the hole is transferred to the material with the lower ionization potential. The electron and hole across the interface can still bound strongly as a geminate pair until dissociating into free carriers. (4) Once geminate pairs are dissociated, charges can transport freely in respective phases and (5) get collected by separate electrodes. From exciton generation till charges collection at electrodes, energy may be lost during each of the aforementioned process. For example, absorption loss may occur due to limitations of the bandgap and low thickness of the active layer. Excitons can decay before charge transfer if created too far from the heterojunction interface. Geminate pairs and free charge carriers can also decay through geminate and bimolecular recombination, respectively. Therefore, the optimization of organic solar cells depends on understanding and prevention of these losses.

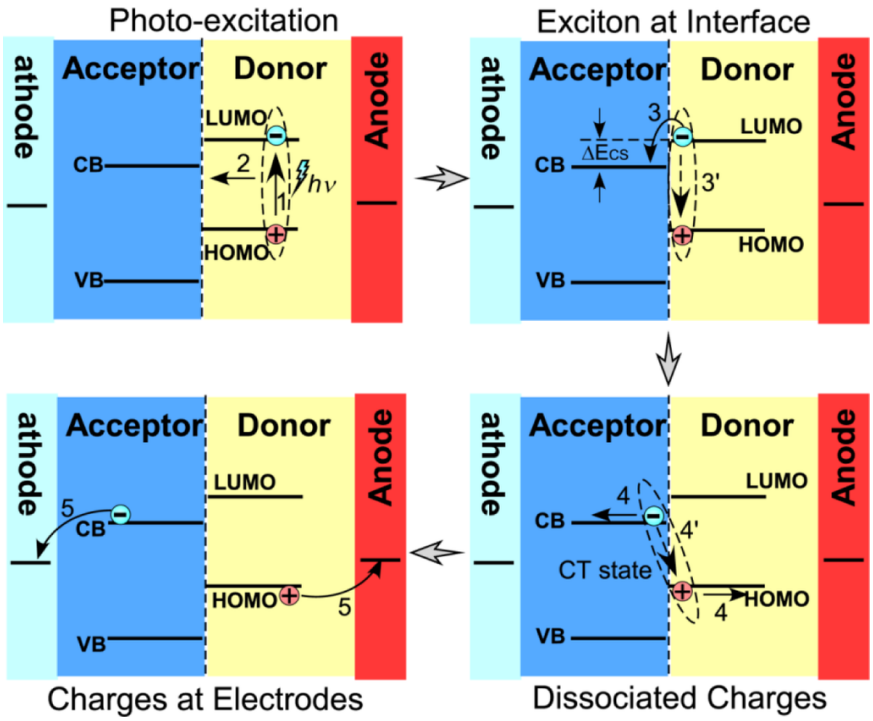

Figure 2-4. Charge separation process at the donor-acceptor heterojunction interface.[5]

The first donor-acceptor heterojunction device utilized the donor and acceptor in a bilayer structure known as the planar heterojunction (**Figure 2-5**).[6] The OPV devices in this structure presented significantly enhanced photocurrent and *FF* compared with the previous devices made of single organic semiconductor owing to improved exciton dissociation by the heterojunction interface. However, the bilayer arrangement of donor and acceptor is not ideal because excitons in organic semiconductors suffer from rather short diffusion length (L_D) of ~ 10 nm, and those excitons generated farther away from the planar interface than the L_D will decay and not contribute to the photocurrent. Therefore, the effective thickness of the active layer in planar heterojunction device that actually generates free charge carriers is restricted to L_D on each side of the planar heterojunction, which seriously limits the device performance. To overcome the limitation of short exciton diffusion length, a new design called bulk-heterojunction[7,8] (BHJ,

Figure 2-5) was developed. In BHJ device, donor and acceptor materials are still used to dissociate the excitons at the interface, but the two components are dissolved and cast together from one matrix to form interpenetrating mixture with large interface area. The well mixing of the donor and acceptor of BHJ produces randomly distributed interface inside the active layer. Therefore, excitons generated everywhere in the bulk can dissociate at heterojunction interface in vicinity, which drastically increases the effective thickness of the active layer and the device performance. The invention of bulk-heterojunction also facilitates the transition to solution processing of organic solar cells, which is appealing for cheaper and more energy effective manufacturing processes. Solution processing of a planar heterojunction is typically challenging because the deposition of the second organic layer can destroy the former layer. In bulk heterojunctions, donors and acceptors are laid down together and thus the processing difficulties are prevented.

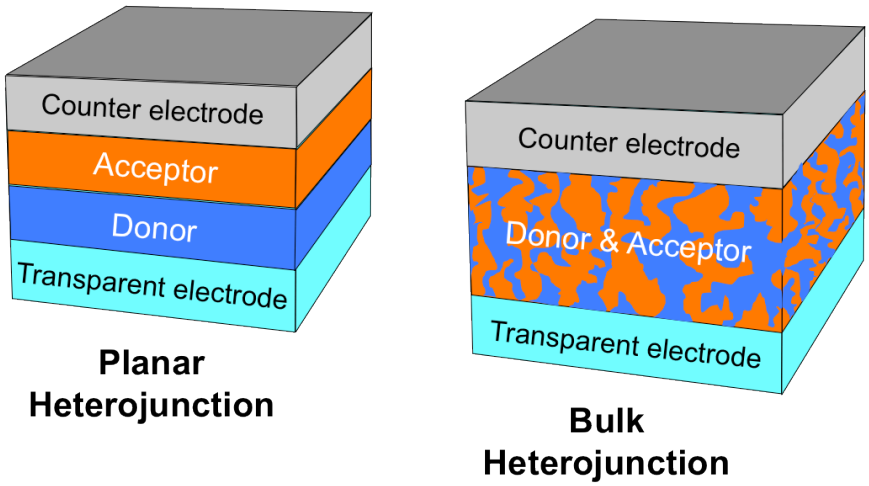

Figure 2-5. Schematics of the basic structures of planar heterojunction and bulk heterojunction organic solar cells.

2.3 POLYMER:FULLERENE BHJ SOLAR CELLS – MATERIAL DEVELOPMENTS

Because most of the charge generation processes (light harvesting, exciton dissociation, and charge transport) take place in the photoactive materials, the developments of both organic semiconducting donors and acceptors with improved optical and electrical properties are central of the advance in OPV devices. In this thesis, we focus on the donor-acceptor BHJ devices made of semiconducting polymers and fullerene derivatives. Various electron acceptors have also been actively developed and applied in organic BHJ devices including small organic molecules[9-15] and polymers.[16,17] Among all materials, devices made of fullerenes and their derivatives have shown the most outstanding performance. Fullerenes are good n-type organic semiconductors with isotropic charge transport properties due to their three-dimensional conjugated structures and tendency to form crystals. It was also found that charge transfer between semiconducting polymers and buckminsterfullerene was extremely efficient.[18] However, applications of fullerenes without functionalization (e.g. C60) in OPV devices are limited due to their poor solubility. A highly soluble C_{60} derivative phenyl-C61-butyric acid methyl ester ($PC_{61}BM$,[7] **Table 2-1**) and its C_{70} derivative ($PC_{71}BM$, **Table 2-1**) have been the workhorses for OPV devices. The lower symmetry of C_{70} allows more efficient optical transition compared to C_{60}, giving $PC_{71}BM$ advantage to absorb more light. $PC_{61}BM$ and $PC_{71}BM$ have been used as the electron acceptor in most record-breaking OPV devices. Many other solution processable fullerene derivatives have also been developed and exhibited good performance.[14] One design concept is to create higher fullerene adducts such as $IC_{60}BA$[19] and bis-$PC_{60}BM$[20] (**Table 2-1**). The elevated LUMO levels of the higher fullerene adducts can improve V_{oc} for OPV devices.

Table 2-1. Representative fullerene-based acceptors for OPV devices.

Molecular structure and Abbreviation	Name	LUMO level (eV)	HOMO level (eV)
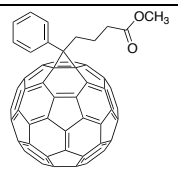 $PC_{61}BM$	[6,6]-phenyl-C61-butyric acid methyl ester	-3.91,[21,22] -4.2,[23] -3.8[20]	-6.0,[23] -5.93[22]
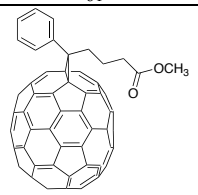 $PC_{71}BM$	[6,6]-phenyl-C71-butyric acid methyl ester	-3.91[22]	-5.87[22]
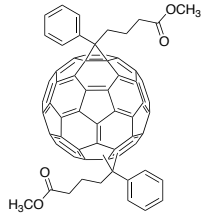 Bis-$PC_{61}BM$	bis(1-[3-(methoxycarbonyl)propyl]-1-phenyl)-[6.6]C62	-3.7[20]	
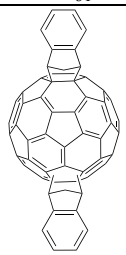 $IC_{60}BA$	Indene-C60 bisadduct	-3.74,[21] -4.0[23]	-5.9[23]
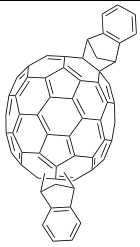 $IC_{70}BA$	Indene-C70 bisadduct	-3.72[22]	-5.61[22]

Table 2-2. Representative semiconducting polymers for OPV devices.

	Name	Bandgap (eV)
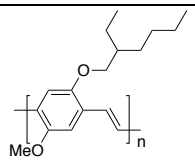 MEH-PPV	Poly[2-methoxy-5-(2-ethylhexyloxy)-1,4-phenylenevinylene]	~2.4
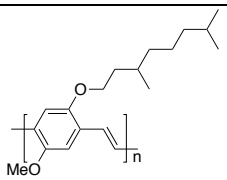 MDMO-PPV	Poly[2-methoxy-5-(3′,7′-dimethyloctyloxy)-1,4-phenylenevinylene]	~2.2
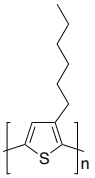 P3HT	Poly(3-hexylthiophene)	~1.9
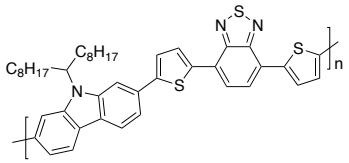 PCDTBT	Poly[N-9′-heptadecanyl-2,7-carbazole-alt-5,5-(4′-7′-di-2-thienyl-2′,1′,3′-benzothiadiazole)	~1.9
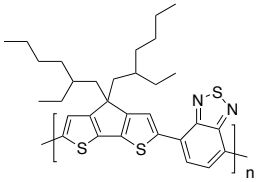 PCPDTBT	Poly[2,6-(4,4-bis-(2-ethylhexyl)-4*H*-cyclopenta[2,1-b;3,4-b′]-dithiophene)-alt-4,7-(2,1,3-benzothiadiadiazole)]	~1.5
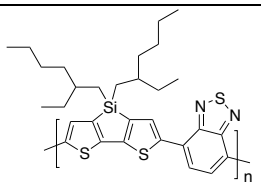 PSBTBT	Poly[(4,4'-bis(2-ethylhexyl)dithieno[3,2-*b*:2′,3′-*d*]silole)-2,6-diyl-alt-(4,7-bis(2-thienyl)-2,1,3-benzothiadiazole)-5,5′-diyl]	~1.5

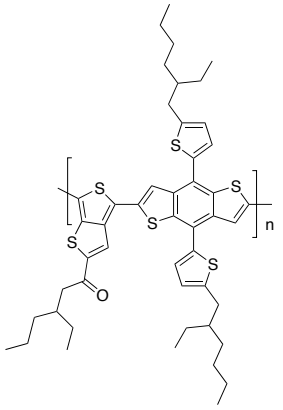 PBDTTT-C-T	Poly{[4,8-bis-(2-ethyl-hexyl-thiophene-5-yl)-benzo[1,2-b : 4,5-b']dithiophene-2,6-diyl]-alt-[2-(2'-ethyl-hexanoyl)- thieno[3,4-b]thiophen-4,6-diyl]}	~1.7
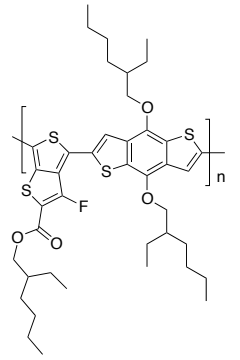 PTB7	Poly{4,8-bis[(2-ethylhexyl)oxy]benzo[1,2-b :4,5-b']dithiophene-2,6-diyl-alt-3-fluoro-2-[(2-ethylhexyl)carbonyl]thieno[3,4-b]thiophene-4,6-diyl}	~1.8
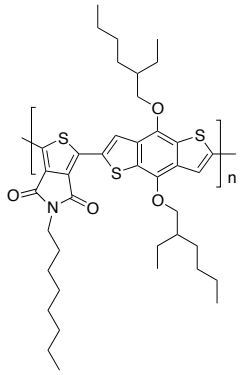 PBDTTPD[24]	Poly{4,8-bis[(2-ethylhexyl)oxy]benzo[1,2-b :4,5-b']dithiophene-2,6-diyl-alt-(1,3-(5-octyl-4H-thieno[3,4-c]pyrrole-4,6(5H)-dione))}	~1.8

Versatile electron donating π-conjugated molecules,[25,26] and polymers[27-30] are also vigorously developed for the OPV application. Semiconducting polymers are particular attractive because it can be processed in solution and can reach the state-of-the-art device performance. Several representative semiconducting polymers and their properties are summarized in **Table 2-2**. At the early stage, only few number of milestone polymers were the focus of research. For

example, *para*-phenylene vinylene (PPV) based polymers (e.g. MEH-PPV[18] and MDMO-PPV[31]) are among the earliest polymers used in BHJ solar cells, which exhibited PCE > 3%[32-34] after morphology optimizations.[35] Polythiophenes, especially regioregular poly(3-hexylthiphene) (P3HT),[36] later replaced the PPV-based polymers as the prototypical polymer because of their improved charge transport properties and absorption coverage. PCE ~ 4% was consistently demonstrated from the optimized P3HT:$PC_{61}BM$ BHJ devices. Thorough studies on the BHJ blends of these prototypical conjugated polymers helped to establish the fundamental knowledge on the correlations of material properties and processing techniques to the performance of OPV devices.[37-39] In recent years, many more high performance polymers incorporating fused heterocycle units were developed. These polymers were designed towards lower bandgap, higher V_{oc}, and better charge mobility for higher device performance. For example, PCDTBT was one of the record-breaking polymers. PCE of 6.1% and IQE approaching 100% were reported by Park *et al.*[40] based on the mixture of PCDTBT and $PC_{71}BM$. PCPDTBT[41,42] and its silicon-substituted analogue PSBTBT[43] are popular small bandgap polymers, both of which showed extended absorption spectrum to nearly 900 nm and high mobility. Mixtures of PCPDTBT and PSBTBT with $PC_{71}BM$, respectively, have reached PCE > 5%. PTB7[44] and its analogues[24,45-47] incorporating benzodithiophene units are another class of polymers that have shown great properties of light collection, charge transport, and high photovoltage, which in combination lead to PCE of 7 - 9 %.[44,48]

2.4 Control of the Photoactive Layer Morphology

The control of the phase separation and distribution of the polymer and fullerene components in bulk-heterojunction is one of the most critical factors dictating the device performance. Because charges dissociation takes place at the donor/acceptor interface, efficient current

generation depends highly on the interface area and continuity of charge transport paths, and thus the spatial dimensions of the donor and acceptor phases have to be optimized to balance between charge separation and charge transport. More homogeneous mixing of the donor and acceptor phases result in higher interface area that facilitates exciton dissociation; phase separation into coarser grains, on the other hand, can enhance intergrain connectivity and improve charge transport. The ideal length scale of at least one of the dimensions of the phase-separated domains should be comparable to the exciton diffusion length (~10–20 nm) to prevent exciton relaxation while maintaining continuous paths for charges to transport to the electrodes. Figuring out how to obtain this ideal phase distribution of the active layer has thus been a strong interest of research.

For solution-processed BHJ layer, the tuning of several processing parameters have been found essential in controlling the active layer morphology during film drying such as the donor and acceptor solubility and concentrations in the solution, solvent viscosity and volatility, and post-deposition treatments such as thermal or solvent vapor annealing.[49-51] In this section the developments of device processing procedures are briefly introduced.

2.4.1 *Effects of Solvents on Morphology*

The solubility of the active materials in the solvents and the volatility of the casting solvent determine their retention time in solution before precipitating into solid-state. A good example is the MDMO-PPV:PCBM solar cells, of which the active layer morphology changed drastically when the casting solvent of the active layer was replaced from toluene to *ortho*-dichlorobenzene (*o*-DCB), leading to a three-time increment on PCE ascribing to reduced domain dimensions and thus increased interface area between the polymer and the fullerene. The correlation between device performance and the processing solvent is also studied comprehensively for the

prototypical P3HT/PCBM system and the best solvents are chlorobenzene and (*o*-DCB).[36] When P3HT/PCM is processed from a higher boiling point solvent like dichlorobenzene, the longer drying time allow the semicrystalline polymer P3HT to reorganize and form more ordered structure.

2.4.2 *Effects of Post-Fabrication Treatments*

Thermal annealing has been a widely used method for optimizing the morphology of OPV devices. The high temperature promotes diffusion and crystallization of both components in the BHJ blend,[52] resulting in coarsened domains as well as increased molecular order that contribute to improved charge transport. Thermal annealing is more effective with polymers that demonstrate crystalline order such as P3HT.[50,53] It was observed that the efficiency of a P3HT:$PC_{61}BM$ solar cell increased from < 1% to ~ 5% after the film is annealed at 150 °C for 30 minutes.[54] Phase contrast transmission electron microscopy (TEM) and small-angle neutron scattering (SANS)[55] reveals that prior to annealing phase segregation between the P3HT and PCBM domains is not apparent, but crystallinity for both P3HT and PCBM phases is increased after thermal annealing. A fibrillar feature with dimension of ~ 10 – 20 nm consisting of P3HT lamellae was also observed upon thermal annealing.[54,56]

Solvent annealing, or slow drying, is another common post-fabrication treatment that provides similar control over the active layer morphology as thermal annealing. By using slightly higher boiling point solvents and stopping the spin-coating process early before solvent evaporates completely, the photoactive materials can gain more time to reorganize until the morphology evolution finalizes. Sometimes optimal condition requires storing devices in enclosed containers with saturated solvent vapor to extend the reorganization time. Solvent annealing results in enhanced structural order[57,58] and mobility[59] of the polymer and fullerene

and thus improve device performance, e.g. DCB vapor treatment increased the crystallization of P3HT, which lead to enhanced absorption, hole mobility, and PCEs of 4.4%.[52]

2.4.3 *Using Solvent Additives*

Another powerful method to control the nanoscale phase separation is through the addition of high boiling point solvent additives to the solvent matrix.[60,61] Small amount of high boiling point solvent additive can change the drying kinetics of film formation. This technique is particularly attractive for systems that thermal and vapor annealing do not work effectively such as the case for PCPDTBT:$PC_{71}BM$ blends.[41] These solvent additives usually possess high boiling point and selectively dissolve the fullerene derivative.[62] For example, the high boiling point additives octanedithiol (ODT) and diiodooctane (DIO) are poor solvent for P3HT[63] and PCPDTBT.[41,64] Their late evaporation degrades the solvent quality for the polymers during drying process of the BHJ mixtures and forces the polymers to aggregate and crystalize, which consequently enhances phase-separation and improve device performance. In the case of the high-efficiency PTB7:$PC_{71}BM$ mixtures, DIO selectively dissolves $PC_{71}BM$ aggregates and suppresses oversize phase separation, leading to significant PCE improvement.[65]

The aforementioned ways of device processing allow sophisticate controls over the degree of phase separation for various active materials and combinations to form the required bi-continuous nanocrystalline domains.

2.5 Developments in Device Configurations

In addition to the photoactive layer, polymeric solar cells are made of several other key functional layers including the transparent electrode, the counter electrode, and the interfacial charge transport layers. The performance of OPV devices relies on proper material selection and optimization for each of these layers, and some of their developments are discussed here.

2.5.1 *Transparent Conductive Electrodes*

Indium tin oxide (ITO) has been the most popular transparent conducting material that is extensively utilized in all kinds of optoelectronic devices. The good transparency (T > 90%) and low resistance ($\rho \sim 10^{-4}$ Ω cm, sheet resistance 10 Ω/□) of ITO have set a high standard for other transparent conducting materials to compete with. However, ITO also has several unfavorable characteristics such as the brittleness, high cost, high energy-consumption, and high temperature processing. ITO represents the most expensive part among all components in an OPV device.[66] In addition, ITO is not a suitable top electrode for organic electronics because the organic layers are vulnerable to the harsh ITO sputtering condition and high temperature post ITO deposition annealing. All these flaws make ITO not the ideal material for low-cost and flexible applications. Therefore, finding ITO replacement is an important objective for the development of organic solar cells, and many potential alternatives of ITO are being developed.

The solution processed conducting polymer poly(3,4-ethylenedioxythiophene) (PEDOT), stabilized and doped with poly(styrenesulphonate) (PSS) is a well studied and a popular transparent conducting material for optoelectronic applications due to its excellent transparency at visible wavelengths.[67] The polymeric conductor is flexible and suitable for plastic substrates. High conductivity close to 10^3 S cm^{-1} has been demonstrated from PEDOT:PSS treated with secondary dopants or additives such as sorbitols, alcohols, dimethyl sulfoxide, and diethylene glycol.[68] However, the electrical stability is a challenge for the highly conductive PEDOT:PSS. The conductivity of PEDOT:PSS films decreases upon exposure to heat, UV radiation, and humidity.

Optically thin metal films composed of single or multiple metal layers are potential ITO alternatives. Thin metal electrodes can be flexible and inexpensive. The transparency of thin metal films is usually inferior to ITO due to the considerable absorption and reflection of metals.

Reducing the film thickness can improve the transparency at the expense of higher resistance. Metal film cannot be infinitely thin because it becomes discontinuous when the thickness is below their coalescence threshold, which is determined by several factors such as the surface energy and temperature of the underlying layer and the rate of vacuum deposition.

Another strategy to use metal as the transparent electrode is by creating patterned metal grids. The transmittance and conductance of the metal grid can be adjusted by controlling the thickness and width of the metal strips and the spacing between the strips. Large area imprinting of patterned metal grids can be realized through roll-to-roll or roll-t-plate printing,[69] and metal grids made of Cu, Au, and Ag with transmittance and sheet resistance only slightly inferior to ITO have be demonstrated.[70] However, the surface roughness of the patterned metal grid can be a challenge for its application in OPV devices.

Network of metal nanowires are also promising for transparent conducting electrodes, which can be manufactured with low-cost solution-deposited techniques such as roll-to-roll printing. Random network of metal nanowires have exhibited excellent optical and electrical properties comparable to standard ITO electrode.[71] Brabec *et al.* have demonstrated semitransparent device based on P3HT:$PC_{61}BM$ blend using spray-deposited silver nanowires as top electrode.[72,73] The spray-coated Ag NW layers exhibited excellent electrical and optical properties of a sheet resistance of approximately < 10 Ω/□ and an average transmission of over 85% between 400–800 nm, respectively. However, the roughness of the film is a concern for its use as bottom electrode for OPV devices.

Graphene is also a novel and promising transparent conductor that has attracted a lot of research devotion [ref]. Chemical vapor deposition (CVD) is an effective method in fabricating homogenous single- or multi-layer graphene sheets up to tens of inches. Graphene layers made

by CVD can be transferred through gentle lamination process. Multi-layer graphene sheets with sheet resistance as low as 30 Ω/□ with transmittance of 90% have been demonstrated.[74] However, high speeds and large area fabrication and patterning are still challenges.

2.5.2 *Counter Electrode and Interfacial Layers*

The counter electrodes of OPV devices are generally made of metal electrodes due to their good reflectivity and high conductivity. Metal electrodes can be deposited through vacuum deposition techniques or printed from inks containing dispersed metal particles. Metal electrodes and interfacial charge transport layers are both important in determining the energy barrier for charge extraction and maximizing V_{oc} of OPV devices.[75-79] The interfacial layers, or interlayer, also provide several crucial functions including forming charge selectivity, prevention of diffusion and reaction between the electrode material and polymer, determination of the charge collection polarity, and modulation of the optical field as an optical spacer.

The interlayers can be made of many different materials.[77-80] High bandgap transparent semiconductors such as transition metal oxides can selectively transport one type of charge carrier while blocking the extraction for the opposite type. ZnO[81-85] and TiO_2[86-90] are two n-type semiconductors that are often used as the electron transport interlayer between the cathode and the photoactive layer. P-type metal oxides[61,85,91-97] such as MoO_3, WO_3, V_2O_5, and NiO can be used as the anode interlayer for hole transporting and electron blocking. Besides metal oxides, solution processable conducting polymers, especially poly(styrene sulfonate)-doped poly(ethylene-dioxythiophene) (PEDOT:PSS), are among one of the most popular and earliest used anode interlayers.[31] Its low work function usually forms good ohmic contact with ITO, and it can also planarize the rough ITO surface. However, disadvantage of PEDOT:PSS include poor charge selectivity and intrinsic acidity, which can cause device degradations. Crosslinkable

charge-transporting molecules[98-102] are also possible interlayers. These materials can be thermally or photochemically crosslinked to form robust charge-transporting films with improved solvent resistance for subsequent processing of other layers. Their energy levels and charge mobility can be tuned by rational molecular design. Another class of interlayers creates surface dipole to modify the work function of the metal electrodes. These dipole layers can be salts (e.g. LiF,[32,103,104] and Cs_2CO_3[105,106]), polymer electrolytes,[107-109] and other polar molecules.[76,110-116]

Because the active layer thickness of OPV device is typically limited to < 200 nm due to the relatively low charge mobility of organic semiconductors, interference becomes important in determining the strengths and phases of standing waves formed inside the device, which has significant effects on device performance. The transparent interfacial layer can work as optical spacer by tuning its thickness and refractive index to modulate the distribution of the electric field and maximize the absorption. It was demonstrated that tuning the thickness of ZnO[83] or TiO_2[117] as the optical spacer for a few tens of nm can significantly improves the absorption.

2.5.3 *Conventional and Inverted Configurations*

A conventional OPV device has configuration shown in **Figure 2-6**. In such configuration, holes generated from the photoactive layer are collected from the bottom electrode and electrons exist from the top electrode. Metals with low work-function are commonly used for the counter electrode to collect electrons. Unfortunately, low work-function metals are generally prone to oxidation and cause device performance reduction. Therefore, interfacial layers with permanent dipoles have been applied to modify the work function of the metal electrode so more chemically stable metals can be used as the cathode.[109,115,116]

Another way to prevent the use of low work-function metals is by reversing the polarity of charge collection in OPV devices. The electrical polarity of an OPV device is controlled by the arrangement of its composing layers. Thus, the polarity can be inverted by reversing the sequence of the hole and electron transport layers and use high work-function metals as the counter electrode for ohmic contact (**Figure 2-6**).[82] Such inverted configuration is known to have several advantages over the conventional configuration such as improved stability and compatibility to roll-to-roll processes.[84,118-121] The inverted geometry can also avoid using PEDOT:PSS at the ITO interface, which is known to degrade performance due to chemical instabilities of ITO under acidic environment. OPV devices adopting the inverted structure have demonstrated much improved stability compared with the conventional devices with low work-function counter electrode.[84]

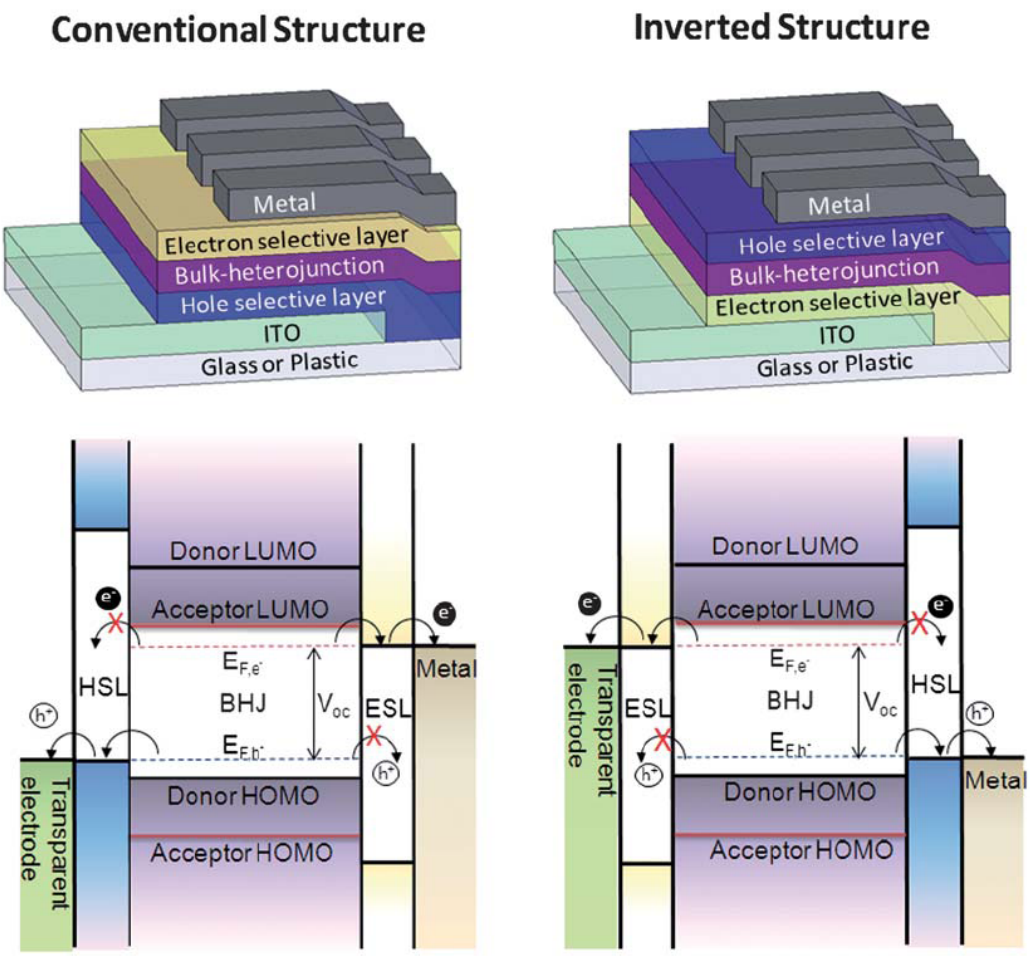

Figure 2-6. Schematics of device structures and energy level diagrams of conventional and inverted organic solar cells.

2.5.4 *Multi-Junction Organic Solar Cells*

Building multi-junction (tandem) device, which has two or more single-junctions or subcells stacked together, is a way to increase the limit of solar cells by minimizing thermal relaxation loss through capturing high and low energy photons using absorber materials with different bandgaps. OPV devices, in particular, can benefit from adopting the tandem structure. Organic semiconductors are known for their relatively narrow absorption bands compared with their inorganic counterparts due to weak intermolecular coupling; thus a single junction device made of organic semiconductors may absorb only a portion of the broad solar spectrum. Stacking

subcells with complementary absorption to build tandem device not only reduce thermal relaxation loss but also can improve the coverage of solar spectrum for OPV devices.

In a tandem OPV device, either the V_{oc} and J_{sc} is to be enhanced by connecting the subcells in series or parallel connection,[122] respectively. In the case of series connection, two or more subcells with matched photocurrent are connected to prevent space charge accumulation that can decrease device performance. For tandem cell in parallel connection, each subcell should have equal V_{oc} to prevent shunting. The fabrication of tandem OPV cells typically requires more complex processing steps and optical management,[123] yet many tandem devices using high efficiency organic semiconductors have been demonstrated.[4,124-127] Currently, the best record of tandem OPV device has reached over 10% PCE (**Figure 2-7**).[128]

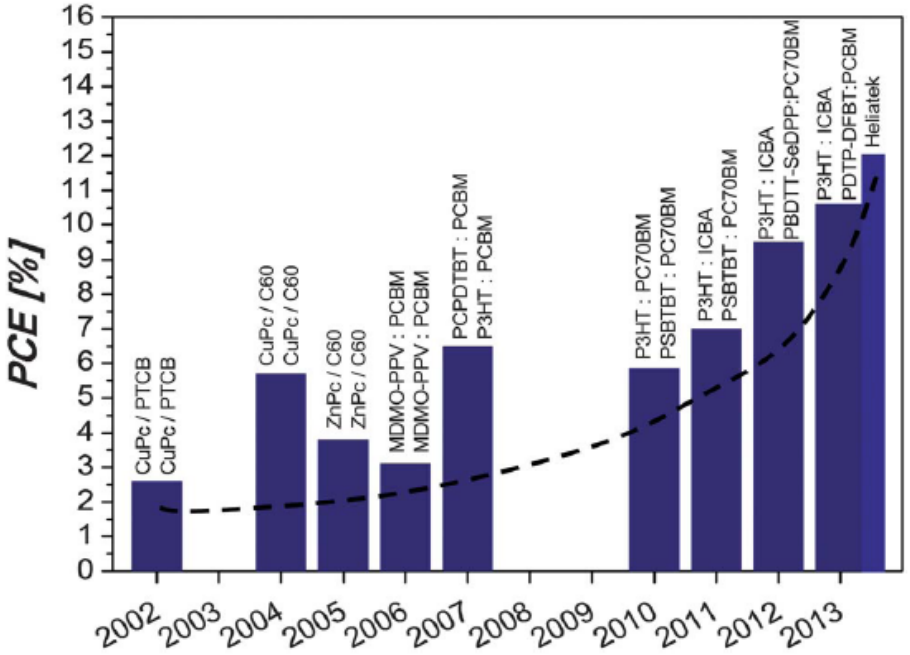

Figure 2-7. Progress in power conversion efficiency of organic tandem solar cells.

2.5.5 *Semi-Transparent Organic Solar Cells*

It is also possible to make organic solar cells into see-through or semitransparent structures. The very thin photoactive layers (< 200 nm) used in OPV devices are often intrinsically semitransparent. Therefore, OPV device can allow the incident light to pass through if the opaque counter electrodes are replaced with transparent conductive electrodes. Many transparent conductive electrodes have been applied in semitransparent OPV devices. [129-134] Developments of semitransparent OPV cells are often considered as intermediate steps towards high performance tandem device because semitransparent subcells are indispensable components of tandem devices. However, the great color and shade tunability of stand-alone semitransparent OPV devices also make them great power-generating tinted films, which are possible replacements for regular tinted windows of buildings and automobiles, curtains, and screens of consumer electronic devices.

Chapter 3. LADDER-TYPE SEMICONDUCTING POLYMERS PIDT-PHANQ AND PIDTT-DFBT FOR HIGHLY EFFICIENT POLYMER:FULLERENE SOLAR CELLS

3.1 Introduction to Low Bandgap Push-Pull Polymers for BHJ Solar Cells

Photoactive materials having bandgaps adequately small is crucial to absorb photons from high to low energy and maximize the collection of photons. Semiconducting properties such as energy levels and charge mobility of organic conjugated molecules can be adjusted drastically through chemical modifications. The versatility of molecular designs of the conjugated polymers provides almost unlimited possibilities for tailoring molecules for OPV applications.

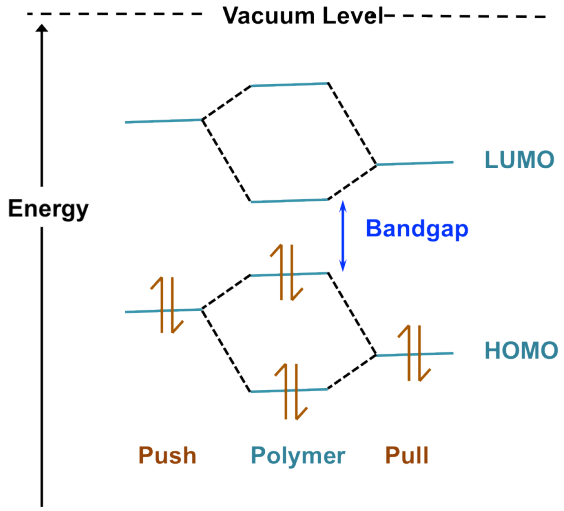

Figure 3-1. Orbital interactions between electron-rich and electron-deficient units leading to smaller bandgap push-pull conjugated polymer.

The absorption of the traditional semiconducting homopolymers (e.g. polyfluorene, PPV, P3HT) often matches poorly with the solar irradiance spectrum due to their relatively high bandgaps, resulting in significant collection loss of the long wavelength photons. To reduce the bandgap of conjugated polymers, the most common design has been utilizing push-pull effects between alternating electron rich and electron deficient.[135] As shown in **Figure 3-1**, orbital mixing between the push-pull units effectively reduces the polymer bandgap. However, the

positions of the energy levels also control the V_{oc} of the polymer:fullerene device as can be revealed by the empirical relation described below:

$$V_{oc} = \frac{1}{e}(|E^{Donor}HOMO)|-|E^{PCBM}LUMO|) - 0.3V$$

Therefore, creating low bandgap polymer and simultaneously maintaining high V_{oc} is a primary target for designing the polymer for OPV devices. The development of push-pull polymers has made significant progress in the past decade. Various push-pull combinations have been extensively studied for high efficiency OPV devices. In this chapter, two low bandgap push-pull conjugated polymers developed in our group and used in the works of this dissertation are introduced.

3.2 QUINOXALINE BASED SEMICONDUCTING POLYMER PIDT-PHANQ

3.2.1 *Conjugated Polymers Incorporating Indacenodithiophene (IDT)*

Multifused-ring conjugated polymers are favorable materials for BHJ devices due to their superior optical and electrical properties.[136-150] The fused aromatic/heteroaromatic units enhance effective conjugation of the polymer backbone to facilitate electron delocalization. Moreover, the covalently rigidified adjacent units could minimize rotational disorder and enhance charge carrier mobilities.[151-153] To date, numerous fused-ring, ladder type donor systems have been developed for OPV applications.[138,140,149,154,155]

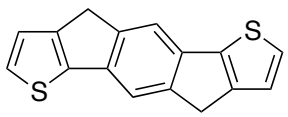

Figure 3-2. Structure of an indacenodithiophene (IDT) molecule.

Indacenodithiophene (IDT) molecule (**Figure 3-2**) is an electron-rich unit containing one central benzene and two peripheral thiophene rings rigidified by two bridging carbon atoms. The bridging carbon atoms can be functionalized with grafting side groups such as long aliphatic hydrocarbon chains, which is critical to improve the solubility of polymers containing the stiff pentacyclic IDT units and tune the intermolecular interactions. The thiophene rings of the IDT unit minimize steric hindrance with other comonomers upon polymerization and facilitate a planar backbone orientation. High charge mobilities have been reported from polymers with IDT segments.[137,156] The relatively deep HOMO level of IDT is also beneficial for attaining higher V_{oc} for OPV devices. The aforementioned features indicate IDT is an attractive electron-rich unit for push-pull conjugated polymers.

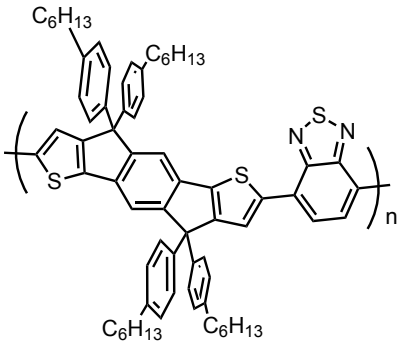

Figure 3-3. Structure of IDT-based semiconducting polymer PIDT-BT.

PIDT-BT (**Figure 3-3**) is one of the earliest demonstrated IDT based polymers, which has reached high PCE of 6.4% after careful solvent annealing.[157] The good performance has encouraged further molecular modifications of IDT-based polymers for better charge transport or light absorption.[137,145,154,158,159] Our group is also engaged in the derivatization of IDT-based polymers to take advantage of the desirable properties from these ladder-type polymers.[76,160-166]

By copolymerizing IDT with different electron withdrawing comonomers, we could fine-tune the optoelectronic properties and energy levels of the targeted polymers to achieve high efficiency.

3.2.2 *Introduction to PIDT-phanQ*

Quinoxaline and its derivatives can be implemented as the electron-deficient comonomer in designing push-pull low-bandgap semiconducting polymers. 2,3-diphenylquinoxaline (diphQ) is one commonly investigated analogue because of its facile synthesis and versatility.[167-171] The separated phenyl rings situated on position 2 and 3 of the quinoxaline, however, could induce steric hindrance and interfere intermolecular stacking. Such rotational disorder can be prevented by connecting the two phenyl substituents with a single bond between their *ortho* positions to make the fused quinoxaline derivative phenanthro[9,10-b]quinoxaline (phanQ). Conjugated polymer poly(indacenodithiophene-co-phenanthro[9,10-b]quinoxaline) (PIDT-phanQ) (**Figure 3-4**)[155] incorporates alternating IDT and phanQ comonomers with 4-hexylphenyl side chains grafting on IDT to solubilize the stiff polymer backbone. The more planar phanQ unit promotes chain packing and extends π-conjugation of PIDT-phanQ compared with its diphQ analogue.[ref]

Figure 3-5 shows the UV-Vis spectrum of PID-phanQ. Two strong absorption bands with peaks at around 645 and 440 nm can be observed, which is in good complement to the absorption of $PC_{71}BM$. An optical band gap of 1.67 eV can be estimated from its absorption onsets (~744 nm) of the as-spun films of PIDT-phanQ. The HOMO level of PIDT-phanQ estimated by cyclic voltammetry (CV) was found to be -5.28 eV, and the LUMO level of -3.61 eV can be calculated from its optical bandgap.

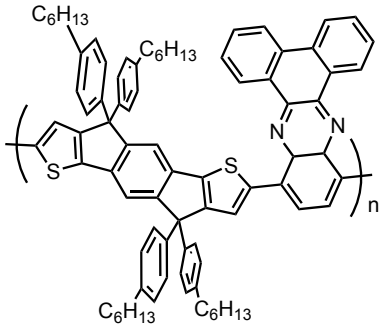

PIDT-phanQ

Figure 3-4. Structures of the conjugated polymer PIDT-phanQ.

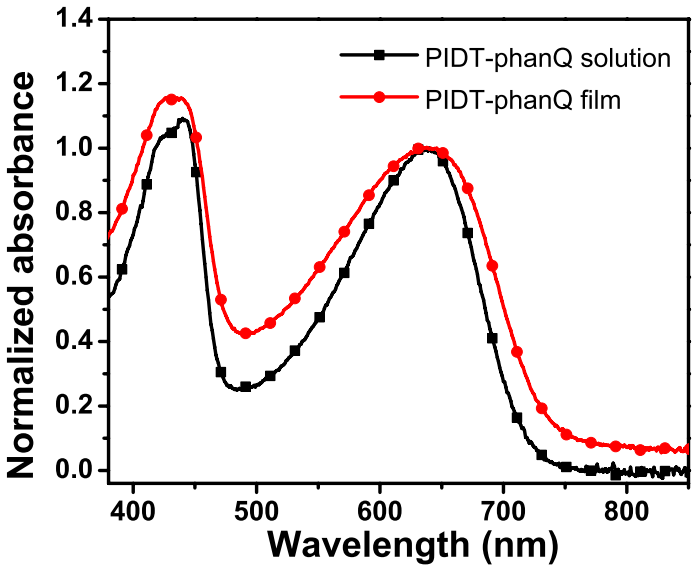

Figure 3-5. UV-Vis spectra of PIDT-phanQ in solution and film state.

3.2.3 *Measurement of Charge Transport Property by Field Effect Transistor*

Charge carrier mobility of the organic semiconductors is one of the crucial factors dictating the degree of charge recombination of OPV devices. One way to gauge the mobility of the

organic semiconductors is by building field-effect transistors (FET). The key parameters used to defined the electronic properties OFETs are charge carrier mobility (μ), threshold voltage (V_t) and current on/off ratio ($I_{on/off}$).[172] The field effect mobility in the saturation regime can be calculated using the equation shown below:

$$I_{sd} = \frac{WC_i}{2L}\mu(V_g - V_t)^2$$

I_{ds} is the source-drain current, W and L are the length and width of the channel, C_i is the capacitance density of the dielectric layer, μ is the charge carrier mobility, V_g is the gate voltage, and V_t is the threshold voltage. The capacitance density is calculated using the capacitance and thickness of the dielectric material as shown below:

$$C_i = \frac{C_0}{d} = \varepsilon(\frac{\varepsilon_0}{d})$$

The charge mobility of pristine PIDT-phanQ film was measured by building FET device in a bottom-gate top-contact configuration on n-doped silicon wafers. The transfer and output characteristics of the FET devices of PIDT-phanQ can be found in **Figure 3-6**. The FET characteristics of the PIDT-phanQ are summarized in **Table 3-1**. It was found that the hole mobility of pristine PIDT-phanQ films is rather insensitive to short-term heat treatment. The hole mobility only increases from 2.4×10^{-2} cm^2 V^{-1} s^{-1} to 2.9×10^{-2} cm^2 V^{-1} s^{-1} after the film is annealed at 110 °C for 10 min under nitrogen. The relatively high mobility of PIDT-phanQ is encouraging for its use as efficient donors in polymer solar cells.

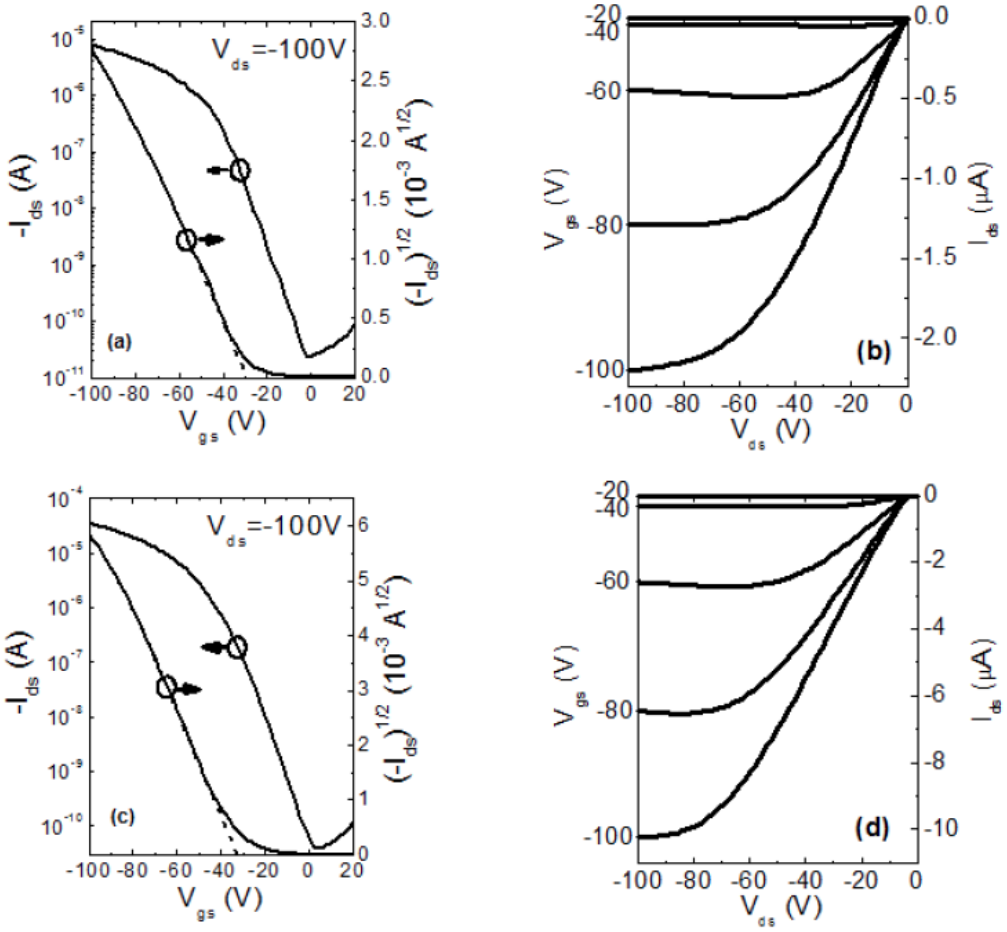

Figure 3-6. Transfer and output characteristics of PIDT-phanQ (a, b for un-annealing FET, c, d for annealing FET).

Table 3-1. FET characteristics of PIDT-phanQ with and without annealing.

Polymer	$\mu_{sat,h}$ [$cm^2\ V^{-1}\ s^{-1}$]	I_{on}/I_{off} (hole)
PIDT-phanQ	2.4×10^{-2}	10^6
PIDT-phanQ (ann.)	2.9×10^{-2}	10^6

3.2.4 *Photovoltaic Characteristics of the Polymer:Fullerene Solar Cells*

PIDT-phanQ has been mixed with several fullerene derivatives to make solar cells in the structure of ITO/PEDOT:PSS (50 nm)/polymer:$PC_{71}BM$ (1:3 w/w, 80nm)/Ca (10 nm)/Al (100

nm). **Figure 3-7** and **Table 3-2** show the *J-V* curves and output parameters of the solar cells, respectively. The best performance is obtained from the PIDT-phanQ:$PC_{71}BM$ device, which shows V_{oc} = 0.86 V, J_{sc} = 10.8 mA cm^{-2}, *FF*= 0.64, and PCE of 6.0%. Replacing $PC_{71}BM$ to its C_{60} analogue $PC_{61}BM$ causes significant drop on photocurrent due to the poor absorption of $PC_{61}BM$ while maintaining almost identical V_{oc} and *FF*, leading to overall PCE of 4.0%.

Besides PCBM, solar cells are also made from mixtures of the indene-fullerene bis-adduct ICBA ($IC_{60}BA$ and $IC_{70}BA$) with PIDT-phanQ. Previous reports of poly(3-hexylthiophene) (P3HT)[21,22] with ICBA have shown significant enhancements in V_{oc} values compared to PCBM blends, with J_{sc} being maintained in the ICBA-based device. The V_{oc} enhancement is attributed to destabilization of the charge transfer (CT) state when using fullerene derivative ICBA that are more difficult to reduce.[173,174] **Figure 3-7** and **Table 3-2** show that switching to ICBA also increases V_{oc} for our PIDT-PhanQ blends. The value of V_{oc} = 1.0 V for the ICBA blends is 140 mV larger than that for the PCBM-based devices (V_{oc} = 0.86 V). However, our devices exhibit a marked trade-off between J_{sc} and V_{oc}. This trade-off is in contrast to what has been observed for P3HT:ICBA devices compared to P3HT:PCBM but is consistent with reports from some other high performance polymer:PCBM blends like the carbazole-based push−pull polymer PCDTBT.[175] All the PIDT-phanQ:fullerene blends show similar surface roughness and degree of phase-separation as displayed in **Figure 3-8**; therefore, morphological difference is unlikely the cause for the variation of device performance.

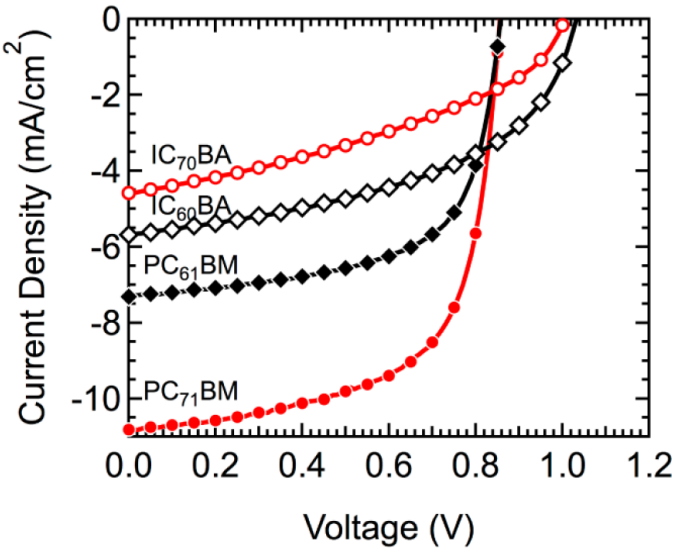

Figure 3-7. Photocurrent density as a function of voltage for the PIDT-phanQ:PCBM and PIDT-phanQ:ICBA devices.

Table 3-2. Performance metrics for PIDT-phanQ:fullerene devices under illumination.

Device	V_{oc} (V)	J_{sc} (mA cm^{-2})	*FF*	PCE (%)
PC$_{71}$BM	0.86	10.8	0.64	6.0
PC$_{61}$BM	0.86	7.30	0.63	4.0
IC$_{60}$BA	1.0	5.69	0.49	2.9
IC$_{70}$BA	1.0	4.60	0.39	1.8

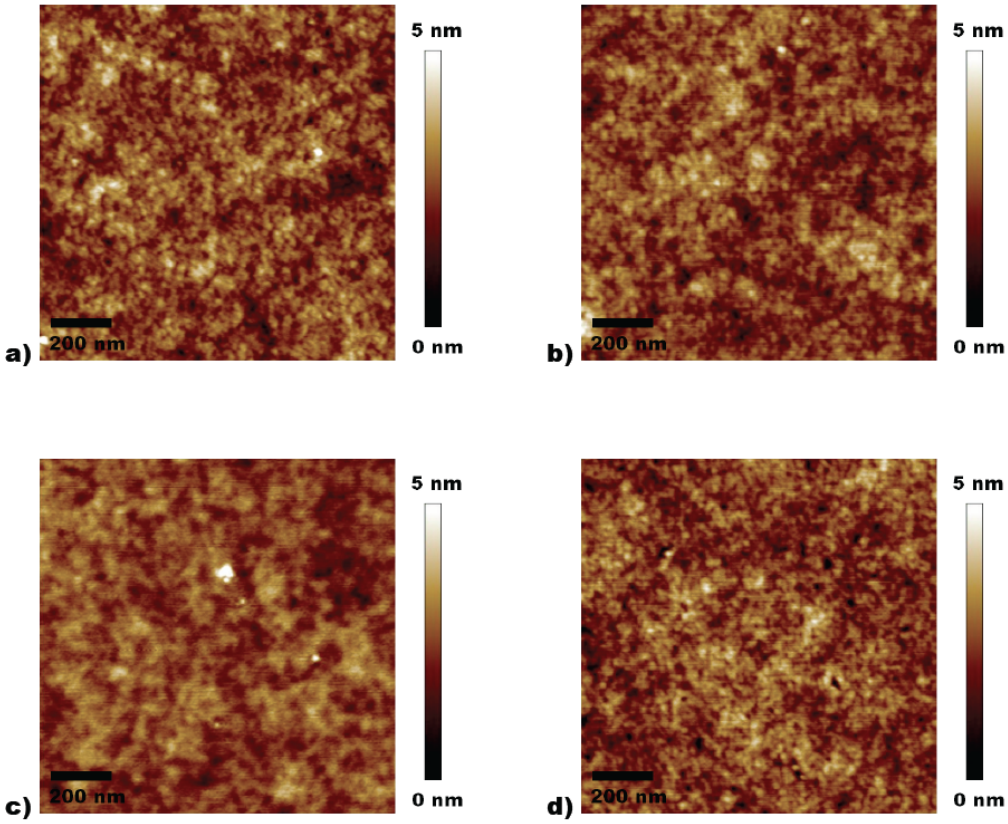

Figure 3-8. AFM images showing the surface topography for PIDT-PhanQ blended with a) $PC_{71}BM$, RMS surface roughness ca. 0.62 nm; b) $PC_{61}BM$, RMS surface roughness ca. 0.58 nm; c) $IC_{70}BA$, RMS surface roughness ca. 0.61 nm; and d) $IC_{60}BA$, RMS surface roughness ca. 0.59 nm.

Since the smaller PCE for both ICBA derivatives is due in part to substantial losses in J_{sc}, the examination of examined both the external (EQE) and internal (IQE) quantum efficiencies for these devices can provide some insights. **Figure 3-9** plots EQE and IQE values for these blends as a function of wavelength. The upper panel of **Figure 3-9** shows that the trend in EQE coincides with the trend in J_{sc} ($PC_{71}BM > PC_{61}BM > IC_{60}BA > IC_{70}BA$). The IQE values plotted in the lower panel of **Figure 3-9** were determined using the transfer matrix approach to calculate the active layer absorption[176] from optical constants obtained by variable angle spectroscopic ellipsometry. Significantly, the IQE values for the PCBM derivatives are quite high, with the

IQE for $PC_{71}BM$ exceeding 90% over much of the visible region. These high IQE values underpin the strong device performance of the PIDT-phanQ:$PC_{71}BM$ system, and place these blends among the highest performing materials reported.[40,44,177] The IQE values for the ICBA-based devices are lower than for the PCBM devices, which explains their lower J_{sc}.

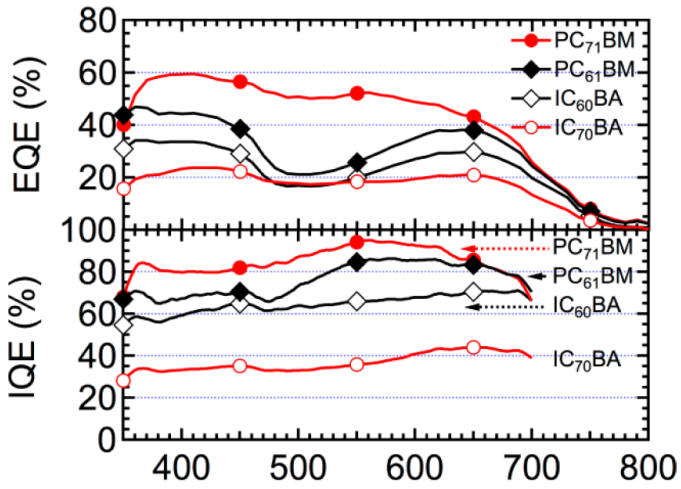

Figure 3-9. External (upper panel) and internal (lower panel) quantum efficiency for the PIDT-phanQ:fullerene devices.

3.2.5 *Recombination of PIDT-phanQ:ICBA BHJ Blend*

Charge recombination via the donor triplet[178] has been considered as a process that can limit attainable J_{sc} whenever the energy of the interfacial CT state is raised above that of the donor triplet state.[178-184] In the cases of our PIDT-phanQ:fullerene blends, it is found that although the triplet energy level of PIDT-phanQ is well below the CT state, the BHJ device of PIDT-phanQ:$PC_{71}BM$ can still work efficiently and deliver high IQE (>90% over most visible region), but IQE of the PIDT-phanQ:ICBA blends are significantly reduced. The changes of IQEs observed upon fullerene derivatization are noteworthy given the driving forces for recombination to form triplet excitons in these blends. To find out the reasons of the reduced performance of

PIDT-phanQ with the higher adduct fullerene ICBA, spectroscopic analyses are carried out by Dr. Schlenker *et al.* to correlate the resulting device performance with potential recombination pathways.[185]

Figure 3-10 shows the proposed energy level diagram and recombination scheme of the PIDT-phanQ:ICBA system based on spectroscopic evidences.[185] Quenching of the S_1 states of the polymer (1.61 eV) or the $IC_{60}BA$ (1.69 eV) leads to either free charges or population of the lowest energy charge transfer state (CT_1 = 1.44 eV), which is nearly degenerate with the $IC_{60}BA$ T_1 state at 1.48 eV. The fullerene triplet state may serve as an important intermediate in the recombination process in PIDT-PhanQ:$IC_{60}BA$ blends and may decay either by Dexter energy transfer to the polymer T_1 state (1.01 eV), or by direct decay (both radiative and nonradiative) to the fullerene ground state. Such new relaxation pathway through other higher-lying triplet states may be kinetically more accessible and responsible for the reduced J_{sc} of the PIDT-phanQ:ICBA devices.

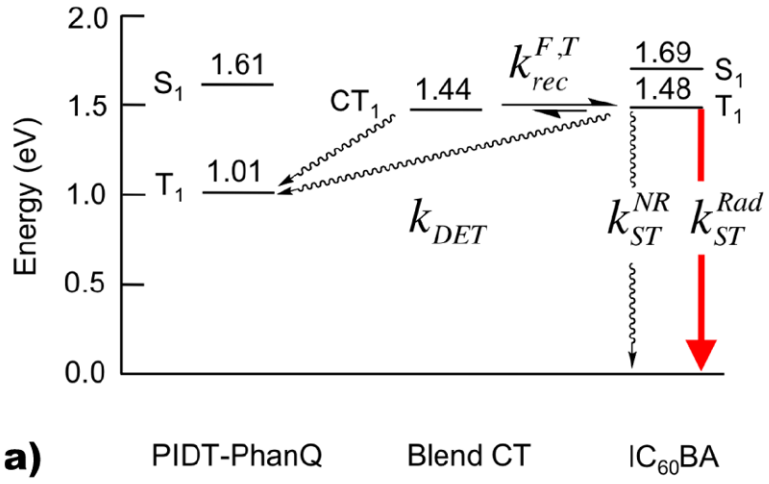

Figure 3-10. State energies and proposed recombination pathways for PIDT-PhanQ:$IC_{60}BA$.

The photovoltaic performance of the PIDT-phanQ:fullerene devices and their photophysical investigations suggest several interesting conclusions. First, in certain systems low-lying triplet states need not limit efficient photocurrent collection in organic solar cells (e.g., PIDT-PhanQ:PCBM), since the process of charge separation may kinetically outcompete other loss processes. Additionally, anomalously high triplet populations may not always form most rapidly via the lowest energy triplet state, but rather through other higher-lying triplet states that may be more kinetically accessible (e.g., PIDT-PhanQ:ICBA). These results suggest important considerations for the optimization of organic solar cells. First, as noted before, the fullerene triplet can serve as an important recombination intermediate, especially in blends where a substantial portion of the light is absorbed by the fullerene.[186-188] Second, and more importantly, photocurrent losses via triplet states may be avoided kinetically as a result of either slow triplet formation or fast carrier escape from the interface.

3.3 Fluorinated Ladder-Type Polymer PIDTT-DFBT

3.3.1 *Introduction*

Benzothiadiazole (BT) is one of the most extensively employed electron deficient moieties in the push-pull alternating semiconducting polymers for OPV applications. Many electron rich moieties have been copolymerized with BT and shown outstanding device performance.[40,41,157,189,190] For example, PCPDTBT[41] and its silicon substituted analogue PSBTBT[43,189,191,192] show excellent light harvesting capability due to its small bandgap as low as 1.45 eV, which have led to impressive short-circuit current density (J_{sc}) of > 15 mA/cm^2 and PCE of > 5%. However, their relatively high-lying HOMO levels result in relatively low V_{oc} of only ~ 0.6 V. Another class of poly[(9,9-dialkylfluorene)-2,7-diyl-*alt*-(4,7-bis(2-thienyl)-2,1,3-benzothiadiazole)-5,5′-diyl] (PFDTBT)-based polymers is noted for their deep HOMO levels

which give high V_{oc} of ~1.0 V with corresponding PCE of 2~4%.[193,194] When the fluorene units in PFDTBT are replaced with either a carbazole[40] or a silafluorene[190] derivative, a significant enhancement of PCE was achieved due to improved charge transport properties. However, these polymers suffer inferior light harvesting due to their relatively large bandgap (~1.9 eV), which is approximately the same as P3HT. These examples manifest how important the positions of the energy levels can affect the performance of OPV devices.

PIDT-BT is another great BT-based conjugated polymer that has shown good performance (PCE > 6%, V_{oc} = 0.86 V) resulting from its high charge mobility and relatively low bandgap (E_g ~ 1.75 eV). Through chemical modification, it is possible to further optimize the energy levels of its frontier orbital and improve the performance of OPV device. Fluorine substitution onto the polymer backbone has been an effective way of increasing the V_{oc} of the OPV devices. Several preceding examples[164,195-197] have demonstrated that the strongly electronegative fluorine atoms decorated on the polymer backbone can lower the HOMO and LUMO energy levels of the push-pull conjugated polymers without significant effects on their optical properties. By introducing of fluorine atoms onto the BT unit, the HOMO level of the resulting polymer poly(indacenodithiophene-difluorobenzothiadiazole) PIDT-DFBT (**Figure 3-11**) was successfully stabilized compared with PIDT-BT. However, while the V_{oc} of the BHJ device based on PIDT-DFBT can be enhanced, the J_{sc} and FF were simultaneously decreased due to the inferior charge transport mobility of PIDT-DFBT, which counterbalanced the V_{oc} enhancement and consequently resulted in slightly inferior PCE.[164] In order to compensate the charge transport limitation, the electron-donating fused-ring segment of the polymer is extended. The approach of ring extension has been considered promising for improving the charge transport properties and light-conversion efficiency of polymers.[139,148] In our design, the IDT unit was

extended by replacing the two thiophene rings with thieno[3,2-b]thiophene (TT) units. TT has been widely utilized to improve charge mobility of polymers[136,198-200] by extending the effective conjugation length and improving backbone planarity. **Figure 3-11** shows the structure of the resulted polymer poly{indacenodithieno[3,2-b]thiophene-difluorobenzothiadiazole} (PIDTT-DFBT). With the two-stage derivatization of PIDT-BT by fluorine substitution and extending IDT to seven-ring IDTT building block, the semiconducting polymer PIDTT-DFBT simultaneously demonstrates deeper HOMO level and improved charge transport properties, leading to improved V_{oc} (0.95 V) and PCE of (7.03%) without sacrificing J_{sc} and FF.[201] In the following sections, the fundamental properties PIDTT-DFBT are introduced.

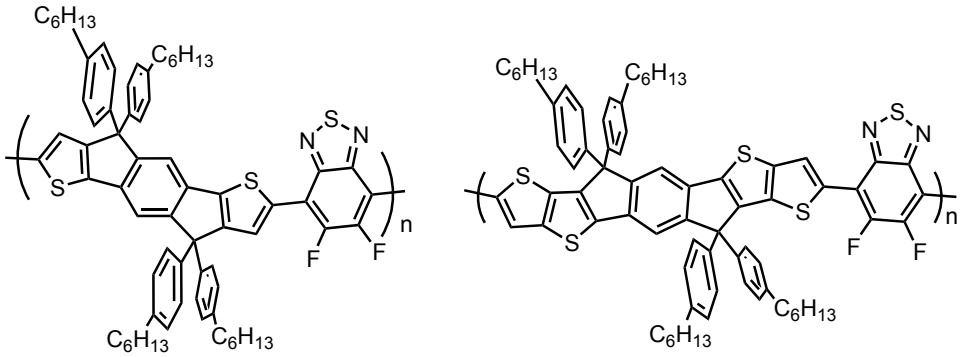

Figure 3-11. Structures of the conjugated polymers PIDT-DFBT (left) and PIDTT-DFBT (right).

3.3.2 *Fundamental Properties and PV Characteristics of PIDTT-DFBT*

The UV-Vis absorption spectra of PIDTT-DFBT in *o*-DCB solution and in thin film are shown in **Figure 3-15a** and **3-15b**, respectively. The thin film absorption maxima (λ_{max}) of PIDTT-DFBT is around 650 nm and the optical bandgaps extracted from the absorption band edges is estimated to be around 1.78 eV. The intense absorption peaks of the two polymers indicate the existence of strong intramolecular charge transfer (ICT) between the IDTT and

DFBT units. The HOMO and LUMO energy levels of PIDTT-DFBT acquired by cyclic voltammetry are exhibited in **Table 3-3**.

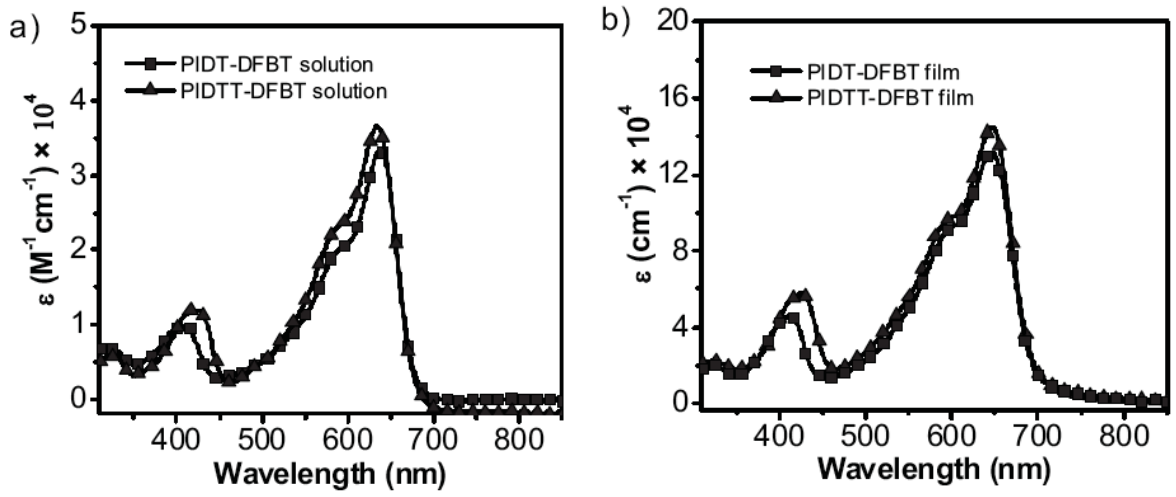

Figure 3-12. UV-Vis spectra of PIDT-DFBT and PIDTT-DFBT in (a) solution and (b) film states.

Table 3-3. Electrochemical and optical properties of PIDT-DFBT and PIDTT-DFBT.

	HOMO (eV)	LUMO (eV)	Electrochemical Bandgap (eV)	Optical bandgap[a] (eV)
PIDTT-DFBT	-5.30	-3.50	1.80	1.78

[*a*] The optical bandgap is derived from the absorption edge from the UV-Vis spectrum of the polymer films.

Figure 3-13 and **Table 3-4** shows the *J-V* characteristics and the output parameters of the PIDTT-DFBT:$PC_{71}BM$ BHJ device in the device structure of ITO/PEDOT:PSS/ polymer:$PC_{71}BM$ (1:3)/Bis-C_{60} salt/Ag. Bis-C_{60} salt is a dual-function fullerene surfactant, which simultaneously modifies the work-function of the metal electrode and transports electron.[76,116] The performance of PIDTT-DFBT:$PC_{71}BM$ is significantly enhanced compared with the devices made of PIDT-DFBT,[201] which is ascribed to the improved charge transport properties of PIDTT-DFBT as revealed in **Table 3-5**.

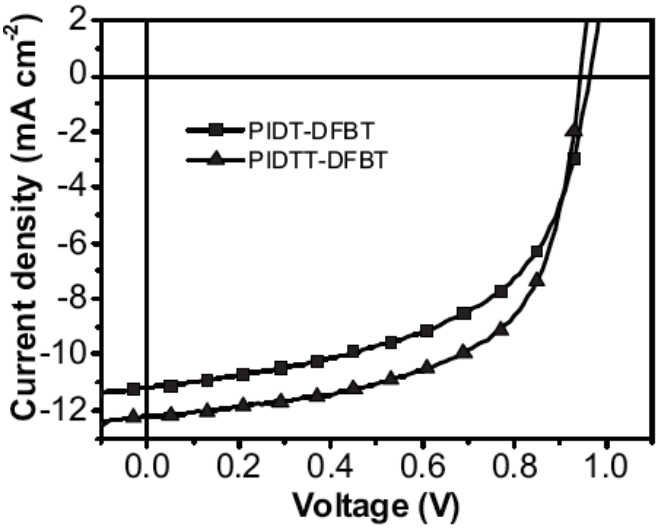

Figure 3-13. (a) Characteristic *J–V* curves for the BHJ solar cells derived from PIDT-DFBT and PIDTT-DFBT.

Table 3-4. Photovoltaic characteristics of PIDT-DFBT and PIDTT-DFBT.

Device	V_{oc} [V]	J_{sc} [mA cm^{-2}]	FF	PCE [%]
PIDT-DFBT:$PC_{71}BM$	0.97	11.20	0.55	5.97
PIDTT-DFBT:$PC_{71}BM$	0.95	12.21	0.61	7.03

Table 3-5. FET characteristics of PIDT-DFBT and PIDTT-DFBT.

Polymer	$\mu_{sat,h}$ [cm^2 V^{-1} s^{-1}]	I_{on}/I_{off} (hole)
PIDT-DFBT	$\approx 2\times10^{-3}$	2×10^{3}
PIDTT-DFBT	$\approx 2\times10^{-2}$	5×10^{4}

3.3.3 *Summary*

PIDTT-DFBT created by two-stage modifications of PIDT-BT to PIDTT-DFBT demonstrates better charge mobility and deeper HOMO level. The solar cell made from PIDTT-DFBT showed an improved PCE of 7.03% with a large V_{oc} of 0.95 V. This proves the effectiveness of using a multi-fused-ring donor to enhance the device performance.

3.4 EXPERIMENTAL SECTION

3.4.1 *Materials and Instruments*

$PC_{71}BM$ of purity better than 98 % was purchased from American Dye Source. Poly(3,4-ethylenedioxy-thiophene):poly(styrene sulfonate) (PEDOT:PSS, Baytron P VP AI 4083) was purchased from H. C. Stark. Chemicals were used as received.

Synthetic procedures of the donor polymers PIDT-phanQ and PIDTT-DFBT have been described elsewhere.[155,164,201] The molecular weights of the polymers were measured using GPC with THF as an eluent. The number-average molecular weights (Mn) of the polydispersity indices (PDI) of the polymers are shown in **Table 3-6**. The surface morphology of the active layers was characterized under tapping mode using the Veeco multimode AFM with a Nanoscope III controller.

Table 3-6. Number-average molecular weights (Mn) and polydispersity indices (PDI) of the conjugated polymers.

	PIDT-phanQ	PIDTT-DFBT
Mn (KDa)	82.4	24.0
PDI	2.84	2.58

3.4.2 *Mobility Measurements by Field Effect Transistors*

Heavily doped silicon substrates with a 300 nm thick thermally grown SiO_2 dielectric (Montco Silicon Technologies, Inc.) were cleaned sequentially by sonication in acetone and isopropyl alcohol, followed by a 5 minutes exposure to air plasma. The surface of the silicon substrates was treated with hexamethyldisilazane (HMDS) by vapor phase deposition in a vacuum oven (200 mTorr, 100 °C, 3 hours). The polymer film was spin-coated from its 5 mg/ml chloroform solution at 2,000 rpm under a dry nitrogen environment. No thermal treatment was

performed on the polymer. Source and drain electrodes (L=1000 μm, W=12, 20 or 30 μm) were defined by thermally evaporating 50 nm thick gold through a shadow mask. The transfer and output characteristics of the thin film transistors were obtained on an Agilent 4155B semiconductor parameter analyzer under nitrogen atmosphere. The field-effect mobility was calculated in the saturation regime from the linear fit of $(I_{ds})^{1/2}$ versus V_{gs}. The threshold voltage (V_t) was estimated as the *x* intercept of the linear section of the plot of $(I_{ds})^{1/2}$ versus V_{gs}.

3.4.3 *OPV Device Fabrication and Characterization*

Indium tin oxide coated glass substrates (ITO, 15 Ω per square) were cleaned sequentially by sonicating in detergent, de-ionized water, acetone, and isopropyl alcohol, followed by blow-drying under nitrogen stream and exposing under oxygen plasma for 5 minutes. In the conventional architecture solar cells, a thin layer (ca. 40 nm) of PEDOT:PSS (filtered at 0.45 μm, Nylon) was first spin-coated onto the ITO surface and baked at 140°C for 10 min in ambient. Subsequently, the substrates were transferred into a nitrogen-filled glovebox for further processing.

Solution of the polymer:fullerene blends in *o*-DCB was stirred at 85 ºC overnight before use. The solution was filtered (0.2 μm PTFE) before spin-coating. The substrates were annealed at 110 °C for 10 minutes after spin-coating the BHJ blends. The DFBT-Based polymer:$PC_{71}BM$ solar cells were annealed at 110 °C for 5 minutes after the Bis-C_{60} salt was spin-coated onto the BHJ layer. Metal electrodes were thermally evaporated through the openings of the shadow masks with the size of 10.08 mm^2 under high vacuum (< 2×10^{-6} Torr) to define the active area of the solar cells.

The *J-V* characteristics were measured using a Keithley 2400 source-measurement unit. A xenon lamp coupled with an AM1.5G filter was used as the solar simulator. The light intensity

was set to 1 sun (100 mW/cm^2) using a calibrated Hamamatsu silicon diode with a KG5 color filter, which can be traced to the National Renewable Energy Laboratory (NREL). The EQE system uses a lock-in amplifier (Stanford Research Systems SR830) to record the short-circuit current under chopped monochromatic light.

Chapter 4. HALOGEN-FREE SOLVENT PROCESSING FOR SUSTAINABLE DEVELOPMENT OF HIGH EFFICIENCY ORGANIC SOLAR CELLS

4.1 INTRODUCTION

The morphology of the photoactive layer plays a key role in governing charge generation and charge transport in BHJ solar cells.[202-204] An ideal BHJ layer would consist of interpenetrating nanometer-scale domains of conjugated polymer and fullerene. Such a structure ensures high density of donor/accepter interface for excitons to dissociate through photoinduced charge transfer. Domains made of the same material have to retain interconnected as continuous percolating pathways for unipolar charge transport. Cost-effective manufacturing of OPV devices depends on the use of simple coating methods to create the BHJ layer such exquisite structure. Therefore, the morphological optimization via tuning coating parameters has been one of the top challenges for OPV.

Halogenated solvents have been widely used as the processing solvents for the polymer-fullerene solar cells. One of the reasons for their popularity is that the solubility of many fullerene-based molecules in halogenated aromatic solvents is much higher than in halogen-free solvents (e.g. solubility of C_{60} is 7.0 mg/mL in chlorobenzene, 27 mg/mL in *o*-DCB, 2.8 mg/mL in toluene, and 5.2 mg/mL in xylene).[205] In fact, the difficulties in obtaining blend morphologies optimal for good operation of OPV device have lead to very few reports of high-efficiency devices prepared without halogenated solvents.[206-208] As a result, chlorobenzene and *o*-DCB have become the most pervasively used solvents for casting the active materials in the polymer-fullerene solar cells. However, halogen-free solvent processing is attractive for large-scale module manufacturing[209] from a life cycle assessment and sustainable development point of view.[210] Therefore, solvent systems anticipated to be more transferable to sustainable module production, while maintaining high efficiency, are extremely compelling. Water is the most

favorable processing solvent from cost and sustainability standpoints. However, efficient photoactive materials compatible with water are currently scarce. [209,211]

Halogen-free organic solvents such as toluene and isomers of xylene are comparatively preferable organic solvents, since their aggregate environmental accumulation can be mitigated with comparative ease,[212] making them more compatible with environmental impact concerns associated with large-scale manufacturing. However, the tendency of toluene and xylenes to promote less-than-ideal morphologies in the BHJ layer[31,213] typically counteracts their attraction as halogen-free replacements as processing matrices.

In this chapter, we demonstrate the fabrication and optimization of a highly efficient BHJ solar cell (PCE > 6%) based on the conjugated polymer PIDT-phanQ and $PC_{71}BM$ from simple processing steps using completely halogen-free solvents to obtain performance equivalent to that obtained with the regular halogenated solvent systems. To achieve this level of performance, we explored the effects of using solvent additives and found that the active layer morphology and device performance could be dramatically improved if the solvent combination was carefully chosen.

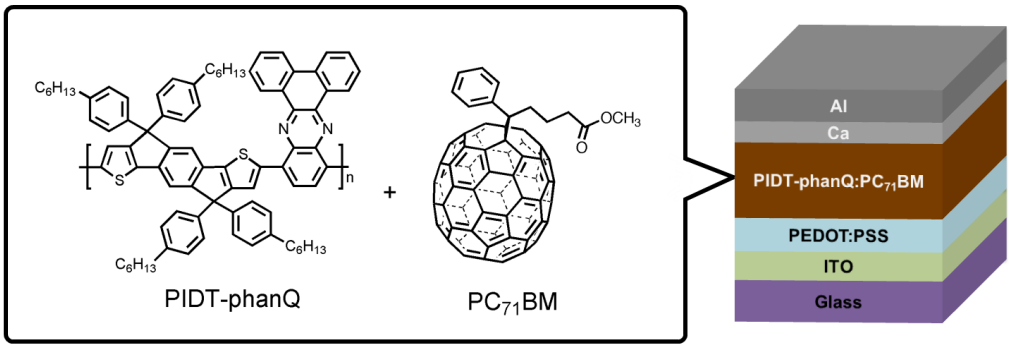

Figure 4-1. Device architecture and the chemical structures of the active materials PIDT-phanQ and $PC_{71}BM$.

4.2 DEVICES PROCESSED FROM PURE HALOGEN-FREE SOLVENTS

Unlike many semi-crystalline conjugated polymer systems that rely on post-casting treatments to enhance the crystallization of the polymer phase for better charge transport,[57,214-216] PIDT-phanQ is relatively amorphous, yet still possesses high charge carrier mobility and good solubility, making this class of polymers promising for high performance OPVs that can be fabricated by simple processes[165] without time-consuming processing steps lower manufacturing speed. Two halogen-free solvents, toluene and *o*-xylene, are investigated as the processing solvent the for PIDT-phanQ:$PC_{71}BM$ BHJ devices. PIDT-phanQ:$PC_{71}BM$ blend in 1:3 weight ratio were dissolved in either toluene (20 mg ml^{-1}) or *o*-xylene (30 mg ml^{-1}). **Figure 4-1** and **Figure 4-2** show the device architecture and *J-V* characteristics of the PIDT-phanQ:$PC_{71}BM$ BHJ devices, respectively, and **Table 4-1** summarizes the photovoltaic output parameters of the devices. PIDT-phanQ:$PC_{71}BM$ BHJ solar cells cast from toluene or *o*-xylene both showed much inferior performance compared to PCE > 6% for devices cast from *o*-DCB (**Figure 3-7**). An extremely poor PCE (< 0.05%) was obtained from the toluene-processed device. The devices processed from *o*-xylene performed better than the toluene-processed device but still only delivered PCE of 3.3%, which is roughly half of the PCE of the device made from *o*-DCB.

Table 4-1. Summary of PIDT-phanQ:$PC_{71}BM$ device performance from different casting solvent systems.

Host solvent	Me-naph concentration (vol%)	V_{oc} [V]	J_{sc} [mA cm^{-2}]	*FF*	PCE [%]	R_s [Ω cm^2]	R_{sh} [Ω cm^2]	$J_{sc,\ calc.}$ [mA cm^{-2}]
Toluene	0	0.88	0.1	0.39	0.03	1818.2	8282.8	
Toluene	1	0.87	10.3	0.65	5.8	7.3	970.3	
Toluene	2	0.87	10.8	0.65	6.1	7.7	1059.5	10.6
Toluene	4	0.87	10.2	0.65	5.8	6.8	853.1	
o-Xylene	0	0.89	6.8	0.54	3.3	12.7	589.7	
o-Xylene	1	0.86	10.6	0.62	5.7	9.4	768.2	
o-Xylene	2	0.86	10.5	0.63	5.7	8.3	695.9	10.0
o-Xylene	4	0.87	10.2	0.62	5.5	9.5	847.4	

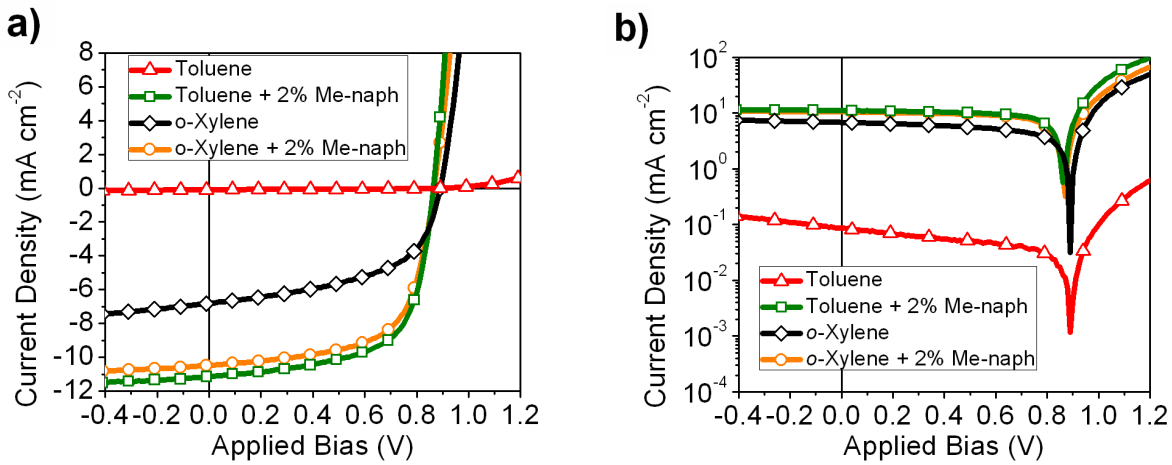

Figure 4-2. *J-V* curves of PIDT-phanQ:$PC_{71}BM$ devices under simulated AM 1.5 global illumination processed from pure toluene (triangles), toluene + 2% Me-naph (squares), pure *o*-xylene (diamonds), and *o*-xylene + 2% Me-naph (circles). a) Linear and b) semi-logarithmic plots.

Figure 4-2 shows that both halogen-free solvents still yield devices with diode behavior and maintain the V_{oc} close to 0.9 V, similar to the previous *o*-DCB-cast devices. Decreases in both photocurrent and fill-factor were responsible for the lower efficiencies. Simple estimations of the

series resistance (R_s) and shunt resistance (R_{sh}) from the slopes[217] of the experimentally obtained *J-V* curves are also given in **Table 4-1**. The toluene-processed device displays exceptionally high R_s of 1818.2 Ω cm^2, suggesting extremely poor charge transport through the polymer:fullerene composite.

4.2.1 *Morphology Analyses*

To clarify the drop in device performance we perform topological characterization using atomic force microscopy (AFM). The topography images of the films processed from toluene and *o*-xylene are shown in **Figure 4-3a** and **Figure 4-3c**, respectively. While AFM topography probes only the surface features of the film, the gross morphological differences observed between solvents is dramatic. Active layers cast from pure halogen-free solvents showed large-scale phase separation and rough surfaces. The degree of phase separation has strong correlation to the choice of solvent. Toluene processed device show large granular clusters (domain size roughly 1.1 μm) sporadically distributed over the film with root-mean-square (RMS) roughness as high as 116 nm. Films cast from *o*-xylene exhibit smaller clusters (ca. 150 - 400 nm) with RMS roughness of 12.3 nm. In either case, the morphology of the PIDT-phanQ:$PC_{71}BM$ blend shows serious phase segregation compared to the film cast from *o*-DCB (**Figure 3-8**) and is apparently far from optimal for efficient device performance.

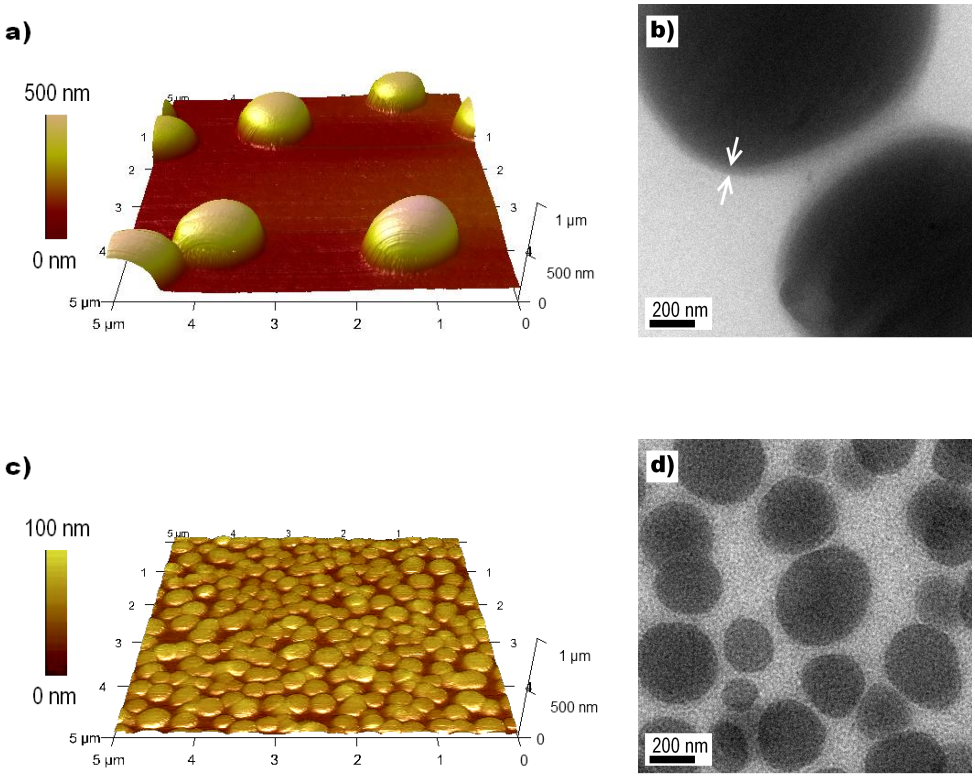

Figure 4-3. AFM topography (a, c, 5 × 5 μm) and TEM micrographs (b, d, scale bar indicating 200 nm) of PIDT-phanQ:$PC_{71}BM$ blend films (1:3, w/w) processed from pure toluene (a, b) and from pure *o*-xylene (c, d). In (b), the arrows are indicating a 40 nm region of intermediate contrast surrounding the surface of an aggregated cluster as discussed in the text.

Complementary morphology examinations of the PIDT-phanQ:$PC_{71}BM$ blends cast from toluene (**Figure 4-3b**) and *o*-xylene (**Figure 4-3d**) via transmission electron microscopy (TEM) also clearly display the granular clusters observed under AFM. Note that regions of intermediate contrast exist, indicated by the white arrows in **Figure 4-3b** that are distinct from the darkly shaded regions and the brightly shaded surrounding medium. These variations in image contrast suggest regions of different compositions. Based on previous reports, $PC_{71}BM$ clusters often appear darker than conjugated polymers in bright-field TEM images due to higher scattering density.[218] Therefore, **Figure 4-3b** suggests that the PIDT-phanQ:$PC_{71}BM$ is phase separated

into large $PC_{71}BM$-rich clusters embedded in a ca. 40 nm surface coating with higher PIDT-phanQ content.

As mentioned above, drastic performance changes linked to morphological changes are common for BHJ devices processed from halogen-free solvents. For example, when the casting solvent for BHJ blend of MDMO-PPV (**Table2-2**) and $PC_{61}BM$ was changed from chlorobenzene to toluene[31,219] or xylene,[213,220] large-scale phase separation or clusters also appeared corresponding to much poorer device performance. Shaheen *et al.*[31] observed a more than two fold difference between devices cast from chlorobenzene (PCE = 2.5%) and toluene (PCE = 0.9%), and Rispens *et al.*[220] showed ~30% reduction on PCE for xylene-cast device (PCE = 2.1%) compared to the chlorobenzene-cast device (PCE = 3.0%).

Similar to the toluene-cast PIDT-phanQ:$PC_{71}BM$ films, toluene-cast MDMO-PPV:$PC_{61}BM$ films also exhibited severe phase-separation, where fullerene-rich aggregates were embedded in an polymer-rich matrix.[219] Such severe phase segregation of large fullerene-rich grains was believed to be caused by $PC_{61}BM$'s low solubility in toluene. It was found that the higher the loading of $PC_{61}BM$ in the MDMO-PPV:$PC_{61}BM$, the more severe the phase separation. It was also observed that the degree of phase separation was inversely correlated with fullerene solubility in the casting solvent, with relative solubility values being xylene < chlorobenzene < *o*-DCB.[205,220]

In the present work, the bright field TEM image (**Figure 4-3d**) of the *o*-xylene-cast PIDT-phanQ:$PC_{71}BM$ blend exhibits dark regions (ca. 50 - 300 nm in width) with sharper edge contrast than observed for the > 1 μm feature in the toluene case. Since *o*-xylene is a better solvent for $PC_{71}BM$ than toluene, the degree of phase-separation was expected to decrease, which may explain the observation of smaller cluster sizes and the lack of the observable surrounding skins.

Note that the PIDT-phanQ:$PC_{71}BM$ system also shows the trend of decreasing phase separation with increasing fullerene solubility as that for the MDMO-PPV:$PC_{61}BM$ blends, suggesting the performance of halogen-free solvent processed devices could be improved by tuning the solubility of the fullerene in the processing fluid.

4.3 Influences of Solvent Additive 1-Methylnaphthalene on Morphology and Device Performance

Among several morphological optimization methods, manipulation of the solvent composition has been a popular strategy.[193,221] Specifically, adding a small fraction of a secondary liquid additive into the regular solvent has successfully improved the performance of many devices.[44,62,222-225] The origin of the improved device performance and the relationship between solvent additive and blend morphology are current areas of intense research. For instance, diiodoalkanes such as 1,6-diiodohexane (DIH) or 1,8-diiodooctane (DIO) are very popular solvent additives, offering selective solubility of an active component and an extended drying time due to its high boiling point.[62] Using diiodoalkanes as the additive promotes ordering of semi-crystalline conjugated polymers and $PC_{61}BM$ (or $PC_{71}BM$) and increases the degree of phase-separation, which has successfully led to significantly enhanced device efficiency in BHJ devices based on blends of PCPDTBT:$PC_{71}BM$[62] and PBTTPD:$PC_{71}BM$.[222] Conversely, 1-chloronaphthlene (Cl-naph) may help to create finer phase separation in BHJ systems. Using Cl-naph as the processing additive helps dissolve conjugated polymers with low solubility,[226] increases the detention time of active materials due to the solvent's low vapor pressure, and ultimately improves the phase-separation on the nanometer length scale. However, these popular additives all contain halogens, which runs counter to the goal of using only non-halogenated solvent.

Since the low fullerene solubility in toluene and *o*-xylene is possibly responsible for the severe phase separation of PIDT-phanQ:$PC_{71}BM$ blends, we hypothesized that adding a small fraction of a more potent solvent for $PC_{71}BM$ to the processing fluid might improve film properties and device performance. The halogen-free methyl analogue of Cl-naph, 1-methylnaphthalene (Me-naph), is known to be an exceptional fullerene solvent[227] and is often used as the solvent for chemical reactions involving fullerenes.[228,229] The boiling point of Me-naph is also high (> 240 °C) and close to that of Cl-naph. We thus examined Me-naph as a logical potential alternative to Cl-naph.

To test the effects of Me-naph as a solvent additive on PIDT-phanQ:$PC_{71}BM$ blends, we investigated concentration effect of Me-naph in toluene and *o*-xylene. Three concentrations (1%, 2%, and 4% by volume) of Me-naph in either toluene or *o*-xylene were examined. **Table 4-1** also includes the output parameters of the devices processed with Me-naph and the *J-V* characteristics of the best devices are shown in **Figure 4-2**. At all three concentrations of Me-naph, the additive processed devices significantly improved J_{sc} (greater than 10 mA cm^{-2}) and FF (greater than 0.60) while maintaining the V_{oc} at about 0.87 V. The optimized device was obtained from 2% of Me-naph in toluene with PCE = 6.1%, comparable in efficiency to our previously reported best *o*-DCB-cast devices. EQE of PIDT-PhanQ:$PC_{71}BM$ solar cells processed from toluene or *o*-xylene containing 2% Me-naph are presented in **Figure 4-4**. The EQE spectrum of the toluene + 2% Me-naph processed device shows two main responsive bands; one that peaks at 410 nm with the maximum value of 60%, and a second band that peaks around 560 nm with a value of 56% and has a shoulder around 650 nm. For the *o*-xylene + 2% Me-naph processed device, a short wavelength band peaked at 420 nm is also observed, but the EQE plateaus at roughly 43% from 500 nm to 650 nm. The EQE for the toluene + 2% Me-naph device is more than 5% higher over

the range from 490 nm to 610 nm, where the absorption coefficient of the polymer is relatively low. The calculated short-circuit current density from the integration of the EQE spectra ($J_{sc,\ calc.}$) of the test cells were and summarized in **Table 4-1**. Slightly lower $J_{sc,\ calc.}$ comparing to the J_{sc} extracted from the *J-V* curves was observed. Since the EQE was not tested under inert environment, the devices might have slightly decayed. Nevertheless, the error between the $J_{sc,\ calc.}$ and the J_{sc} is less than 5% for all the tested cells.

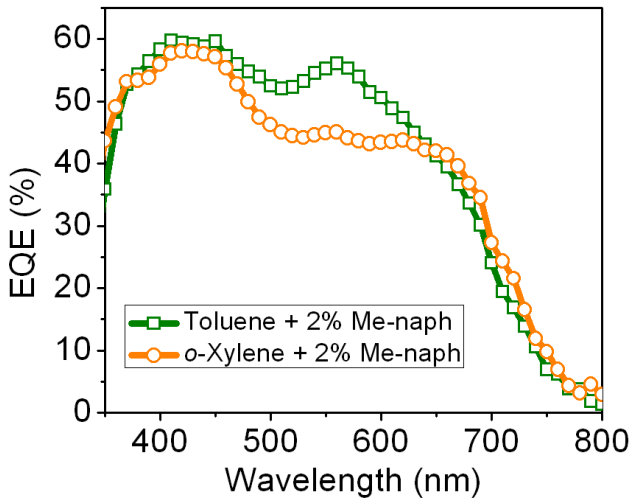

Figure 4-4. EQE spectra of PIDT-phanQ:$PC_{71}BM$ devices processed from toluene + 2% Me-naph (squares) and *o*-xylene + 2% Me-naph (circles).

4.3.1 *Morphology Analyses*

In contrast to the images in **Figure 4-3** for pure solvent cast films, AFM topography images of the PIDT-phanQ:$PC_{71}BM$ blends cast from toluene + 2% Me-naph (**Figure 4-5a**) and *o*-xylene + 2% Me-naph (**Figure 4-5d**) show much lower surface roughness and smaller domain sizes, suggesting a more homogenous distribution of the polymer and fullerene throughout the film. Estimated from the topography images, the RMS roughness values of the PIDT-

phanQ:$PC_{71}BM$ blend processed from toluene + 2% Me-naph and *o*-xylene + 2% Me-naph are 1.34 nm and 0.91 nm, respectively. The BHJ film thicknesses determined by AFM are 85 nm and 90 nm for the toluene and *o*-xylene processed films, respectively.

Note that there are shallow pinholes distributed throughout both films. The average width and the depth of the pinholes on the toluene + 2% Me-naph (*o*-xylene + 2% Me-naph) processed film are approximately 107.6 ± 32.9 nm (87.9 ± 17.3 nm) and 10.7 ± 4.8 nm (6.9 ± 2.5 nm), respectively. The mechanism of pinhole formation is unclear, but may relate to the late evaporation of the high-boiling-point Me-naph. Regardless, the existence of these pinholes appears not to affect the device performance, probably because the depth of the pinholes is less than the entire BHJ layer thickness. Nanometer-scale domains are evident in both the 1×1 μm^2 topography (**Figure 4-5a** and **4-5d**) and phase images (**Figure 4-5b** and **4-5e**).

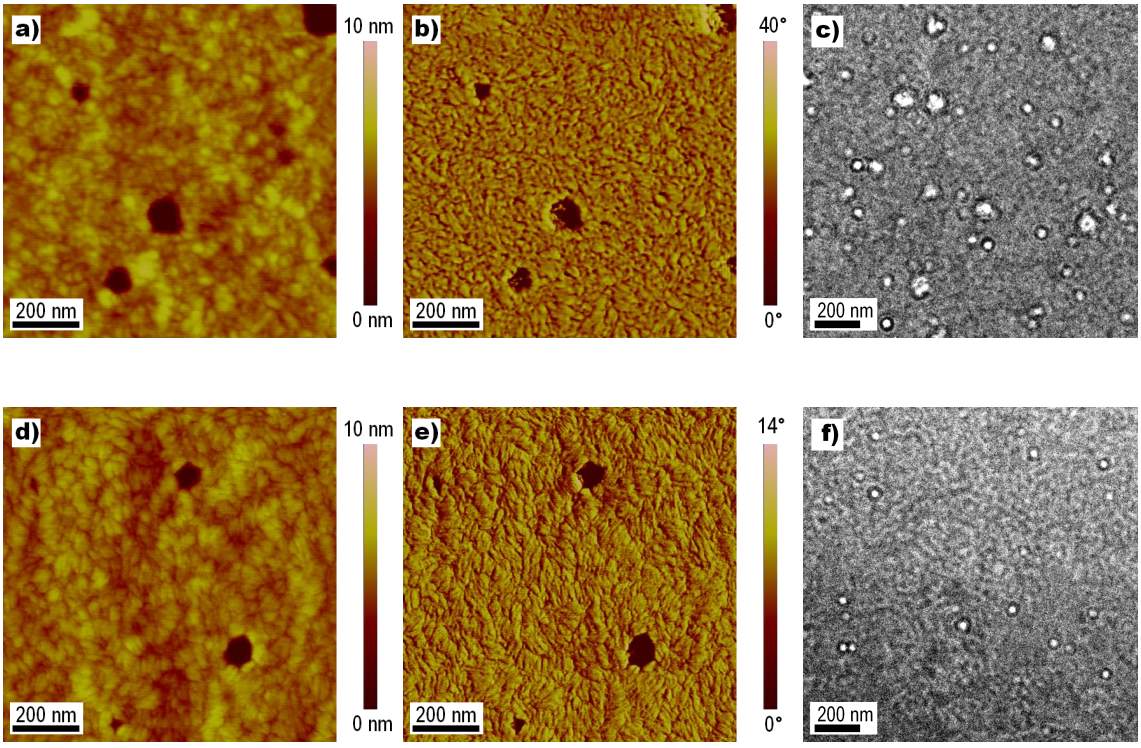

Figure 4-5. AFM topography (a, d, 1 × 1 μm^2), phase images (b, e, 1 × 1 μm^2), and TEM micrographs (c, f, scale bar indicating 200 nm) of PIDT-phanQ:$PC_{71}BM$ blend films (1:3, w/w) spin-cast from toluene + 2 % Me-naph (a, b, c) and from *o*-xylene + 2 % Me-naph (d, e, f).

In comparing the devices cast from the two solvent mixtures, the domains are finer and the domain shapes are somewhat more irregular in the toluene + 2% Me-naph processed film than those of the *o*-xylene + 2% Me-naph processed film. TEM micrographs of the BHJ layers cast from toluene + 2% Me-naph (**Figure 4.5c**) and *o*-xylene + 2% Me-naph (**Figure 4.5f**) were also taken to examine the internal nanostructure. In contrast to the images in **Figure 4.3**, much finer mixing with features of ca. 20 nm length scale can be observed in both images of films processed with Me-naph, indicating an improved morphology with larger interfacial area and interpenetrating pathways for efficient charge generation and collection. Pinholes in the films are also evident in the TEM images as the brighter circular spots.

4.3.2 *Spectroscopic Analyses*

4.3.2.1 Me-naph PIDT-phanQ:$PC_{71}BM$ Blend Photoluminescence Results at Room Temperature

For blends processed from pure toluene, the severe phase segregation (~1.1 μm domains) suggested by the AFM topography images and TEM micrographs in **Figure 4-3** appears to markedly diminish the quenching efficiency of both polymer and fullerene excitons. Evidence for this phenomenon is presented in **Figure 4-6**, where the room temperature photoluminescence (PL) for a neat film of PIDT-phanQ and a film of $PC_{71}BM$, dispersed in polystyrene, are compared with the PL data measured for PIDT-phanQ:$PC_{71}BM$ blends processed with and without Me-naph from toluene and *o*-xylene solvents. The PL measured for the pure toluene-processed blend exhibits features reminiscent of the fluorescence of each of the isolated blend components. The fluorescence fingerprints from the individual components observed in the blend suggests that a significant fraction of excitons on the polymer as well as on the fullerene decay radiatively without reaching a donor/acceptor interface.

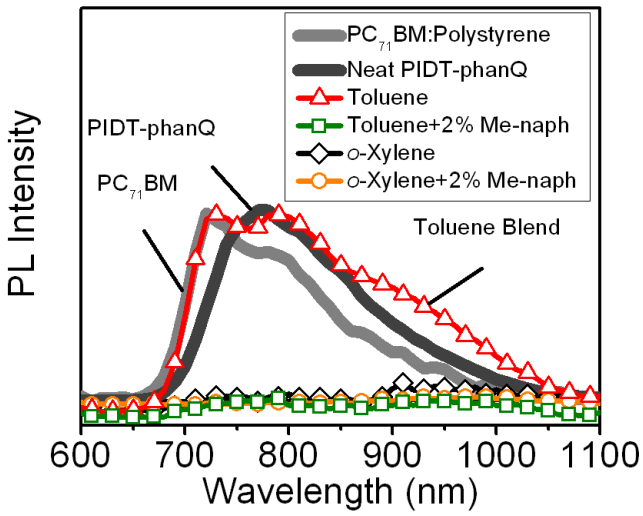

Figure 4-6. Photoluminescence (PL) signatures measured at room temperature for PIDT-phanQ:$PC_{71}BM$ blend films processed on glass from pure toluene (triangles), toluene + 2% Me-naph (squares), pure *o*-xylene (diamonds), and *o*-xylene + 2% Me-naph (circles). Normalized PL signals for $PC_{71}BM$ dispersed in polystyrene (light gray trace) and neat PIDT-phanQ polymer (dark gray trace) are also included as points of reference. Spectra measured with 455 nm excitation.

Presumably, the mismatch between the length scales of domain size (1.1 μm) and exciton diffusion length, typically tens of nm or less for most conjugated organic chromophores,[230-234] is responsible for the poor exciton quenching observed in the films cast from pure toluene. In other words, excitons decay radiatively before traveling far enough in a single phase to reach the heterojunction and undergo charge transfer quenching. Use of Me-naph as a processing additive to toluene substantially reduces large scale phase segregation, producing domains on the nanometer length scale and thus yields complete fluorescence quenching of each blend component as shown in **Figure 4-6**. Compared to pure toluene, the phase segregation is less severe for blends cast from pure *o*-xylene. Recall from **Figure 4-3** that in this case domains are

formed that are three to six times smaller than those observed for pure toluene. As a result, even for pure *o*-xylene cast samples fluorescence quenching of both blend components is observed, consistent with the superior performance of pure *o*-xylene cast films in photovoltaic devices.

4.3.2.2 Blend Photoinduced Absorption Spectroscopy Results

Photo-induced absorption spectroscopy (PIA) monitors the differential transmission of long-lived (μs - ms) optical excitations such as triplet excitons or polarons. PIA was employed to further interrogate the impact of Me-naph processing on PIDT-phanQ:$PC_{71}BM$ blends prepared from halogen-free solvents. **Figure 4-7** shows the in-phase components of the PIA spectra, plotted as the inverse natural log of the normalized differential transmission, for blends cast from pure toluene and toluene + 2% Me-naph. The pure toluene-processed film exhibits an extremely weak ($\Delta\alpha d \sim -5 \times 10^{-6}$) bleach of the polymer ground-state absorption and an induced absorption feature between 900 nm and 1600 nm of commensurate intensity, approaching the detection limit of our instrumentation. Such a PIA feature at room temperature is consistent with a low density of photoinduced PIDT-phanQ triplet excitons present in the blend.[185] Moreover, spectroscopic evidence for photoinduced charge transfer is not observed in blend samples processed from pure toluene. This observation is in qualitative agreement with the OPV device results showing negligible J_{sc} for pure toluene processing and is consistent with the poor fluorescence quenching observed. Blends cast from toluene + 2% Me-naph exhibit a PIA band ($\Delta\alpha d \sim 15 \times 10^{-6}$) at ca. 1070 nm consistent with positive polarons generated on the polymer due to photoinduced charge transfer to the fullerene.

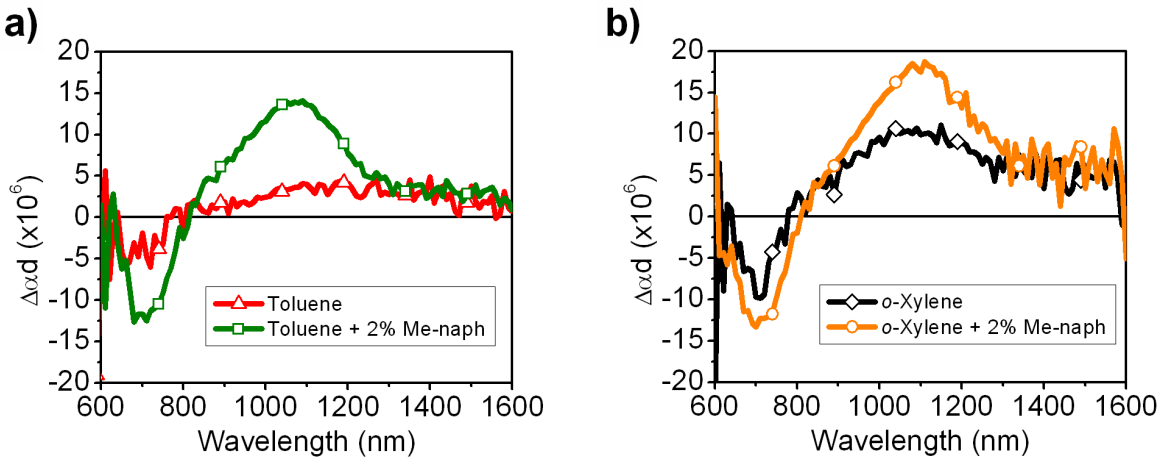

Figure 4-7. a) Photoinduced absorption (PIA) spectra for PIDT-phanQ:$PC_{71}BM$ blend films processed on glass from pure toluene (triangles) and from toluene + 2% Me-naph (squares). b) PIA spectra for PIDT-phanQ:$PC_{71}BM$ blend films processed from pure *o*-xylene (diamonds) and from *o*-xylene + 2% Me-naph (circles). All spectra were measured at room temperature with 455 nm excitation.

In contrast to pure toluene-cast blends, samples prepared with pure *o*-xylene show polymer polaron absorption, consistent with the PL quenching and device measurements. The magnitude of this polaron absorption feature increases by an additional 70% to $\Delta\alpha d = 18 \times 10^{-6}$ when the blend is processed using *o*-xylene + 2% Me-naph. This increase in polaron absorption is comparable to the percentage increase (54%) in J_{sc} of the analogous OPV devices from 6.8 mA cm^{-2} for pure *o*-xylene processing to 10.5 mA cm^{-2} observed for *o*-xylene + Me-naph. Moreover, the magnitude of the polaron signatures are roughly equal for Me-naph processed samples from toluene and *o*-xylene, which is also in agreement with the equivalent J_{sc} values obtained for the analogous devices. Frequency modulation dependence of the photoinduced polaron absorption signatures measured for films cast from toluene + 2% Me-naph, pure *o*-xylene, and *o*-xylene + 2% Me-naph were virtually indistinguishable (**Figure 4-8**) with estimated polaron lifetimes on the order of $\tau \approx 5\ \mu s$ for these films.

Taken together the PIA data form a consistent picture with the device performance, PL, and imaging data, indicating that the Me-naph additive yields a morphology that produces more photogenerated charges than the devices cast from pure solvents.

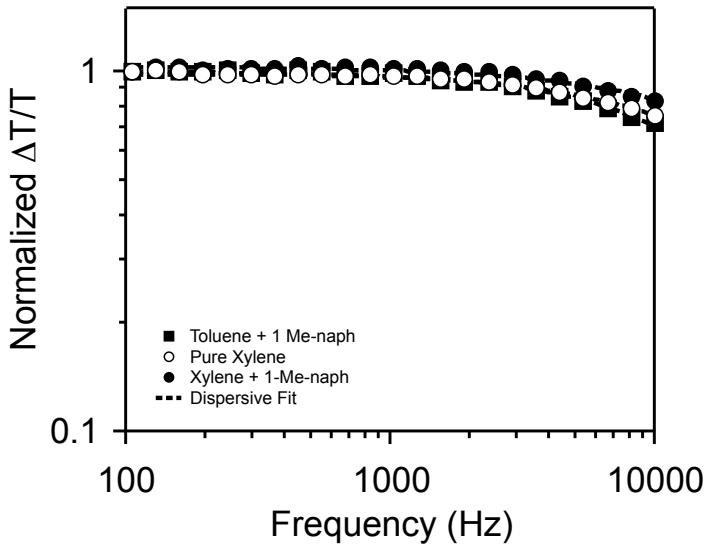

Figure 4-8. Normalized differential transmission as a function of optical modulation frequency measured using 455 nm excitation and 980 nm probe light for blended films of PIDT-phanQ:$PC_{71}BM$ processed from toluene + 2% Me-naph (filled squares, $\tau = 6\ \mu s$), pure *o*-xylene (open circles, $\tau = 5\ \mu s$), or *o*-xylene + 2%Me-naph (open circles, $\tau = 4\ \mu s$). Lifetimes were estimated based on the dispersive fits to the data shown in the plot according to $-\Delta T/T = (\Delta T/T)_o/(1+\omega\tau)$, where $(\Delta T/T)_o$ is the PIA signal magnitude at steady state, $\omega = 2\pi f$ with f being the modulation frequency in Hz, and τ is the lifetime.

4.4 Conclusion

In summary, we have studied the effect of using halogen-free solvents for processing BHJ blends comprising PIDT-phanQ and $PC_{71}BM$. Employing Me-naph as a processing additive for either toluene or *o*-xylene yielded performance of PCE = 6.1% in optimized devices, nearly

equivalent to that obtainable with halogenated solvents, while processing from pure toluene or *o*-xylene yielded performance much worse than devices prepared from halogenated solvents, employing Me-naph as a processing additive for either toluene or *o*-xylene yielded performance of PCE = 6.1% in optimized devices, just below that obtainable with halogenated solvents. Both AFM topography and TEM micrographs revealed the emergence of finer phase separation of PIDT-phanQ:$PC_{71}BM$ blends when using Me-naph. Complementary PL and PIA studies confirmed that the observed changes in morphology favorably impacts exciton quenching and the yield of long-lived charges. This work demonstrates the viability of the additive strategy to halogen-free solvent systems, which could be an important step further towards the realization of large scale manufacturing of high efficiency OPV devices.

4.5 Experimental Section

Mn and DPI of PIDT-phanQ determined by GPC were about 92 kg mol^{-1} and 2.6, respectively. PIDT-phanQ:$PC_{71}BM$ (1:3 w/w) were dissolved in toluene (20 mg ml^{-1}) or *o*-xylene (30 mg ml^{-1}) with or without the additive Me-naph. All solutions were stirred on a hotplate at 90 ºC overnight under inert atmosphere. Solar cells were fabricated in the conventional geometry. ITO coated glass substrates (15 Ω per square) were pre-cleaned by wet cleaning and then oxygen plasma treated for 30 s. PEDOT:PSS (50 nm) were spin-coated on clean ITO substrates and annealed at 140 ºC in ambient, followed by spin-coating the active layers on PEDOT:PSS covered ITO from filtered (0.20 μm PTFE syringe filter) PIDT-phanQ:$PC_{71}BM$ solutions. Toluene-based and *o*-xylene-based solutions were spin-coated on at 2000 rpm and 3000 rpm for 120 s, respectively. The active layers were annealed at 110 ºC for 10 min prior to cathode evaporation (30 nm Ca/100 nm Al). The mask patterns defined the device area to be 10.08 mm^2.

AFM measurements were performed with a Veeco multimode AFM with a Nanoscope III controller operating in tapping mode on the exposed area between the metal electrodes after the photovoltaic properties of the devices were characterized. An FEI Tecnai G2 F20 TEM operated at 200 kV was employed for bright field TEM imaging. To prepare a PIDT-phanQ:$PC_{71}BM$ BHJ thin film for TEM imaging, the devices were soaked in deionized water to dissolve the PEDOT:PSS and float the BHJ layer. The PL and PIA measurements were performed as previously described[235] using standard lock-in detection methods.[236] All PL data have been corrected for detector response.

Device *J-V* measurements were performed under a nitrogen atmosphere using a Keithley 2400 source meter. A 450W xenon arc lamp (Oriel) with an AM 1.5 global filter was operating at 100 mW cm^{-2} to simulate the AM 1.5G solar irradiation. The illumination intensity was corrected by using a silicon photodiode with a protective KG5 filter calibrated by the National Renewable Energy Laboratory (NREL). The spectral photocurrent was recorded under monochromatic illumination also from the 450W xenon lamp in ambient atmosphere. The incident beam was chopped with a mechanical chopper, and the photocurrent was recorded with a lock-in-amplifier (Stanford Research Systems SR830).

Chapter 5. STRONG PHOTOCURRENT ENHANCEMENTS IN HIGHLY EFFICIENT FLEXIBLE ORGANIC SOLAR CELLS BY ADOPTING A MICROCAVITY CONFIGURATION

5.1 INTRODUCTION

Organic photovoltaics (OPV) based technology has potential to provide cost effective solar energy conversion from solution-processed light-weight, flexible, and large-area devices.[237-239] Due to limitation of the low charge carrier mobility of organic semiconductors, the optimal thickness of the photoactive layer in most OPV devices is often ~100 nm in order to avoid serious charge recombination loss. However, this may cause insufficient light absorption and inhomogeneous electromagnetic field distribution due to coherent interference between the transmitted and reflected waves. Both effects can compromise the collection of the incident sunlight, especially at wavelengths with lower absorption coefficients such as those near the band edge of the semiconductors.

To address this deficiency in absorption, various light-trapping approaches have been proposed. For example, a common approach is to introduce an optical spacer[240,241] to modulate the phases of the standing electromagnetic waves to eliminate absorption dead zones from the photoactive layers. Other strategies such as multi-junction stack,[242-244] plasmonics,[245-249] diffraction gratings,[250,251] photonic crystal,[252] microlens,[253] and wrinkled photonic structures[254] have also been proposed to alleviate this problem.

In addition to the aforementioned strategies, the application of microcavity architecture represents a promising alternative for OPV devices.[255-261] The term microcavity refers to an optical resonator structure that has a spacer layer sandwiched by two reflecting faces. Light bounded inside a microcavity travels back and forth between the reflectors until getting absorbed or escaping from the device. Due to coherent interference, radiations having the resonant frequencies will be reinforced and the other out-of-phase waves will be depressed. Such

improved optical confinement through multi-reflection can extend the length of absorption path and potentially reduce collection loss without using thick photoactive layers.

Although the stratified structures of OPV devices resembles a microcavity geometry, the commonly used highly transparent conducting electrode such as indium tin oxide (ITO) in OPV devices will allow the unabsorbed photons to escape from the devices easily. This makes the ordinary OPV devices function as a very weak and inefficient microcavity. A stronger microcavity can be realized by replacing the ITO electrode with a more reflective transparent metal thin film[262,263] to enhance the optical confinement and eliminate problems associated with ITO electrode, such as poor flexibility, limited lateral conductance, high temperature processing, and low natural reserve of indium which strongly limit the development of OPV devices.[264,265]

However, unlike the electrically pumped optoelectronic devices such as organic light-emitting diodes (OLED),[266-270] using highly reflective mirrors for optically pumped devices like OPV cells on both ends of the cavity can significantly hinder light entrance and degrade the device performance. Furthermore, strong resonance effects can lead to narrow spectral distribution, which is disadvantageous for harvesting broadband radiation from the sun. Therefore, careful control of the optical field distribution and resonance effects is very crucial for achieving balance between the entry and the confinement of the incident radiations.

Recently, the performance of OPV devices adopting the ultrathin metal films (UTMF) microcavity structures has been progressively improved to reach comparable power conversion efficiency (PCE) with those of regular ITO-based devices using the same photoactive organic semiconductors.[255,256,259,261,263,271] These encouraging results have affirmed the feasibility of using UTMF electrodes to replace ITO in OPV and many other optoelectronic devices. However, the optical resonant cavity approach has yet to demonstrate significant improvements in

enhancing light collection for high efficiency OPV devices like other aforementioned light-trapping approaches.

In this chapter, we demonstrate PIDTT-DFBT:$PC_{71}BM$ BHJ devices in an ITO-free microcavity structure that reach high PCE of 8.5% on both glass and flexible plastic substrates, which corresponds to ~20% improvement in PCE when compared to the ITO-based devices. The significantly enhanced performance is ascribed to the substantially improved photon collection by resonant microcavity structure. Optical models based on the transfer matrix method (TMM) have been employed to assist understanding and designing the OPV devices. The results from strongly enhanced absorption and the possibility to use ITO-free structure show the promise of applying the microcavity architecture on OPV devices.

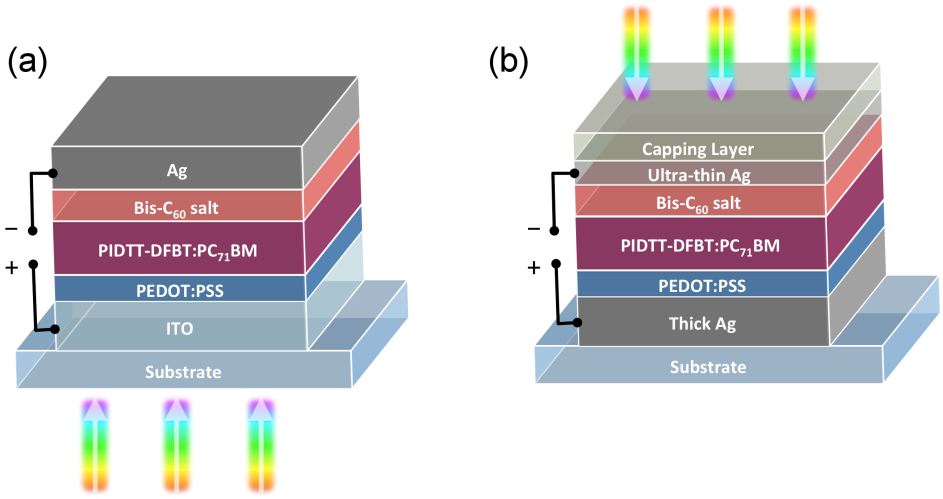

Figure 5-1. Device configurations studied in this work: (a) Normal ITO-based OPV device configuration (b) Microcavity configuration using semitransparent Ag film and top-capping light incoupling layer as the optical incident electrode.

5.2 Optical Model Built on Transfer Matrix Method

An optical model based on transfer matrix method (TMM) is established to simulate how incident light is distributed and collected in OPV devices. TMM has been demonstrated as a useful tool for understanding the optical field distribution within the layer structures of OPV devices to estimate the potential achievable photocurrent. Here the optical model is briefly described.

It is assumed that a multilayer OPV device is composed of m layers. The individual layer *j* (*j*=1,2, ..., m) has thickness of d_j and wavelength–dependent complex indices of refraction, $\bar{n}_j = n_j + ik_j$. The device is embedded between two semi-infinite layers (*j* = 0 and *j* = m+1), which are the substrate (glass or poly(ethylene terephthalate) (PET)) and air in our cases. The multilayer is illuminated along the surface normal direction *x*.

At an interface between layer *j* and *k*, the propagation of the optical field is described by the interface matrix I_{jk}.

$$\begin{bmatrix} E_j^+ \\ \bar{E}_j^- \end{bmatrix} = I_{jk} \begin{bmatrix} E_k^+ \\ \bar{E}_k^- \end{bmatrix} = \begin{bmatrix} \frac{1}{t_{jk}} & \frac{r_{jk}}{t_{jk}} \\ \frac{r_{jk}}{t_{jk}} & \frac{1}{t_{jk}} \end{bmatrix} \begin{bmatrix} E_k^+ \\ \bar{E}_k^- \end{bmatrix}$$

where $\bar{E}_j^{\pm}$ and $\bar{E}_k^{\pm}$ are the components of the optical electric field propagation in the positive (+) and negative (-) direction in the adjacent layers j and k, respectively. For a plane wave propagation along the surface normal, the Fresnel complex reflection and transmission coefficients are $r_{jk} = (\bar{n}_j - \bar{n}_k)/(\bar{n}_j + \bar{n}_k)$ and $t_{jk} = 2\bar{n}_j/(\bar{n}_j + \bar{n}_k)$, respectively. The propagation through a layer *j* causes absorption and changes the phase, as described by the layer matrix L_j.

$$L_j = \begin{bmatrix} e^{-i\xi_j d_j} & 0 \\ 0 & e^{i\xi_j d_j} \end{bmatrix}$$

where $\xi_j = (\frac{2\pi}{\lambda})\overline{n}_j$. The electric field in the two outermost layers j = 0 and j = m+1 are related via the transfer matrix S as

$\begin{bmatrix} \overline{E}_0^+ \\ \overline{E}_0^- \end{bmatrix} = S \begin{bmatrix} \overline{E}_{m+1}^+ \\ \overline{E}_{m+1}^- \end{bmatrix}$, where $S = \begin{bmatrix} S_{11} & S_{12} \\ S_{21} & S_{22} \end{bmatrix} = (\prod_{n=1}^{m} I_{(n-1)n} L_n) \cdot I_{m(m+1)}$.

The reflection coefficient $r = \frac{\overline{E}_0^-}{\overline{E}_0^+} = \frac{S_{22}}{S_{11}}$, and the transmission coefficient $t = \frac{\overline{E}_{m+1}^+}{\overline{E}_0^+} = S_{11}^{-1}$. The absorption efficiency of a multilayers stack is then $\eta_A = 1 - T - R$, where transmissivity of the multilayer structure $T = \frac{|t|^2 \overline{n}_{m+1}}{\overline{n}_0}$ and reflectivity of the multilayer structure $R = |r|^2$. The device is typically supported by a substrate with a thickness of 0.1-1mm >>λ. Hence, the effect of the substrate is included by correcting T and R for reflections at the air/substrate and substrate/multilayer interfaces rather than by including it directly in the transfer matrix calculation, *viz*

$$R' = \frac{R^* + R}{1 + R^* R}$$

$$T' = \frac{T^* T}{1 + R^* R}$$

with $R^* = \left|\frac{1-\overline{n}_0}{1+\overline{n}_0}\right|^2$ and $R = \left|\frac{2}{1+\overline{n}_0}\right|^2$, where $\overline{n}_0$ is the refraction index of the substrate. The absorption efficiency $\eta_A = 1 - T' - R'$. To obtain the electric field within layer j, we note that the total multilayer transfer matrix is

$S = S_j^- L_j S_j^+$,

with

$$S_j^- = (\prod_{n=1}^{j-1} I_{(n-1)n} L_n) \cdot I_{j(j-1)}$$

$$S_j^+ = (\prod_{n=j+1}^{m} I_{(n-1)n} L_n) \cdot I_{m(m+1)}$$

The electric field propagating in the positive direction in the layer *j* at the left interface is related to the incident plane wave by

$$\frac{\overline{E_j^+}}{\overline{E_0^+}} = t_j^+ = \frac{\frac{1}{S_{j11}^-}}{1 + \frac{S_{j12}^- S_{j21}^+}{S_{j11}^- S_{j11}^+} e^{i2\xi_j d_j}}$$

The total electric field at an arbitrary position inside layer *j* is given in terms of the electric field of the incident wave by

$$E_j(x) = E_j^+(x) + E_j^-(x) = \left(t_j^+ e^{i\xi_j x} + t_j^- e^{-i\xi_j x}\right) E_0^+$$

The time averaged absorbed power as a function of position is then

$$Q_j(x) = \frac{4\pi c \varepsilon_0 k_j n_j}{2\lambda} \left|\overline{E}_j(x)\right|^2,$$

where *c* is the speed of light and ε_0 is the permittivity of free space.

Thus, the exciton generation rate can be derived from $G_j(x) = \left(\frac{\lambda}{hc}\right) Q_j(x)$. By integrating $G_j(x)$ on all the wavelengths where the materials have absorption, the spatial distribution of exciton generation as a function of position in the active layer can be plotted.[272]

5.3 PIDTT-DFBT:$PC_{71}BM$ Device in Regular ITO-based Structure: Effects of Varying Photoactive Layer Thickness

PIDTT-DFBT:$PC_{71}BM$[201] BHJ device is employed as the sample system because of its good performance demonstrated from a relative thin photoactive layer (~80 nm) and low loading of the semiconducting polymer PIDTT-DFBT (25 wt%) in the photoactive blend, which suggest a substantial fraction of the incident light may not be completely absorbed. To investigate how much light is collection affected, optical simulations are performed. The simulated device configuration is: glass (1 mm)/ITO (120 nm)/PEDOT:PSS (50 nm)/PIDTT-DFBT:$PC_{71}BM$ (0 – 1 μm)/Bis-C_{60} salt (8 nm)/Ag (120 nm). The complex refractive indices of each composing layer

are acquired by spectral ellipsometric technique and shown in **Figure 5-2**. The light source is assumed to be the AM 1.5 global solar spectrum at intensity of 1000 W m^{-2}. By assuming a unity photon-to-electron conversion, i.e. IQE = 100% at all wavelengths, we can calculate the theoretical lossless photocurrent ($J_{ph\text{-}100\%IQE}$) of each simulated condition. The thickness of the photoactive layer (t_{BHJ}) is varied from 0 to 1 μm, and the dependence of $J_{ph\text{-}100\%IQE}$ on t_{BHJ} are plotted in **Figure 5-3**.

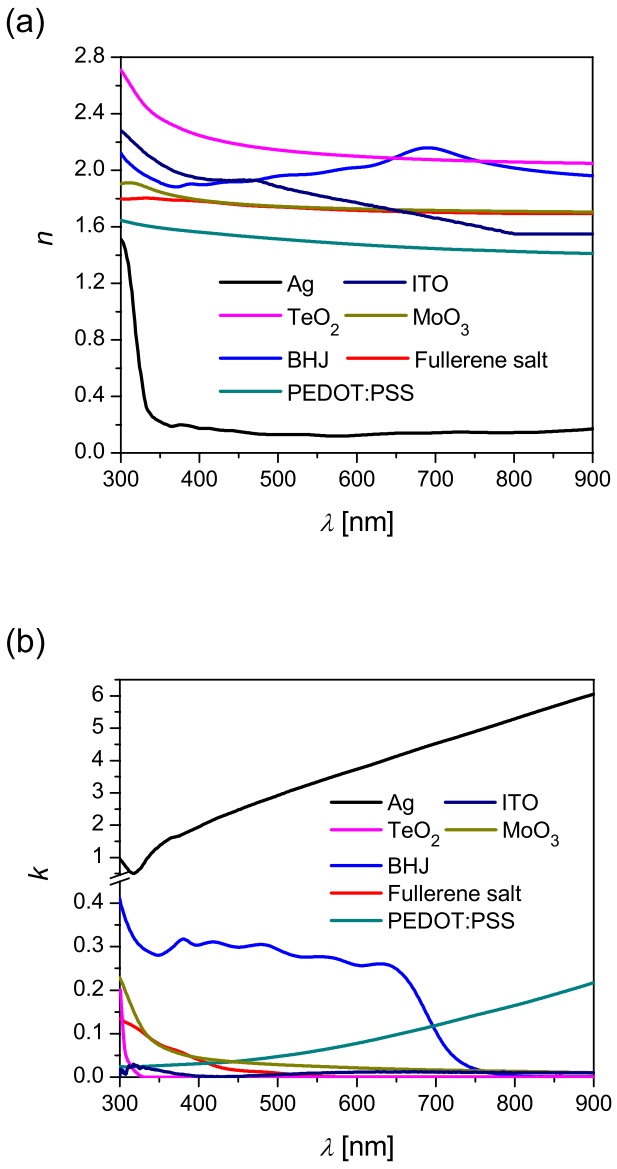

Figure 5-2. (a) Real parts and (b) imaginary parts of the complex refractive indices $\overline{n} = n + ik$ of the materials acquired by variable angle ellipsometric spectroscopy.

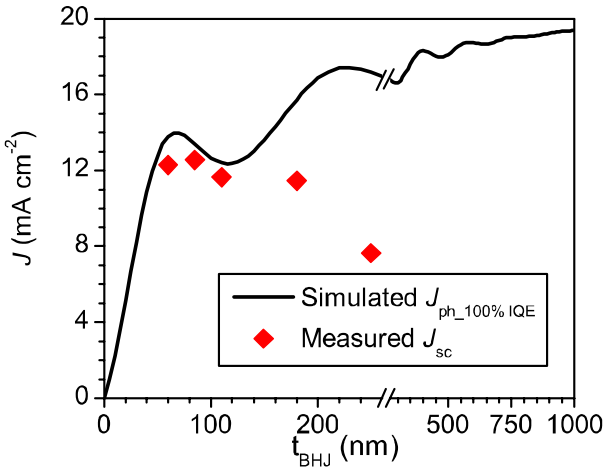

Figure 5-3. Calculated lossless photocurrent ($J_{ph\_100\%IQE}$) and the measured short-circuit current (J_{sc}) of the PIDTT-DFBT:$PC_{71}BM$ OPV devices in the regular ITO-based device configuration plotted against the thickness of the BHJ layer (t_{BHJ}).

The $J_{ph\text{-}100\%IQE}$ curve shows common oscillating characteristics due to coherent interference.[273,274] The best condition for thin absorber layer appears to be at t_{BHJ} = 70 nm with $J_{ph\text{-}100\%IQE}$ reaching 13.97 mA cm^{-2}. On the other hand, the $J_{ph\text{-}100\%IQE}$ of device with thick absorber layer (t_{BHJ} = 1 μm) can reach > 19 mA cm^{-2}. The large photocurrent variation between different thicknesses of absorber layers in devices clearly reveals the substantial absorption loss when the t_{BHJ} is < 100 nm. However, as mentioned earlier, the finite charge mobility of the organic semiconductors is the main limiting factors for using thicker photoactive layers. **Figure 5-3** shows the dependence of short-circuit current (J_{sc}) of actual OPV devices on several different t_{BHJ} (60 nm, 85 nm, 110 nm, 180 nm, 250 nm). Among all the thicknesses tested, the highest J_{sc} is obtained for device with a t_{BHJ} of ~ 85 nm, which is similar to the optimal condition reported by Xu *et al.*[201] However, the devices with the thicker photoactive layers (t_{BHJ} = 180 nm or 250 nm) show seriously declined J_{sc} and fill factors (**Figure 5-4**), implying the devices suffer

increased charge recombination loss, which offset the improved absorption from using thicker films. Based on combined optical simulations and device measurements, we conclude that it is possible to further improve the PIDTT-DFBT:$PC_{71}BM$ system if optical dissipation can be inhibited without using an electrically thick BHJ layer.

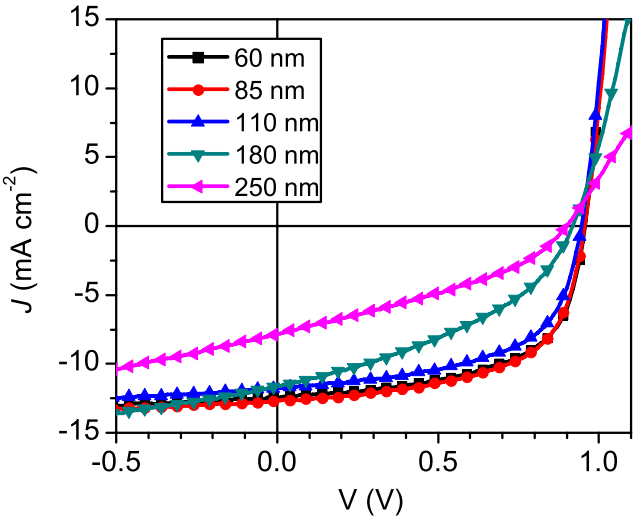

Figure 5-4. *J-V* characteristics of PIDTT-DFBT:$PC_{71}BM$ devices in the normal ITO-based configuration with different active layer thicknesses (t_{BHJ} = 60 nm, 85 nm, 110 nm, 180 nm, and 250 nm).

5.4 PIDTT-DFBT:$PC_{71}BM$ IN MICROCAVITY STRUCTURE

5.4.1 *Optical Simulations of the Microcavity Device*

As mentioned earlier, it is possible to apply the microcavity confinement effect to extend the absorption path for harvesting more photons without using a thick absorber layer. To prove this, we replaced ITO with an ultrathin Ag film as the optical incident electrode to enhance light trapping of the OPV device. The device structure is shown in **Figure 5-1b**. In this configuration, the cavity is established between a transparent ultrathin Ag cathode and an opaque Ag anode,

which reverse the direction of light incidence. Such kind of top-illuminated configuration is appealing for their applicability to opaque or low-cost substrates like papers or metal foils.[275,276]

Ag is used at both electrodes due to its great conductivity and ductility. An additional top-capping optical spacer layer is also introduced on top of the transparent Ag electrode. Such optical spacer usually serves as the anti-reflecting or light in-coupling layer in a microcavity configuration and is critical in determining the electric field distribution through the regulation of the optical interference similar to the functions of regular internal optical spacers.[256,259,277] However, unlike the regular optical spacers, the light in-coupling layer is not connected with the electrical loop of the OPV cell thus it only serves the optical function without participating in the electrical operation of the OPV device. As a result, it is feasible to use a less conductive material or a thicker layer without introducing resistive loss to the device. In literature, there are various materials that can be used to couple with UTMF electrodes,[255,259,277-280] however, the selection/design rules are not clearly elaborated.

In order to estimate the achievable photocurrent and find suitable materials for the top-capping spacer layer, optical simulations based on TMM again are performed using virtual materials with variable refractive indices. The real part (n_{cap}) of the refractive indices of the virtual capping layer is assumed to be wavelength-independent. The virtual materials are also assumed to be non-absorptive so the imaginary parts (k_{cap}) of the refractive indices are null. $J_{ph\text{-}100\%IQE}$ of device with the structure shown in **Figure 5-1b** is calculated by sequentially varied n_{cap} from 1.0 to 3.0. For each n_{cap}, the thickness of various composing layers in the microcavity device is simultaneously optimized to assure the optimal device configuration is obtained.

To show the impact of the top-capping optical spacer on light harvesting, the $J_{ph\text{-}100\%IQE}$ is plotted as a function of the refractive index n_{cap} (**Figure 5-5a**). When no capping layer (n_{cap}

equals to n_{air} = 1.0) is used, a decent $J_{ph\text{-}100\%IQE}$ (14.51 mA cm^{-2}) can be obtained. Once the capping layer is introduced, the $J_{ph\text{-}100\%IQE}$ can be further improved for all the calculated n_{cap} values (1.1 – 3.0). From the results shown in **Figure 5-5a**, it indicates that a wide range of n_{cap} are suitable for improving the absorption efficiency of the microcavity device; the $J_{ph\text{-}100\%IQE}$ reaches its plateau of ~15.9 mA cm^{-2} when the n_{cap} is between 1.7 and 2.7. The best condition occurs at n_{cap} = 2.2 with a t_{cap} of 35 nm, giving a peak value of $J_{ph\text{-}100\%IQE}$ = 15.99 mA cm^{-2}, which is considerably better than that obtained from the ITO-based configuration.

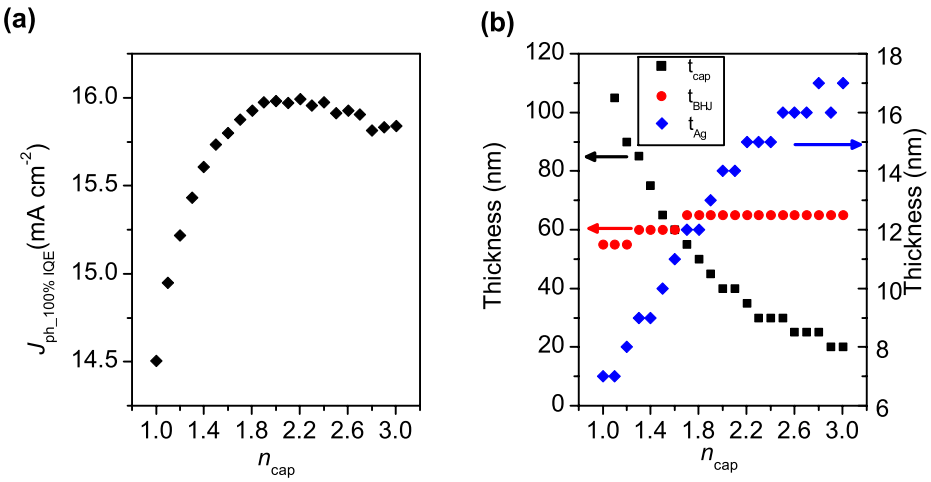

Figure 5-5. (a) Optimal calculated lossless photocurrent ($J_{ph\_100\%IQE}$) of the microcavity devices using virtual top-capping spacer layer as a function of the refractive index (n_{cap}) (b) The thicknesses of the active layer (t_{BHJ}), capping layer (t_{cap}), and ultrathin Ag electrode (t_{Ag}) in the optimal conditions as functions of the refractive index (n_{cap}).

Figure 5-5b also shows how the optimal thickness of the active layer (t_{BHJ}), capping layer (t_{cap}), and thin Ag electrode (t_{Ag}) changes when the n_{cap} is sequentially varied. The optimal t_{BHJ} increases from 55 nm to 65 nm, the optimal t_{cap} decreases from 105 nm to 20 nm, and the optimal t_{Ag} increases more than twofold from 7 to 17 nm, respectively, as n_{cap} changing from 1.0

to 3.0. To our surprise, using thinner metal electrode is not optically ideal for microcavity-based devices but is explainable by better light trapping provided by the thicker metal reflector. Note that being able to use a thicker semitransparent metal layer is advantageous for OPV development because the R_s of UTMF can increase substantially if the film thickness is reduced to near its percolation threshold (roughly ~10 nm) due to film discontinuity and inhomogeneity.[263,278] The superior conductance of a thicker metal film will facilitate the fabrication of large-area OPV devices.[281,282] The result from **Figure 5-5a** suggests that the application of a capping layer with higher n_{cap} values is potentially beneficial because the association of increasing electrode conductance.

Based on the simulations, we decide to perform simulations using tellurium oxide (TeO_2) as the top-capping optical spacer because of its relatively high refractive indices (n_{TeO2} ~ 2.2, **Figure 5-2**) and simplicity to be deposited via vacuum evaporation.[259] **Figure 5-6** shows the topographic plot of $J_{ph\text{-}100\%IQE}$ as a function of different thickness of t_{BHJ} and t_{TeO2}. The optimal $J_{ph\text{-}100\%IQE}$ (13.97 mA cm^{-2} at t_{BHJ} = 70 nm) of the ITO-based device is outlined by the dashed contour line. The maximum value of $J_{ph\text{-}100\%IQE}$ can reach 15.96 mA cm^{-2} when the thickness of t_{Ag}, t_{BHJ}, and t_{TeO2} is equal to 14 nm, 65 nm, and 35 nm, respectively. This $J_{ph\text{-}100\%IQE}$ number is extremely close to the best value predicted from the microcavity devices using virtual capping layers, manifesting the optical ideality of TeO_2 as the capping layer in this system.

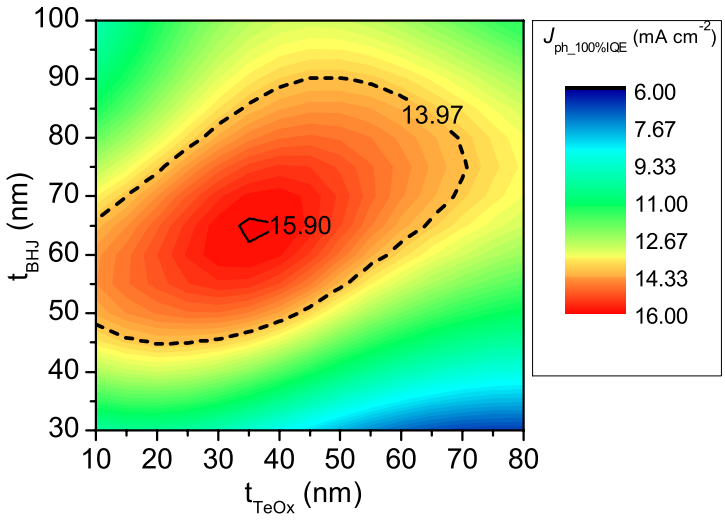

Figure 5-6. $J_{ph\_100\%IQE}$ of the microcavity device using TeO_2 top-capping layer as a function of t_{BHJ} and the thickness of the TeO_2 layer (t_{TeO2}).

5.4.2 *Device Fabrication and Characterization*

Encouraged by the significantly enhanced $J_{ph\text{-}100\%IQE}$ predicted from the simulation of microcavity-based OPV devices, we have fabricated devices with a TeO_2 capping layer. A high PCE of 8.56% could be obtained from the optimized device structure of glass/Ag (120 nm)/PEDOT:PSS (30 nm)/PIDTT-DFBT:$PC_{71}BM$ (85 nm)/Bis-C_{60} salt (8 nm)/Ag (15 nm)/TeO_2 (50 nm). The output parameters and the *J-V* characteristics of this optimized device and the ITO-based control device are shown in **Table 5-1** and **Figure 5-7a**, respectively. The EQE spectrum is shown in **Figure 5-7b**. The V_{oc} (~0.96 V) and *FF* (~0.59) of the optimized microcavity-based device remain almost identical to those of the ITO-based control device, showing the replacement of electrodes and the use of TeO_2 capping layer does not introduce any electrical loss. Moreover, the J_{sc} is significantly improved to 15.19 mA cm^{-2}, which is approximately 20% greater than that obtained from the ITO-based control device.

Table 5-1. Output parameters of the optimized devices in the microcavity configurations and the regular ITO-based configuration.

Substrate	Electrode	V_{oc} [V]	J_{sc} [mA cm^{-2}]	FF	PCE [%]
Glass	ITO	0.96	12.56 (12.63)[a]	0.60	7.21 (7.30)
Glass	Ag/TeO_2	0.96	15.03 (15.19)	0.59	8.47 (8.56)
Glass	Ag/MoO_3	0.96	13.49 (13.71)	0.59	7.66 (7.80)
PET	ITO	0.94	13.05 (13.33)	0.54	6.61 (7.07)
PET	Ag/TeO_2	0.96	14.95 (15.09)	0.58	8.37 (8.50)

[*a*] Numbers in parentheses represent the highest recorded value.

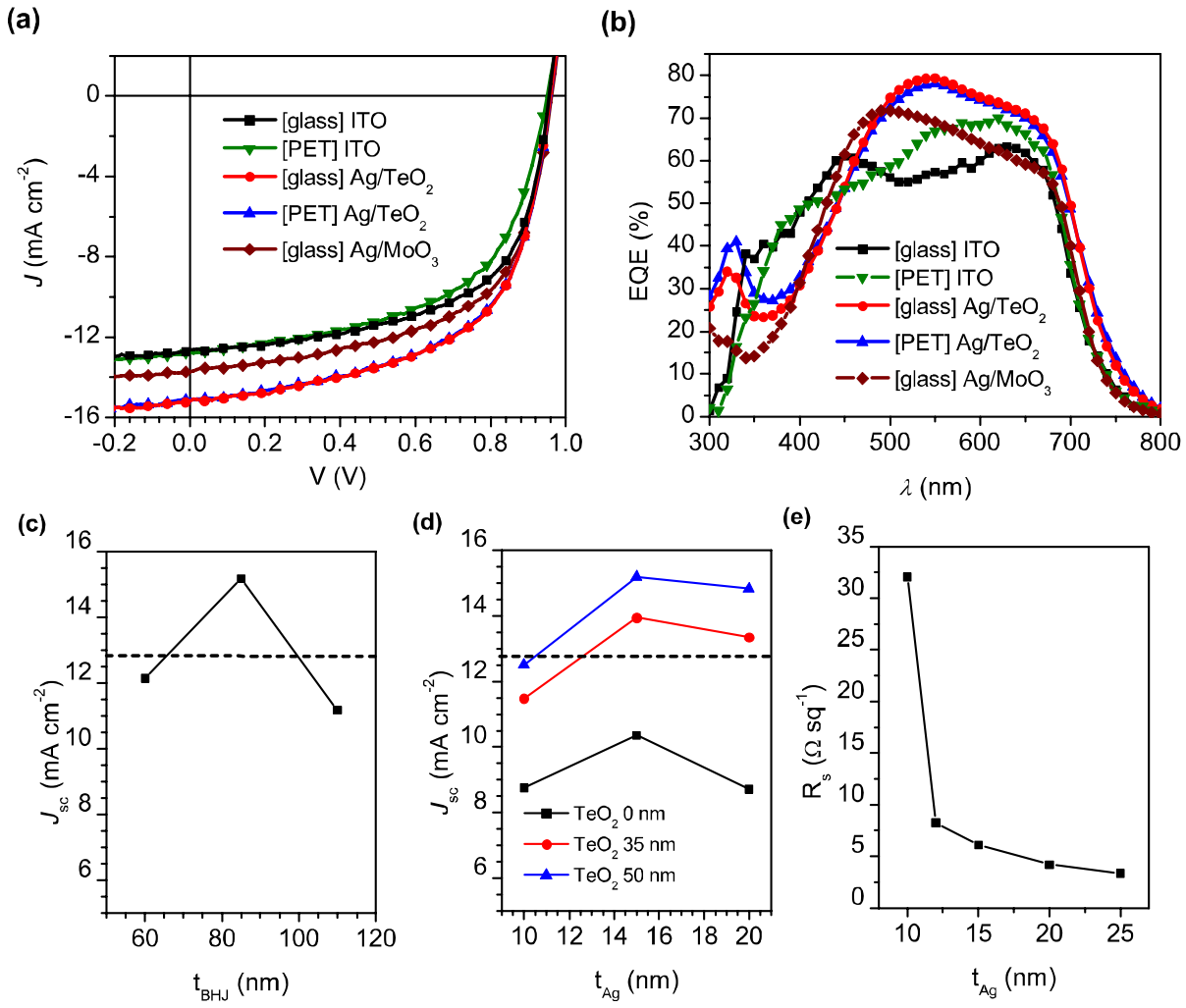

Figure 5-7. (a) *J-V* characteristics and (b) external quantum efficiencies of the best devices in the control ITO-based configuration and the microcavity configurations. (c) Short-circuit current (J_{sc}) of actual TeO_2-capped microcavity OPV devices as a function of the thickness of the photoacitve BHJ layer (t_{BHJ}) (d) J_{sc} of actual TeO_2-capped microcavity OPV devices as a function of the thicknesses of the semitransparent Ag cathode (t_{Ag}) and TeO_2. (e) Sheet resistance (R_S) of the Ag electrode as a function of t_{Ag} . Four-point probe measurements were performed on samples in the structure of glass/ PIDTT-DFBT:$PC_{71}BM$ (85 nm)/Bis-C60 salt (8 nm)/Ag (10 nm, 12 nm, 15 nm, 20 nm, or 25 nm) to determine R_S.

Figure 5-7c shows the J_{sc} of the TeO_2-capped microcavity devices as a function of t_{BHJ} while t_{TeO2} and t_{Ag} of the devices are fixed at 50 nm and 15 nm, respectively. **Figure 5-7d** exhibits the

dependence of J_{sc} on t_{TeO2} and Ag thickness (t_{Ag} = 10, 15, and 20 nm) while t_{BHJ} of the devices is kept at 85 nm as control. The horizontal dashed lines in **Figure 5-7c** and **5-7d** indicate the J_{sc} of the optimal control ITO-based device (12.56 mA cm^{-2}). Note that the t_{BHJ} and t_{TeO2} of the best device are deviated slightly from the optimal thickness predicted by the optical model. The deviations might come from the errors in the refractive index measurements and without considering any electrical contributions in the simulations. **Figure 5-7e** shows the sheet resistance (R_s) of the Ag electrodes measured by the four-point-probe technique. From the plot, t_{Ag} and the J_{sc} do not show a simple negative correlation. Although the R_s of the 10 nm Ag is higher than that of 15 nm one, the fill factor of the device with 10 nm Ag electrode ($FF \sim 0.55$) remains reasonable, suggesting the device does not suffer seriously from the resistive loss. Therefore, the improved R_s cannot be the sole contributor to the J_{sc} increments. Instead, the coherent resonance effects introduced by the more reflective electrodes are believed to be the main reason for achieving high J_{sc}.

Figure 5-7b shows the EQE spectrum of the optimized microcavity devices and the ITO-based control device. It can be seen that the EQE spectrum of the two devices look significantly different despite they use the same BHJ blend with the same thickness (t_{BHJ} = 85 nm). The spectral response of the microcavity device becomes narrower and more intense as a result of the resonance effect; the region between 450 nm to 750 nm is significantly enhanced, while the spectral response between 300 nm – 450 nm is suppressed. The net increase of light harvesting leads to significantly enhanced photocurrent. The EQE spectra of microcavity devices with different t_{Ag} and t_{TeO2} can be found in the **Figure 5-8**. Adopting the resonance effect to create relatively narrow and intense photo-response can be particularly important for the multi-junction devices through the creation of efficient sub-cells with complementary absorption.

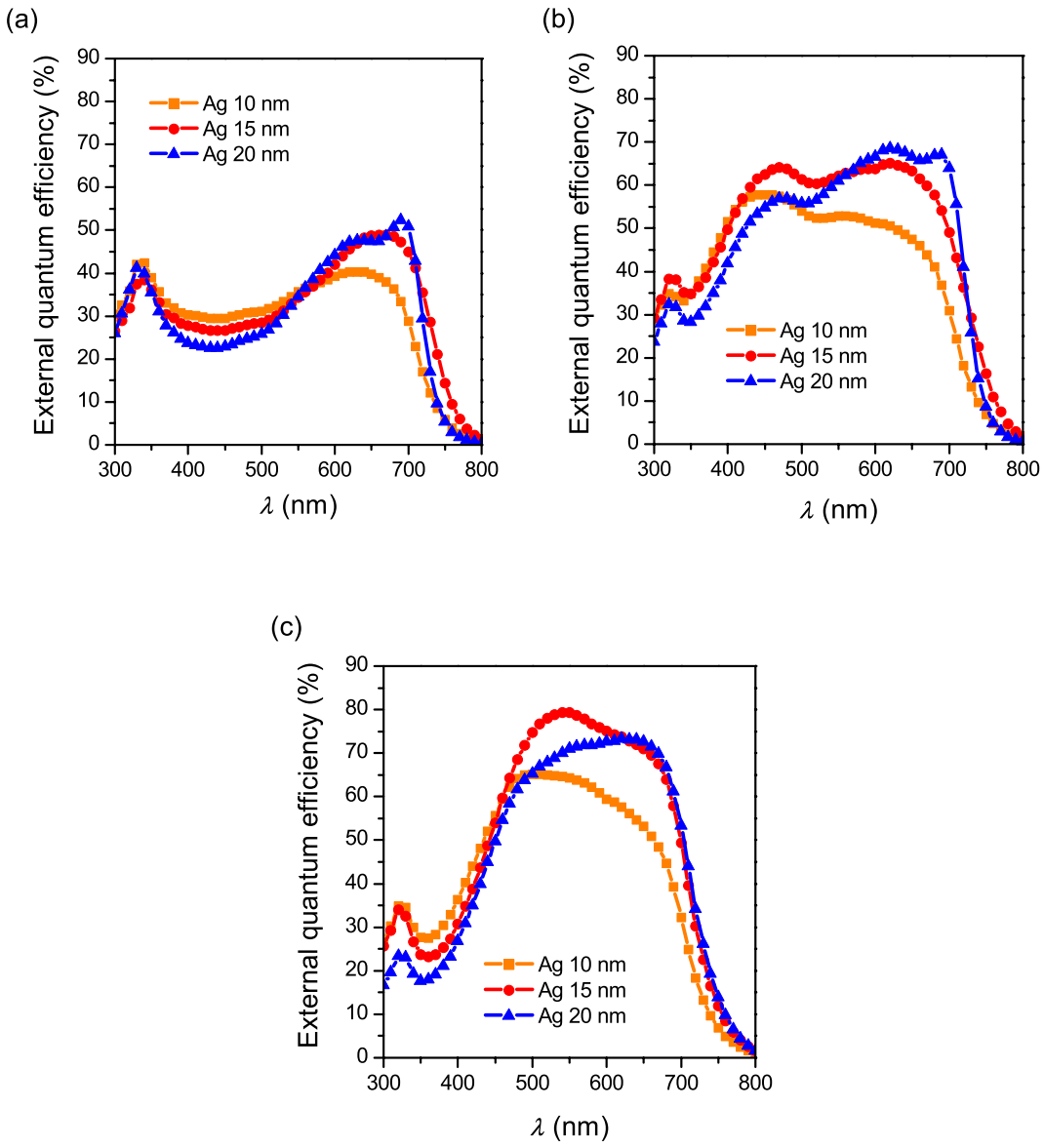

Figure 5-8. EQE of the OPV devices in the microcavity configuration as a function of the thickness of the thin Ag electrode with (a) no TeO_2 capping layer, (b) 35 nm TeO_2 capping layer, and (c) 50 nm TeO_2 capping layer.

To demonstrate the general applicability of this approach and to address the environmental concern of using TeO_2, we have also fabricated device using MoO_3 as the top-capping layer. The PCE of the device in the structure of glass/Ag (120 nm)/PEDOT:PSS (30 nm)/PIDTT-DFBT:$PC_{71}BM$ (90 nm)/Bis-C_{60} salt (8 nm)/Ag (15 nm)/MoO_3 (50 nm) can reach 7.80% (7.66%

in average). The detailed device characteristics can be found in **Table 5-1** and **Figure 5-7a,b**. Although this performance is slightly lower than that of the TeO_2-based device, it is still more efficient than the ITO-based control device, which demonstrates the microcavity strategy can be generally applicable to other capping materials. Other transparent metal oxides that have suitable optical constants and can be deposited without destroying the underlying layers such as other vacuum evaporation or solution-processed[283] techniques are also potential capping materials for such micro- cavity configuration.

5.5 Fabrication and Characterization of Flexible Devices

One prominent feature of OPV devices is their compatibility to solution process on flexible substrates. By replacing the rigid glass substrate with flexible PET films, we have also fabricated flexible devices in both the ITO-based (**Figure 5-1a**) and the TeO_2-capped top-illuminated microcavity ITO-free configurations (**Figure 5-1b**). The output parameters of the flexible devices can be found in **Table 5-1**, and the *J-V* and EQE characteristics are also compared with the rigid devices in **Figure 5-7a** and **Figure 5-7b**, respectively. The ITO-based flexible OPV device shows slightly reduced performance (PCE = 7.07%, *FF* = 0.54) compared with its rigid counterpart, which is due to reduced conductance of ITO electrode on PET substrate (t_{ITO} = 100 nm, R_s = 60 Ω sq^{-1}). In the case of the top-illuminated microcavity configuration, the performance should be irrelevant to the types of substrate used since the incident light get completely reflected by the opaque metal electrode before reaching the substrates. As expected, when the identical optimal microcavity configuration is built on PET substrate, we have observed very similar device performance (PCE = 8.50%) and spectral response curve between the best flexible and rigid microcavity devices.

5.6 CONCLUSION

In conclusion, the microcavity configuration is proved to be a promising architecture for OPV devices because it can avoid the use of brittle and expensive ITO electrode and enhance light trapping through coherent resonance effects. In this work, we demonstrate highly efficient ITO-free and flexible OPV devices adopting microcavity configurations with PCE reaching 8.5%. The optimized devices show unprecedented magnitudes of improvement on the short-circuit current and the capability of using slightly thicker Ag electrodes (15 nm) with good lateral electrical conduction, which enables them to be considered for highly efficient large-area devices.

5.7 EXPERIMENTAL SECTION

5.7.1 *Fabrication of Regular ITO-Based Control Devices*

ITO-coated glass substrates (Colorado Concept Coatings LLC) and ITO-coated PET (Sigma-Aldrich) are cleaned sequentially in detergent, DI water, acetone, and isopropyl alcohol (IPA) by successive 10 min sonication steps followed by 20 s of plasma treatment. PEDOT:PSS aqueous solution are spin-coated onto the ITO and annealed at 140 °C for 10 min. PIDTT-DFBT (4.5 mg mL^{-1}) and $PC_{71}BM$ (13.5 mg mL^{-1}) are dissolved in dichlorobenzene + 2.5 vol% 1-chloro-naphthalene as the solvent additive, stirred overnight at 80 °C, and then spin-coated under nitrogen atmosphere to obtain a film of ~85 nm, followed by thermal annealing at 110 °C for 10 min. For the devices required different active layer thicknesses, the concentration of the solution is adjusted accordingly. The Bis-C60 surfactant film (~8 nm) is also spin-cast under nitrogen atmosphere and annealed at 110 °C for additional 5 min. Finally, a 120 nm-thick Ag film is evaporated through a mask to define a device area of 4.5 mm^2.

5.7.2 *Fabrication of the OPV Devices in the Microcavity Configurations*

Plain glass and plain PET substrates are cleaned via identical sonication steps and plasma treatment as the ITO-coated substrates and deposited with 120 nm Ag bottom electrodes. To deposit PEDOT:PSS (30 nm) on the bottom Ag electrode, the aqueous PEDOT:PSS solution is diluted 4 times with IPA to match the surface energy between the PEDOT:PSS solution and the substrate. The photoactive layers and the surfactant layers are spin-cast and annealed at the same conditions as the control devices. Top ultrathin Ag electrodes are evaporated at 5 Å $^{s-1}$ to the desired thicknesses (10, 15, or 20 nm) through a mask to define a device area of also 4.5 mm^2. Last step the TeO_2 or MoO_3 capping layers are deposited at the rate of 0.2 Å s^{-1} via thermal evaporation.

5.7.3 *Instruments and Device Characterizations*

The complex refractive indices are acquired by a variable angle spectroscopic ellipsometer (VASE) from J.A. Woollam Co. Device characterizations are performed under inert environment to prevent the device performance affected by moisture and oxygen. A Keithley 2400 source meter is used to record the photocurrent for the *J–V* characteristics and the EQE measurements. A 300 W xenon arc solar simulator equipped with an AM 1.5G filter is used to simulate the 1 sun illumination. The illumination intensity was corrected by a calibrated KG5 color filter covered silicon photodiode. Note that the differences of the J_{sc} and calculated short-circuit current density from the integration of the EQE spectra are less than 5% for all the test cells.

Chapter 6. SEMI-TRANSPARENT POLYMER SOLAR CELLS WITH 6% PCE, 25% AVERAGE VISIBLE TRANSMITTANCE, AND COLOR RENDERING INDEX CLOSE TO 100 FOR POWER GENERATING WINDOW APPLICATIONS

6.1 INTRODUCTION

The feasibility of realizing semi-transparent device structures shows promise for the use of OPV devices in novel applications. For example, semi-transparent OPV (ST-OPV) cells can be stacked into multi-junction devices[284] to enhance sunlight harnessing for higher device performance. Besides being incorporated in multi-junction devices, ST-OPV devices are also identified as promising candidates for power-generating windows by integration with conventional see-through elements such as building and automobile glasses. Building integration can be particularly interesting since buildings have large surface areas for sunlight harnessing and have been recognized as one of the major energy consumers and carbon dioxide emitters. Therefore, generating clean energy on site from building integrated photovoltaics (BIPV) could potentially reduce the expense of energy and mitigate the pollution in a very appreciable scale.

Current performance of ST-OPVs, however, is much lower than their opaque counterparts, which hinders their applications for power generating windows. For instance, ST-OPV cells based on the most commonly used active materials poly(3-hexylthiophene) (P3HT) and $PC_{61}BM$ blends show relatively low performance,[73,285,286] and their limited spectral absorption results in a strong color bias of the transmitted light. Though colored windows are useful for the aesthetic and decorative purposes, windows with minimal chromatic alternations of the light source that allow the transmission of natural color spectrum are generally preferred for environments required high quality of illumination. The fast and continuous development of novel organic photovoltaic materials[287,288] can be leveraged in realizing high efficiency ST-OPV cells with desirable optical effects. However, systematic studies and optimization of the optical properties of ST-OPV for window integration are only at the early stage of their developments. Ameri *et al.*[289] suggested that ST-OPV cells based on PCPDTBT and $PC_{71}BM$ blend can provide a more

natural transparency color perception than the solar cells based on P3HT:$PC_{71}BM$ blend. Colsmann *et al.*[290] demonstrated that ST-OPV cells based on the blend of $PC_{71}BM$ and PSBTBT are suitable candidates for window applications due to the remarkable transparency color perception and color rendering capacity afforded by the transmitted light. However, further breakthroughs, especially on the performance of ST-OPV cells, rely on the use of more advanced materials and conscious optical engineering.

In this chapter, we present ST-OPVs in the inverted structure utilizing blends of $PC_{71}BM$ and PBDTTT-C-T (**Figure 6-1**).[47] Conjugated polymers based on the BDT and TT alternating units are by far the most successful type of donor materials for organic photovoltaics that have shown excellent PCE.[44,177] BHJ solar cells based on PBDTTT-C-T has demonstrated PCE as high as 7.6%.[47] The good performance and relatively flat spectral response curve across the visible spectrum makes this donor-acceptor composite promising for applications required high optical quality. By tuning the thickness of the reflective metal electrode, the PCE of the ST-OPV devices ranging from 7.56% to 4.25 % with corresponding transparency ranges from 2% to 36% are demonstrated. The transmitted light of these devices under AM1.5G illumination exhibits extraordinary transparency color perceptions and rendering capacities, favoring their use for real-life window applications.

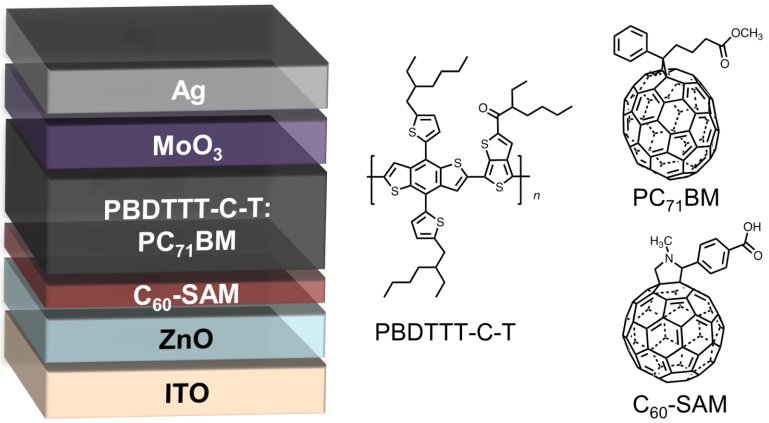

Figure 6-1. Device architecture of the inverted semi-transparent cells and the chemical structures of the active materials PBDTTT-C-T and $PC_{71}BM$ and the interface-modifying molecule C_{60}-SAM.

6.2 Optimization of the Inverted PBDTTT-C-T:$PC_{71}BM$ BHJ Device

The inverted architecture is known to have several advantages over the conventional architecture such as improved stability and compatibility to roll-to-roll processes.[121,291] However, switching device structure between conventional and inverted structure is not always straightforward. The change of charge transport polarity and creation of different interfaces often requires extra optimization efforts.[292,293] Similar situation is observed for the inverted PBDTTT-C-T:$PC_{71}BM$ device with the architecture drawn in **Figure 6-1**. We find that the modification of the ZnO/active layer interface is crucial for otaining the optimal device performance. Devices with no treatment on the interface are found to be significantly less efficient than the conventional device reported by Hou *et al.*;[47] about 20% lower PCE (PCE = 5.7%, J_{sc} = 12.1 mA cm^{-2}) is exhibited as manifested in **Table 6-1**. After modifying the ZnO/active layer interface with self-assembled molecule C_{60}-SAM[294] (**Figure 6-1**), the best inverted device demonstrates much improved performance (PCE of 7.56%, J_{sc} = 15.6 mA cm^{-2}), which becomes

comparable to the conventional device reported by Hou *et al*. Such interfacial modification has been shown to improve the electron extraction.[291,294-296]

Table 6-1. Performance comparison of the inverted PBDTTT-C-T:$PC_{71}BM$ device with and without interface modification to conventional device reported in literature.

Structure	V_{oc} (V)	J_{sc} (mA cm^{-2})	*FF*	PCE (%)
Conventional[a]	0.74	17.48	0.59	7.59
Inverted without C_{60}-SAM modification	0.77[b]	12.13	0.61	5.69
Inverted with C_{60}-SAM modification	0.77	15.64	0.64	7.56

[*a*] Output parameters of conventional PBDTTT-C-T:$PC_{71}BM$ device obtained from reference [47].

[*b*] Numbers represent the data of the best device.

6.3 Fabrication and Characterization of Semi-Transparent Devices

The semi-transparent devices are fabricated by using thin Ag electrode thickness (t_{Ag}) from the most transparent (t_{Ag} = 6) to the least transparent (t_{Ag} = 60 nm). The interfaces between the ZnO and the active layer of all semi-transparent devices are treated with C_{60}-SAM. **Figure 6-2** and **Figure 6-3** show the *J-V* curves and EQE of the inverted semi-transparent devices with different t_{Ag}, respectively. The series resistance (R_s) and the parallel or shunt resistance (R_p) are estimated from the slopes of the *J-V* curves at the points where $V = 0$ and $V = V_{oc}$. The sheet resistance ($R_{\square}$) of thin Ag electrodes is characterized using four-point probe measurements on independent samples of Ag films with the same thicknesses of devices deposited on a 50 nm layer of MoO_3 on glass substrates. Thin Ag films on the MoO_3 substrates have shown $R_{\square}$ comparable to common ITO substrates. A summary of device characteristics can be found in

Table 6-2. PCE of the ST-OPV devices decreases from 7.56% to 4.25 % while t_{Ag} also decreases from 60 nm to 6 nm due to higher absorption loss.

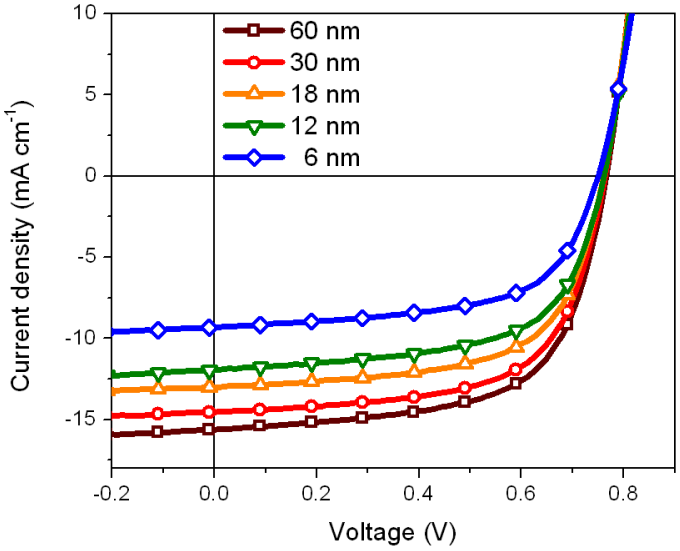

Figure 6-2. *J-V* characteristics of the semitransparent devices with different t_{Ag} under AM1.5G illumination at 100 mW cm^{-2}.

Table 6-2. Characteristics of the semi-transparent PBDTTT-CT:$PC_{71}BM$ solar cells.

Ag thickness (nm)	V_{oc} (V)	J_{sc} (mA cm^{-2})	*FF*	PCE (%)	R_s (Ω cm^2)	R_p (Ω cm^2)	$R_{□}$ (Ω/□)
60	0.77 (0.76)[a]	15.64 (15.09)	0.64 (0.63)	7.56 (7.21)	5.4	540.4	1.1
30	0.76 (0.76)	14.54 (14.37)	0.64 (0.62)	7.05 (6.84)	5.7	766.5	3.4
18	0.76 (0.76)	13.01 (12.99)	0.63 (0.62)	6.22 (6.10)	6.4	740.0	8.3
12	0.76 (0.76)	11.94 (11.75)	0.62 (0.62)	5.62 (5.50)	6.4	547.7	12.3
6	0.75 (0.75)	9.33 (9.25)	0.61 (0.61)	4.25 (4.19)	9.2	668.4	8.8×10^8

[*a*] Numbers in parentheses indicate the average values.

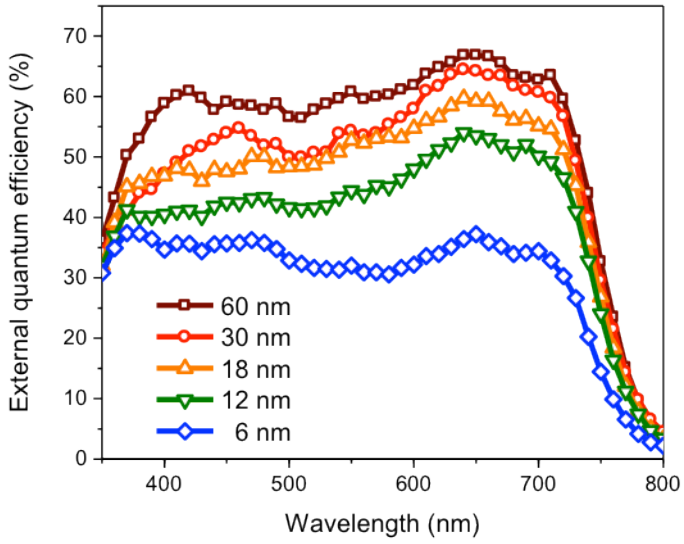

Figure 6-3. EQE of the semi-transparent devices with t_{Ag} varied from 6 nm to 60 nm.

6.4 Optical Properties of The ST-OPV Devices

The semitransparent solar cells exhibit a grayish or color neutral appearance due to the complementary and balanced absorption from the PBDTTT-C-T polymer and $PC_{71}BM$ over the visible spectrum. **Figure 6-4a** demonstrates the transmission spectra of the solar cells with varying Ag thickness (open symbols) obtained via UV-Vis-NIR spectroscopy. The transmission curve of a sample without Ag electrode (t_{Ag} = 0 nm) is also measured for comparison. The average visible transmittance (AVT), or the average of the transmittance of the solar cells in the visible region (370 nm – 740 nm), of the ST-OPV devices are calculated and presented in **Table 6-2**. As the thickness of the reflective Ag electrode varies from 6 nm to 60 nm, the AVT are reduced accordingly from ~35.9% to ~2.0%, showing the ease of transparency management through the electrode thickness control. Though the transparency requirement of the windows depends on the working environments, it is generally considered that AVT of 25% is the benchmark[297] for window application.

The performance of the solar cells are plotted against the AVT and displayed in **Figure 6-5**. It can be observed that the AVT and the device performance oppose each other almost linearly, which clearly shows the tradeoff between the transparency and photon collection. The performance of some representative ST-OPV devices[131,289,290,298] reported earlier is also displayed in **Figure 6-5** for comparison. Note the ST-OPV devices based on PBDTTT-C-T:$PC_{71}BM$ show significantly improved performance compared to other ST-OPV devices with similar transparencies. Furthermore, the devices with t_{Ag} = 12 and 18 nm are particularly attractive among the data points since they have presented very practical AVT between 21% to 28% with excellent PCE of 6.2% to 5.6 %.

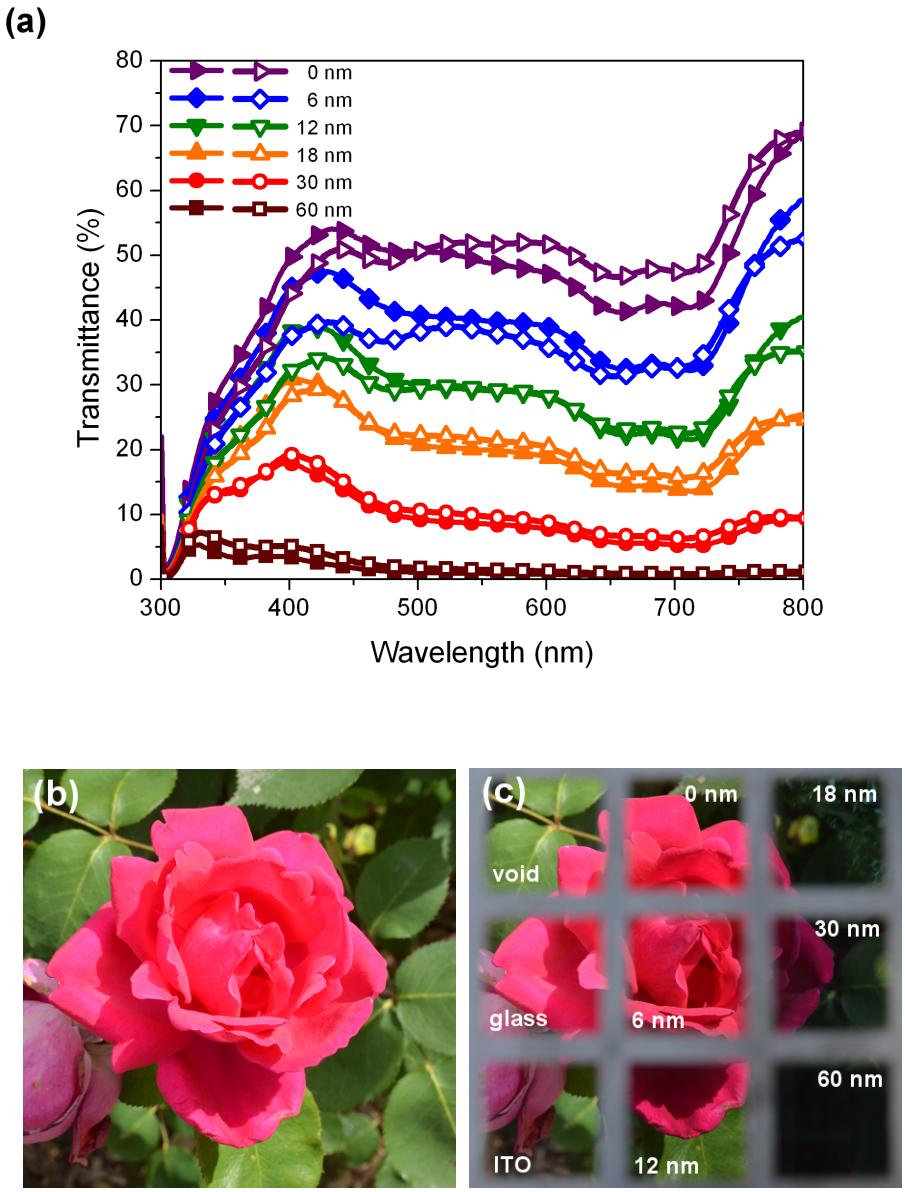

Figure 6-4. (a) Transmission spectrum of the ST-OPV devices from optical modeling (close symbols) and the real devices (open symbols). (b and c) Photographs of a pink rose taken with exactly the same camera settings (shutter, aperture, white balance, etc.) in a sunny day. Photograph (c) was taken through the ST-OPV devices with the six different Ag thicknesses and blank ITO and glass substrates.

Table 6-3. Optical properties of the semi-transparent devices with different transparencies.

Ag thickness (nm)	AVT (%)	HPT (%)	CIE 1931 (x,y)	CCT (K)	|Δuv|	General CRI
60	2.0	1.4	(0.2650, 0.2617)	15894	3.90×10^{-3}	94.8
30	10.6	9.5	(0.2917, 0.3010)	8390	3.98×10^{-5}	96.7
18	21.3	21.1	(0.3091, 0.3227)	6764	1.76×10^{-3}	97.3
12	27.9	28.9	(0.3187, 0.3351)	6156	3.34×10^{-3}	96.8
6	35.9	37.3	(0.3225, 0.3442)	5943	6.11×10^{-3}	96.3
0	48.7	51.3	(0.3323, 0.3478)	5507	3.44×10^{-3}	98.0

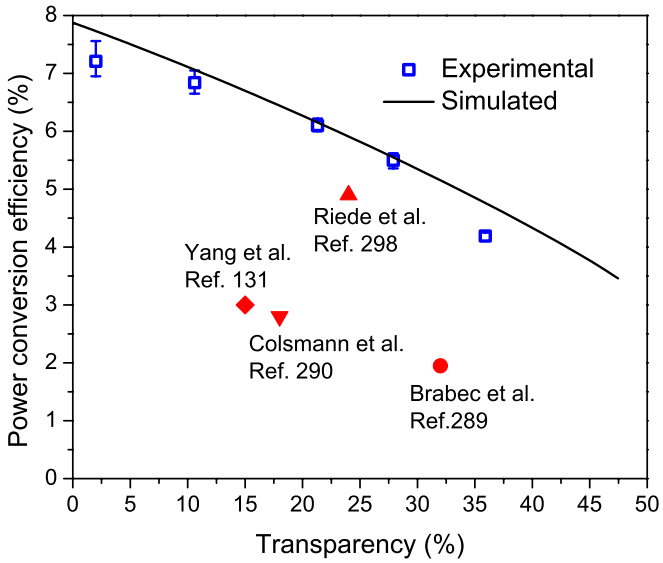

Figure 6-5. Dependence of PCE of the ST-OPV devices to their respective transparency. Representative ST-OPV devices reported in literature are also displayed for comparison.

6.5 Optical Perception Corrected by Response of Human Eye

The visual appearances of the ST-OPV cells perceived by the human eye are also the key properties in determining their functionalities and applications. Due to the spectrally dependent response of the human eyes, the human perception of color and transparency may vary from the

experimental values acquired from machine. For example, the human perception of transmittance (HPT) of ST-OPV cell based on P3HT:$PC_{71}BM$ is distinctly lower than its AVT[289] due to the low responsivity to red light of human eyes. Therefore, we analyze the effect of the response of the human eye by calibrating the transmission spectra of the ST-OPV devices with the human eye sensitivity (y color-matching function) following the procedure reported by Ameri *et al.*[289] The analysis shows small differences between the HPT and AVT of our ST-OPV devices as summarized in **Table 6-3**, which can be attributed to the rather balanced absorption of the PBDTTT-C-T:$PC_{71}BM$ blend over the visible range as revealed in the transmission spectra. The transmission spectra and the small difference between the AVT and HPT suggest the ST-OPV cells are acting similarly to neutral density filters, which is ideal for the windows applications.

The transparency color perceptions of the ST-OPV devices are depicted using the CIE 1931 chromaticity diagram (xyY), which is specifically designed to represent the colors perceptible by the human eye. The transmitted light is represented by the product of the AM1.5G solar spectrum and the transmission spectrum of each semi-transparent device, and the corresponding color coordinates CIE 1931 (x,y) are summarized in **Table 6-3**. The representations of the color coordinates of the ST-OPV devices are also displayed on the CIE 1931 chromaticity diagram in **Figure 6-6**. The color coordinates of the ST-OPV devices with thin Ag electrodes ($t_{Ag} \leq 30$ nm) are located in the low colorfulness area in the CIE chromaticity diagram, indicating good achromatic or neutral color sensations when looking through the devices under AM1.5G illumination. The transmitted light of the device with $t_{Ag} = 12$ nm and $t_{Ag} = 18$ nm show the color coordinates particularly close to the standard daylight illuminant D65 (x_{D65},y_{D65}) = (0.3128, 0.3290) at (x_{Ag12}, y_{Ag12}) = (0.3187, 0.3351) and (x_{Ag18}, y_{Ag18}) = (0.3091, 0.3227), respectively, capable of providing extremely high quality illumination with achromatic sensation. The color

coordinates move in the direction toward the blue corner of the CIE chromaticity diagram as the Ag electrode gets thicker, but overall the color coordinates of the ST-OPV cells suggest transparency color perceptions of neutral colors from the transmitted light with very little color bias caused by the PBDTTT-C-T:$PC_{71}BM$ based STOPV cells.

6.6 Color Rendering Capacity

The human visual system is capable to correct for color deviations caused by varying illumination conditions. This ability is known as color constancy.[299] Experimentally has been determined that the different chromaticities associated to the phases of daylight are close to that of blackbody radiators in the range 4000 to 25000 K.[300] Because the color constancy of our vision system under daylight illumination is known to be excellent, blackbody radiators are often referred in colorimetry as light sources of perfect color rendering capacities. We have demonstrated the transmitted lights of ST-OPV devices under AM1.5G illumination are good metamers, or dissimilar spectral distributions that produce the same color sensation, to nearly white light illuminants. However, white light illuminants do not necessarily provide good color rendering capacities. Therefore, we further evaluate the color rendering indices (CRIs) of the transmitted light of the STOPV cells.

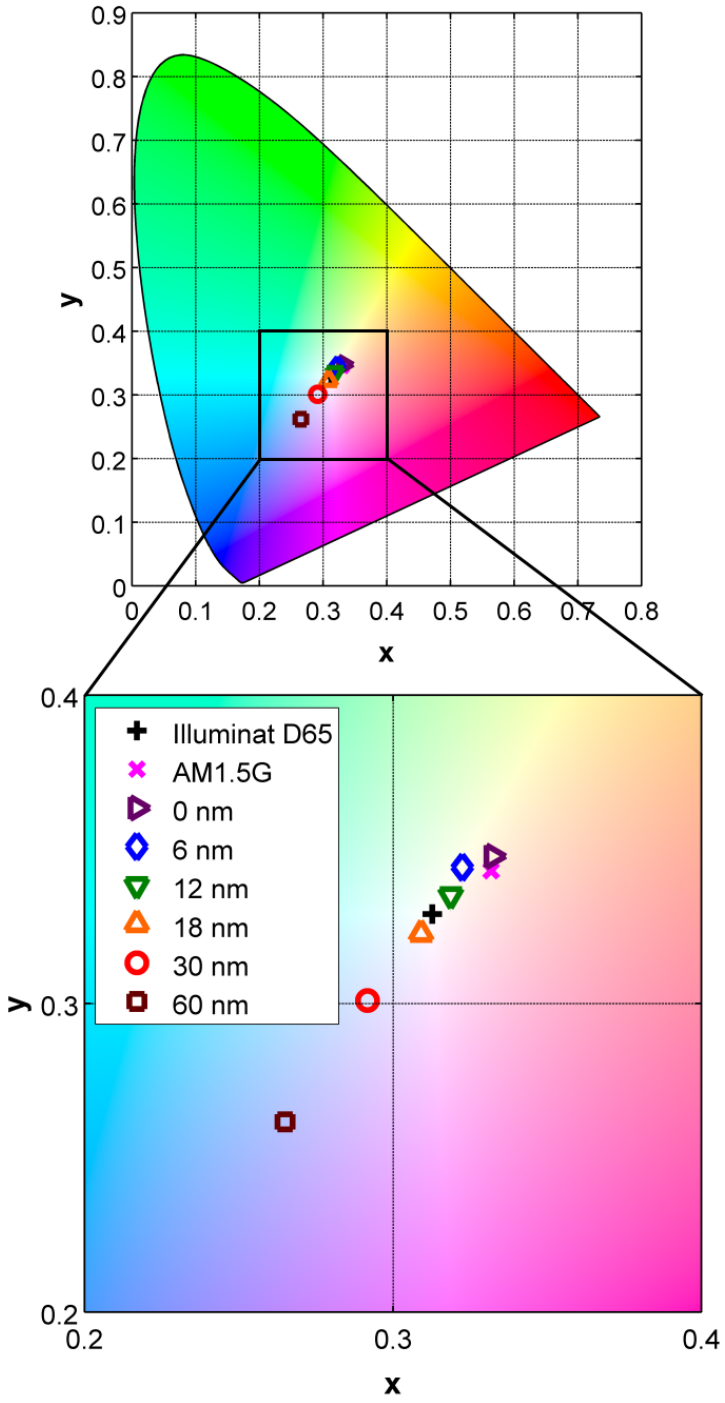

Figure 6-5. The representation of color coordinate of the STOPV devices with different thickness of Ag electrode under AM1.5G illumination on the CIE chromaticity diagram xyY (1931) and the enlarged image. The color coordinate representation of D65 standard daylight illuminant and AM1.5G illumination are also presented.

The trace of the blackbody emission as the function of temperature in a particular color space is known as the Planckian locus or the blackbody locus. When the color coordinate of a light source is considered in the CIE 1960 UCS (uniform color space), the correlated color temperature (CCT) of the light source is defined as the color temperature of the nearest point on the Planckian locus. Note that the CCT is considered meaningful only if the distance between the color coordinate of the light source and the Planckian locus is within ±0.05 as recommended by CIE. The CIE 1931 (x,y) coordinates of the devices are transformed to the UCS CIE 1960 (u, v) color space displayed in **Figure 6-7.** The CCTs of the points and their corresponding distances to the Planckian locus (Δ_{uv}) are calculated from the UCS coordinates and summarized in **Table 6-3**. Notably, all points are very close to the Planckian locus with $|\Delta_{uv}|$ all less than 0.05, suggesting the transmitted light of all devices are all still close to blackbody radiators.

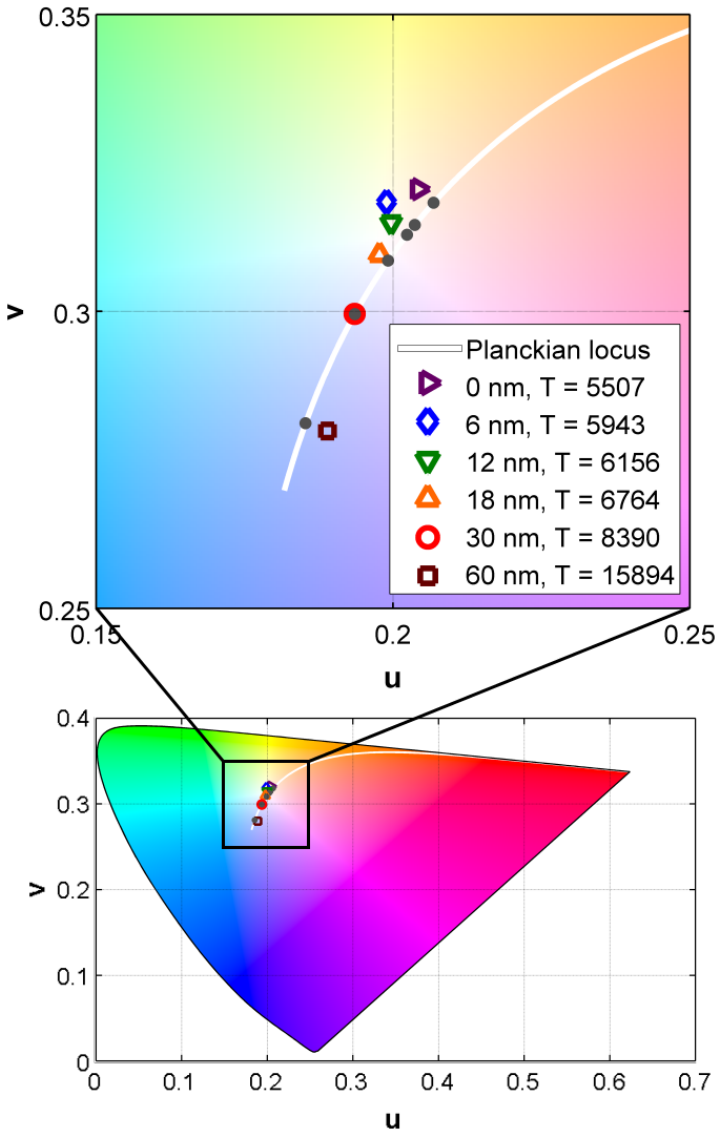

Figure 6-6. Planckian locus and the UCS coordinates CIE 1960 (u, v) of the STOPV devices. The gray dots represent the nearest Planckian radiators.

The color rendering capacities are analyzed by using the test sample method (TSM).[290] The method compares the color associated in the UCS color space to 8 standard color samples (TCS01-08) evenly distributed over the complete range of hues when they are illuminated by a probing light, which denotes the AM1.5G spectrum folded with the transmission spectrum of any of the ST-OPV cells in this case, and a reference white light source with the same color

temperature to the probing light. The choice of the reference white light source depends on the CCT. In the cases of CCT > 5000 K, a CIE standard illuminant D with she same CCT is used as the reference.

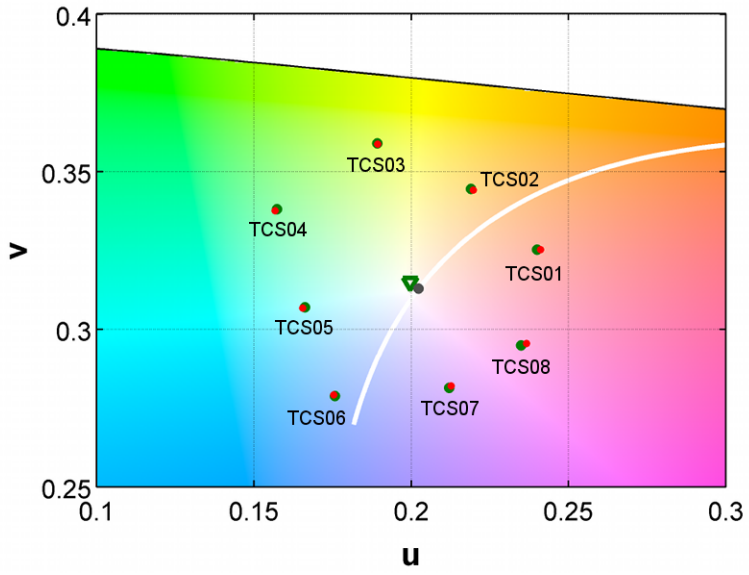

Figure 6-7. Determination of the color rendering index of the ST-OPV device with 12 nm Ag electrode. The central green triangle represents the transmitted light of the PBDTTT-C-T:$PC_{71}BM$ STOPV cell under AM1.5G illumination. The surrounding green dots correspond to the TCS01–08 illuminated by the transmitted light of the ST-OPV cell under AM1.5G illumination. The red dots represent the TCS01–08 illuminated by the reference Standard Illuminant D of CCT = 6156 K.

By multiplying the spectra of the color samples with the reference or with the probing light spectra, we obtain the reflection spectra of the samples, which are further used to calculate their color coordinates in the CIEUVW space and the special CRIs. The mean of the special CRIs is called the general CRI, which represents the color rendering capacity of the sample. By definition, the special and the general CRI can range from 0 to 100, where a higher general CRI

represents a better color rendering capacity. The general CRIs of the transmitted light of all STOPV devices are listed in **Table 6-3**, and the special CRIs are shown in **Table 6-4**. The CRIs of all our functional devices are close to 100. To the best of our knowledge, these are the highest general CRI values ever reported for ST-OPV cells. The UCS points of a representative STOPV device (t_{Ag} = 12nm), the nearest Planckian locus point, and the color samples under both the tested and the reference illumination are plotted in **Figure 6-8**. As implied by the excellent general CRIs, the color point corresponding to the ST-OPV cell is almost superimposed with the nearest point on the Planckian locus. Similarly, the corresponding sample color points under both kinds of illuminations are nearly superimposed, clearly demonstrating the exceptional color rendering properties of this system.

Table 6-4. Special color rendering indices (CRIs) of the transmitted light of the STOPV devices under AM1.5G illumination.

	0 nm	6 nm	12 nm	18 nm	30 nm	60 nm
Special CRI - TCS01	97.7	95.0	96.3	97.5	97.9	97.6
Special CRI - TCS02	98.7	96.9	97.6	97.8	96.8	94.8
Special CRI - TCS03	99.5	99.3	98.9	98.3	96.0	91.2
Special CRI - TCS04	98.2	96.1	97.1	97.7	96.6	93.0
Special CRI - TCS05	98.1	95.6	96.9	98.0	98.4	98.2
Special CRI - TCS06	98.8	96.6	97.5	97.6	96.5	94.5
Special CRI - TCS07	98.1	97.8	97.2	97.2	96.2	93.7
Special CRI - TCS08	95.1	92.8	93.1	94.6	95.5	95.6

6.7 Optical Simulations

In order to investigate and exploit the full potential of this system, particularly concerning the limitation of transparency imposed on the highest achievable efficiency, optical simulations based on the transfer matrix method (TMM) were performed. The optical model comprises 120 nm of ITO, following by 33 nm of sol–gel ZnO, 90 nm of the PBDTTT-C-T:$PC_{71}BM$ (1 : 1.5 w/w) active layer, 5 nm of MoO_3, and finally a Ag

layer with variable thickness. Each component is represented by its complex refractive index acquired by variable angle spectroscopic ellipsometry (VASE). The simulations are based on assumptions of planar interfaces and total isotropy for all layers.

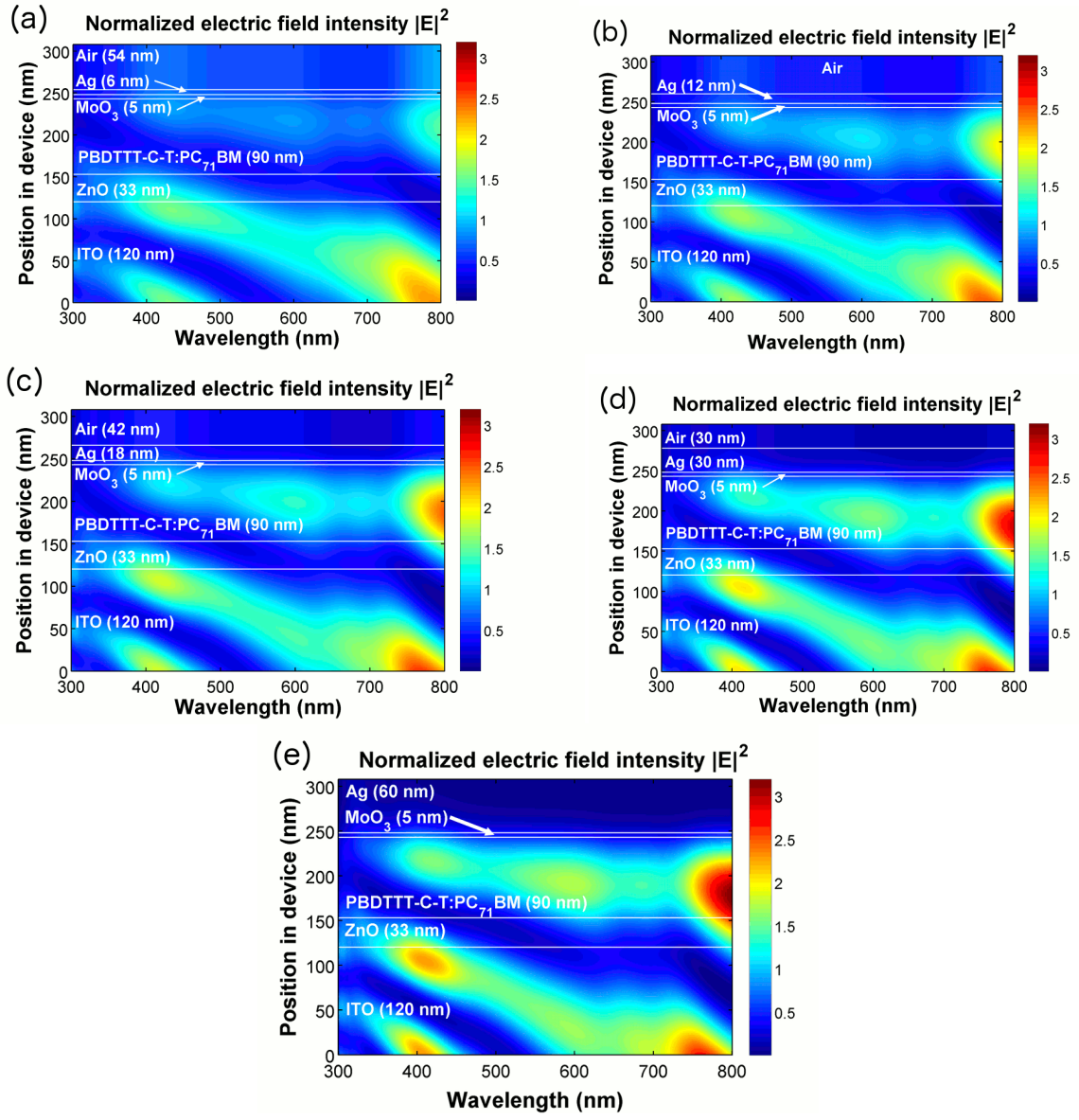

Figure 6-8. Simulations for the electric field intensity profile $|E|^2$ in the studied STOPV devices with (a) 6 nm, (b) 12nm, (c) 18 nm, (d) 30 nm, and (e) 60 nm of Ag electrode.

A constant energy radiator, i.e. illuminant with normalized incident amplitude at all wavelengths, is first applied to the optical model to obtain the electric field distribution inside the solar cells. The electric field intensity profiles of the ST-OPV cells can be visualized in **Figure 6-9**. The simulations indicate that the distributions of the electric field inside the solar cells are highly wavelength dependent and inhomogeneous as a result of the interference effect. Higher intensity of electric field distributed in the device with thicker Ag electrode is observed as expected due to less transmitted photon loss. From the electric field distributions, simulated transmission curves of the ST-OPV cells are derived and compared with the experimental curves in **Figure 6-4**. We note that the simulated curves are in exceptionally good agreements with the experimental curves, indicating the validity of our model.

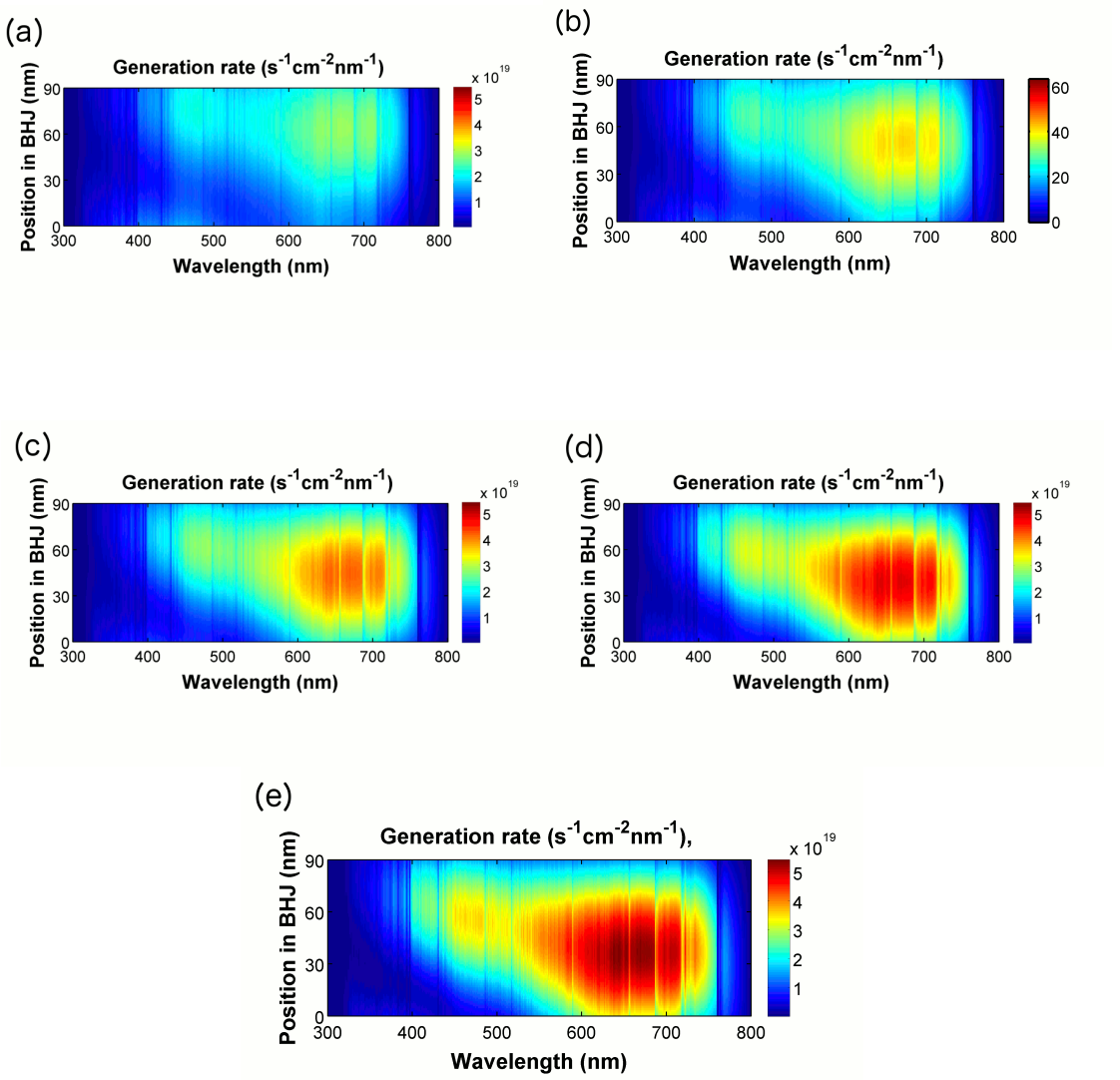

Figure 6-9. Simulations of exciton generation rate in the studied STOPV devices with (a) 6 nm, (b) 12nm, (c) 18 nm, (d) 30 nm, and (e) 60 nm of Ag electrode.

Generation of excitons in the active layer is also described as the product of the modulus squared of the electric field obtained from TMM, the AM1.5G spectrum, the real part of the refractive index (η), and the absorption coefficient (α), which is associated to the imaginary part (κ) of the refractive index by $\alpha = 4\pi\kappa/\lambda$ and the factor $c\varepsilon_0/2$, where c is the speed of light in vacuum and ε_0 the permittivity of free space. The expressions of

the exciton generation rate of the ST-OPV devices are presented in **Fig. 6-10**. It can be observed that the excitons are generated efficiently over the visible regime, which explains the effectiveness of photocurrent generation from the PBDTTT-C-T:$PC_{71}BM$ system.

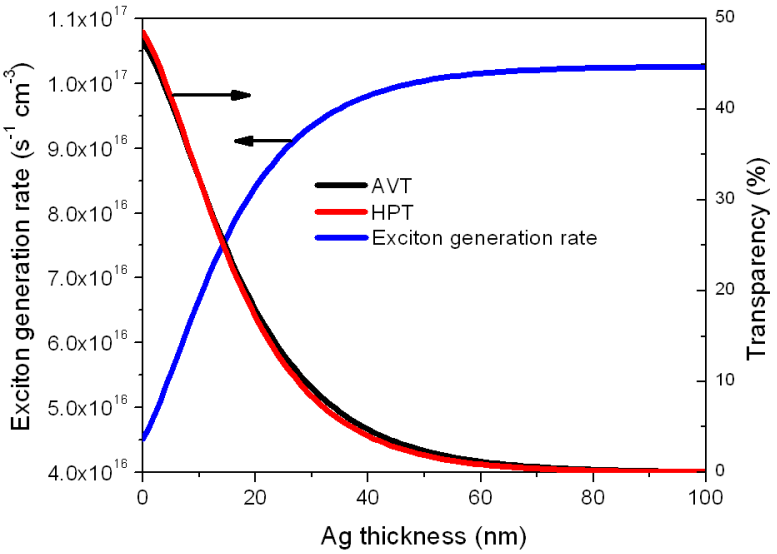

Figure 6-10. Dependence of the exciton generation rate to the thickness of the Ag electrode from the optical model. The dependence of the average visible-light transmittance (AVT, black curve) and human perception of transmittance (HPT, red curve) of devices simulated from the optical model at various Ag thicknesses are also revealed.

By integrating the distributed exciton generation rate over the whole active layer, we also obtain the accumulated exciton generation rate, or the total number of absorbed photons (N_{ph}), in the solar cells. **Figure 6-11** plots the N_{ph} against continuous change of the t_{Ag} (0 nm – 100 nm). The trend indicates that N_{ph} is fairly sensitive to the change of t_{Ag} when t_{Ag} is small. N_{ph} starts with a close to linear increment as Ag begins to build up,

doubles at t_{Ag} ~25 nm, and finally gets to a plateau when t_{Ag} > 65 nm. The monotonic and evident enhancement of the N_{ph} upon the application of reflective electrode in the PBDTTT-C-T:$PC_{71}BM$ inverted cell explains the effectiveness of tuning the transparency through the thickness control of the metal electrode. Interestingly, the observation is very different to the simulation of semitransparent inverted P3HT:$PC_{71}BM$ device performed by Ameri *et al.*, where applying a 100 nm opaque reflective electrode to the device only results in relatively mild enhancement on N_{ph}. We attribute the difference between the two systems to the optical effect of the hole-transport layer. By replacing the 5 nm MoO_3 in the optical model with 100 nm PEDOT:PSS as used in the P3HT:$PC_{71}BM$ inverted solar cell, we observe that the difference of N_{ph} of devices with and without 100 nm Ag electrode becomes insignificant (data not shown). Figure 5.11 also shows the simulations of AVT and HPT at various Ag thicknesses. Again, the figure reveals the HPT is almost identical to AVT at every Ag thickness.

From the simulation of N_{ph}, we can also estimate the relation between the highest achievable PCE with transparency by assuming constant IQE of 100% at every wavelength, V_{oc} = 0.76, and FF = 0.63. The calculation establishes a near linear relationship between the highest achievable PCE and the AVT (**Figure 6-5**), which fits the experimental data even with good quantitative accuracy. The relation makes it possible to build devices with predictable performance and transparency. The success of optical simulations in portraying the optical behaviors of the PBDTTT-C-T:$PC_{71}BM$ system proposes their usefulness in designing or engineering future ST-OPV systems.

6.8 CONCLUSION

In conclusion, we have demonstrated high efficiency ST-OPV cells with significantly improved, state-of-the-art performance compared to other ST-OPV devices with similar transparency. The ST-OPV devices under the AM1.5G illumination provide close to white or achromatic transparency color perceptions, especially for the devices with thin Ag electrodes ($t_{Ag} \leq 30$ nm). The transmitted light further demonstrates extraordinary transparency color rendering capacities with the highest CRIs (> 96) ever reported for ST-OPV devices. This combination of advantages suggest that inverted ST-OPV devices based on PBDTTT-C-T:$PC_{71}BM$ mixtures can provide high quality transmitted light that is suitable for window applications. We also built an optical model that portrays the optical behaviors of the ST-OPV systems accurately.

6.9 EXPERIMENTAL SECTION

6.9.1 *Materials*

PBDTTT-C-T is synthesized according to the procedure reported elsewhere.[47] PBDTTT-C-T (10 mg ml^{-1}) and $PC_{71}BM$ (American Dye Source, 15 mg ml^{-1}) were dissolved in 1,2-dichlorobenzene with 3 vol% of 1,8-diiodooctaneas the processing additive. 1,2-dichlorobenzene (Aldrich) and 1,8-diiodooctane (Aldrich) were used without further purification. The PBDTTT-C-T:$PC_{71}BM$ blend solution was heated for homogenous mixing but was cooled and filtered with 0.45 μm PTFE filter before use. The ZnO precursor was prepared following the procedure reported by Sun *et al.*[301] Zinc acetate dihydrate (Aldrich, 99.9%, 1 g) is dissolved in and ethanolamine (Aldrich, 99.5%, 0.28 g) are dissolved in 2-methoxyethanol (Aldrich, 99.8%, 10 mL) under vigorous

stirring for a least 12 h and filtered (0.45 μm PTFE) before use. Synthesis of the C_{60}-SAM molecule is described in previous report.[294]

6.9.2 *Device Fabrication and Characterizations*

ITO-coated glass substrates were cleaned sequentially by sonication in detergent, de-ionized water, acetone, and isopropyl alcohol, and dried in a nitrogen stream, followed by 30 s of oxygen plasma treatment. The deposition of each layer is described as followed. ZnO precursor solution was first spin-coated on the ITO-coated glass substrates to deposit a thin ZnO layer (ca. 33 nm) and baked at 200°C for 1 h under ambient condition. The substrates were then transferred into a nitrogen-filled glovebox for the following processing. C_{60}-SAM molecules were dissolved in chlorobenzene (Aldrich, 50 vol%) and tetrahydrofuran (THF, Aldrich, 50 vol%) co-solvent at the concentration of 1 wt%. The self-assembly of the C_{60}-SAM was performed by spin-coating of the C_{60}-SAM solution on top of the ZnO surface. The substrates were washed with THF to remove unbound C_{60}-SAM molecules. Subsequently, the PBDTTT-C-T:$PC_{71}BM$ active layer (ca. 90 nm) was spin-coated on the ZnO layer from filtered solution. No further post-treatments such as thermal annealing were performed on the devices. The substrates pumped down to high vacuum ($< 2\times10^{-6}$ Torr) in the evaporator chamber, and then MoO_3 (5 nm) and silver (6 nm - 60 nm) were sequentially evaporated onto the active layer through shadow masks to define the device area of 10.08 mm^2.

The current density-voltage (*J-V*) characteristics of photovoltaic devices were measured in an inert environment using a Keithley 2400 source-measurement unit under simulated AM 1.5 global illumination from an 300 Watt Solar Light solar simulator. A Hamamatsu silicon solar cell with a KG5 color filter, which is traced to the National

Renewable Energy Laboratory (NREL), was used as the reference cell to calibrate the light intensity to 1 sun (100 mW/cm^2). The spectral external quantum efficiency was recorded under chopped illumination in ambient atmosphere. The photocurrent was recorded with a lock-in-amplifier (Stanford Research Systems SR830).

BIBLIOGRAPHY

[1] *International Energy Outlook 2011*, U.S. Energy Information Administration, **2011**.
[2] P. Perez, M. Perez, *A fundamental look at energy reserves for the planet*, Vol. 50, The IEA SHC Solar Update, **2009** 2.
[3] M. A. Green, K. Emery, Y. Hishikawa, W. Warta, E. D. Dunlop, "Solar cell efficiency tables (version 43)" *Prog. Photovoltaics Res. Appl.* **2014**, *22*, 1.
[4] T. Ameri, N. Li, C. J. Brabec, "Highly efficient organic tandem solar cells: a follow up review" *Energy Environ. Sci.* **2013**, *6*, 2390.
[5] R. Liu, "Hybrid Organic/inorganic nanocomposites for photovoltaic cells" *Materials* **2014**, *7*, 2747.
[6] C. W. Tang, "Two-layer organic photovoltaic cell" *Appl. Phys. Lett.* **1986**, *48*, 183.
[7] G. Yu, J. Gao, J. C. Hummelen, F. Wudl, A. J. Heeger, "Polymer photovoltaic cells: enhanced efficiencies via a network of internal donor-acceptor heterojunctions" *Science* **1995**, *270*, 1789.
[8] J. J. M. Halls, C. A. Walsh, N. C. Greenham, E. A. Marseglia, R. H. Friend, S. C. Moratti, A. B. Holmes, "Efficient photodiodes from interpenetrating polymer networks" *Nature* **1995**, *376*, 498.
[9] C. R. McNeill, A. Abrusci, J. Zaumseil, R. Wilson, M. J. McKiernan, J. H. Burroughes, J. J. M. Halls, N. C. Greenham, R. H. Friend, "Dual electron donor/electron acceptor character of a conjugated polymer in efficient photovoltaic diodes" *Appl. Phys. Lett.* **2007**, *90*, 193506.
[10] J. T. Bloking, X. Han, A. T. Higgs, J. P. Kastrop, L. Pandey, J. E. Norton, C. Risko, C. E. Chen, J.-l. Bre, M. D. McGehee, A. Sellinger, "Solution-processed organic solar cells with power conversion efficiencies of 2.5% using benzothiadiazole/imide-based acceptors" *Chem. Mater.* **2011**, *23*, 5484.
[11] P. E. Schwenn, K. Gui, A. M. Nardes, K. B. Krueger, K. H. Lee, K. Mutkins, H. Rubinstein-Dunlop, P. E. Shaw, N. Kopidakis, P. L. Burn, P. Meredith, "A small molecule non-fullerene electron acceptor for organic solar cells" *Adv. Energy Mater.* **2011**, *1*, 73.
[12] P. Sonar, J. P. Fong Lim, K. L. Chan, "Organic non-fullerene acceptors for organic photovoltaics" *Energy Environ. Sci.* **2011**, *4*, 1558.
[13] J. E. Anthony, "Small-molecule, nonfullerene acceptors for polymer bulk heterojunction organic photovoltaics" *Chem. Mater.* **2011**, *23*, 583.
[14] Y. He, Y. Li, "Fullerene derivative acceptors for high performance polymer solar cells" *Phys. Chem. Chem. Phys.* **2011**, *13*, 1970.
[15] Y. Fang, A. K. Pandey, A. M. Nardes, N. Kopidakis, P. L. Burn, P. Meredith, "A narrow optical gap small molecule acceptor for organic solar cells" *Adv. Energy Mater.* **2013**, *3*, 54.
[16] T. Earmme, Y.-J. Hwang, N. M. Murari, S. Subramaniyan, S. A. Jenekhe, "All-polymer solar cells with 3.3% efficiency based on naphthalene diimide-selenophene copolymer acceptor" *J. Am. Chem. Soc.* **2013**, *135*, 14960.
[17] A. Facchetti, "Polymer donor–polymer acceptor (all-polymer) solar cells" *Mater. Today* **2013**, *16*, 123.

[18] N. S. Sariciftci, L. Smilowitz, A. J. Heeger, F. Wudl, "Photoinduced electron transfer from a conducting polymer to buckminsterfullerene" *Science* **1992**, *258*, 1474.
[19] R. Koeppe, D. Hoeglinger, P. A. Troshin, R. N. Lyubovskaya, V. F. Razumov, N. S. Sariciftci, "Organic solar cells with semitransparent metal back contacts for power window applications" *ChemSusChem* **2009**, *2*, 309.
[20] M. Lenes, G.-J. A. H. Wetzelaer, F. B. Kooistra, S. C. Veenstra, J. C. Hummelen, P. W. M. Blom, "Fullerene bisadducts for enhanced open-circuit voltages and efficiencies in polymer solar cells" *Adv. Mater.* **2008**, *20*, 2116.
[21] Y. He, H.-Y. Chen, J. Hou, Y. Li, "Indene−C60 bisadduct: a new acceptor for high-performance polymer solar cells" *J. Am. Chem. Soc.* **2010**, *132*, 1377.
[22] Y. He, G. Zhao, B. Peng, Y. Li, "High-yield synthesis and electrochemical and photovoltaic properties of indene-C70 bisadduct" *Adv. Funct. Mater.* **2010**, *20*, 3383.
[23] P. P. Khlyabich, B. Burkhart, B. C. Thompson, "Efficient ternary blend bulk heterojunction solar cells with tunable open-circuit voltage" *J. Am. Chem. Soc.* **2011**, *133*, 14534.
[24] Y. Zou, A. Najari, P. Berrouard, S. Beaupré, B. R. Aïch, Y. Tao, M. Leclerc, "A thieno[3,4-c]pyrrole-4,6-dione-based copolymer for efficient solar cells" *J. Am. Chem. Soc.* **2010**, *132*, 5330.
[25] Y. Lin, Y. Li, X. Zhan, "Small molecule semiconductors for high-efficiency organic photovoltaics" *Chem. Soc. Rev.* **2012**, *41*, 4245.
[26] A. Mishra, P. Bäuerle, "Small molecule organic semiconductors on the move: promises for future solar energy technology" *Angew. Chem. Int. Ed.* **2012**, *51*, 2020.
[27] R. Kroon, M. Lenes, J. C. Hummelen, P. W. M. Blom, B. de Boer, "Small bandgap polymers for organic solar cells (polymer material development in the last 5 years)" *Polym. Rev.* **2008**, *48*, 531.
[28] Y. J. Cheng, S. H. Yang, C. S. Hsu, "Synthesis of conjugated polymers for organic solar cell applications" *Chem. Rev.* **2009**, *109*, 5868.
[29] H.-J. Jhuo, P.-N. Yeh, S.-H. Liao, Y.-L. Li, Y.-S. Cheng, S.-A. Chen, "Review on the recent progress in low band gap conjugated polymers for bulk hetero-junction polymer solar cells" *J. Chin. Chem. Soc.* **2014**, *61*, 115.
[30] R. S. Kularatne, H. D. Magurudeniya, P. Sista, M. C. Biewer, M. C. Stefan, "Donor-acceptor semiconducting polymers for organic solar cells" *J. Polym. Sci., Part A: Polym. Chem.* **2013**, *51*, 743.
[31] S. E. Shaheen, C. J. Brabec, N. S. Sariciftci, F. Padinger, T. Fromherz, J. C. Hummelen, "2.5% efficient organic plastic solar cells" *Appl. Phys. Lett.* **2001**, *78*, 841.
[32] C. J. Brabec, S. E. Shaheen, C. Winder, N. S. Sariciftci, P. Denk, "Effect of LiF/metal electrodes on the performance of plastic solar cells" *Appl. Phys. Lett.* **2002**, *80*, 1288.
[33] C. Melzer, E. J. Koop, V. D. Mihailetchi, P. W. M. Blom, "Hole transport in poly(phenylene vinylene)/methanofullerene bulk-heterojunction solar cells" *Adv. Funct. Mater.* **2004**, *14*, 865.
[34] V. D. Mihailetchi, L. J. a. Koster, P. W. M. Blom, C. Melzer, B. de Boer, J. K. J. van Duren, R. A. J. Janssen, "Compositional dependence of the performance of poly(p-phenylene vinylene):methanofullerene bulk-heterojunction solar cells" *Adv. Funct. Mater.* **2005**, *15*, 795.

[35] M. M. Wienk, J. M. Kroon, W. J. H. Verhees, J. Knol, J. C. Hummelen, P. A. van Hal, R. A. J. Janssen, "Efficient methano[70]fullerene/MDMO-PPV bulk heterojunction photovoltaic cells" *Angew. Chem.* **2003**, *115*, 3493.
[36] M. T. Dang, L. Hirsch, G. Wantz, "P3HT:PCBM, best seller in polymer photovoltaic research" *Adv. Mater.* **2011**, *23*, 3597.
[37] D. Chirvase, Z. Chiguvare, M. Knipper, J. Parisi, V. Dyakonov, J. C. Hummelen, "Temperature dependent characteristics of poly(3 hexylthiophene)-fullerene based heterojunction organic solar cells" *J. Appl. Phys.* **2003**, *93*, 3376.
[38] H. Hoppe, N. S. Sariciftci, "Morphology of polymer/fullerene bulk heterojunction solar cells" *J. Mater. Chem.* **2006**, *16*, 45.
[39] G. Li, V. Shrotriya, Y. Yao, J. Huang, Y. Yang, "Manipulating regioregular poly(3-hexylthiophene) : [6,6]-phenyl-C61-butyric acid methyl ester blends—route towards high efficiency polymer solar cells" *J. Mater. Chem.* **2007**, *17*, 3126.
[40] S. H. Park, A. Roy, S. Beaupré, S. Cho, N. Coates, J. S. Moon, D. Moses, M. Leclerc, K. Lee, A. J. Heeger, "Bulk heterojunction solar cells with internal quantum efficiency approaching 100%" *Nat. Photonics* **2009**, *3*, 297.
[41] J. Peet, J. Y. Kim, N. E. Coates, W. L. Ma, D. Moses, A. J. Heeger, G. C. Bazan, "Efficiency enhancement in low-bandgap polymer solar cells by processing with alkane dithiols" *Nat. Mater.* **2007**, *6*, 497.
[42] M. Morana, M. Wegscheider, A. Bonanni, N. Kopidakis, S. Shaheen, M. Scharber, Z. Zhu, D. Waller, R. Gaudiana, C. J. Brabec, "Bipolar charge transport in PCPDTBT-PCBM bulk-heterojunctions for photovoltaic applications" *Adv. Funct. Mater.* **2008**, *18*, 1757.
[43] J. Hou, H. Y. Chen, S. Zhang, G. Li, Y. Yang, "Synthesis, characterization, and photovoltaic properties of a low band gap polymer based on silole-containing polythiophenes and 2,1,3-benzothiadiazole" *J. Am. Chem. Soc.* **2008**, *130*, 16144.
[44] Y. Liang, Z. Xu, J. Xia, S. T. Tsai, Y. Wu, G. Li, C. Ray, L. Yu, "For the bright future-bulk heterojunction polymer solar cells with power conversion efficiency of 7.4%" *Adv. Mater.* **2010**, *22*, E135.
[45] Y. Liang, L. Yu, "A new class of semiconducting polymers for bulk heterojunction solar cells with exceptionally high performance" *Acc. Chem. Res.* **2010**, *43*, 1227.
[46] M. Wang, X. Hu, P. Liu, W. Li, X. Gong, F. Huang, Y. Cao, "Donor-acceptor conjugated polymer based on naphtho[1,2-c:5,6-c]bis[1,2,5]thiadiazole for high-performance polymer solar cells" *J. Am. Chem. Soc.* **2011**, *133*, 9638.
[47] L. Huo, S. Zhang, X. Guo, F. Xu, Y. Li, J. Hou, "Replacing alkoxy groups with alkylthienyl groups: a feasible approach to improve the properties of photovoltaic polymers" *Angew. Chem. Int. Ed. Engl.* **2011**, *50*, 9697.
[48] Z. He, C. Zhong, S. Su, M. Xu, H. Wu, Y. Cao, "Enhanced power-conversion efficiency in polymer solar cells using an inverted device structure" *Nat. Photonics* **2012**, 1.
[49] S. Günes, H. Neugebauer, N. S. Sariciftci, "Conjugated polymer-based organic solar cells" *Chem. Rev.* **2007**, *107*, 1324.
[50] J. Peet, M. L. Senatore, A. J. Heeger, G. C. Bazan, "The role of processing in the fabrication and optimization of plastic solar cells" *Adv. Mater.* **2009**, *21*, 1521.

[51] B. C. Thompson, J. M. J. Fréchet, "Polymer-fullerene composite solar cells" *Angew. Chem. Int. Ed.* **2008**, *47*, 58.
[52] G. Li, V. Shrotriya, J. Huang, Y. Yao, T. Moriarty, K. Emery, Y. Yang, "High-efficiency solution processable polymer photovoltaic cells by self-organization of polymer blends" *Nat. Mater.* **2005**, *4*, 864.
[53] X. Yang, A. Uddin, "Effect of thermal annealing on P3HT:PCBM bulk-heterojunction organic solar cells: a critical review" *Renew. Sustain. Energ. Rev.* **2014**, *30*, 324.
[54] W. Ma, C. Yang, X. Gong, K. Lee, A. J. Heeger, "Thermally stable, efficient polymer solar cells with nanoscale control of the interpenetrating network morphology" *Adv. Funct. Mater.* **2005**, *15*, 1617.
[55] D. Chen, A. Nakahara, D. Wei, D. Nordlund, T. P. Russell, "P3HT/PCBM bulk heterojunction organic photovoltaics: correlating efficiency and morphology" *Nano Lett.* **2011**, *11*, 561.
[56] T. Erb, U. Zhokhavets, G. Gobsch, S. Raleva, B. Stühn, P. Schilinsky, C. Waldauf, C. J. Brabec, "Correlation between structural and optical properties of composite polymer/fullerene films for organic solar cells" *Adv. Funct. Mater.* **2005**, *15*, 1193.
[57] G. Li, Y. Yao, H. Yang, V. Shrotriya, G. Yang, Y. Yang, "“Solvent annealing” effect in polymer solar cells based on poly(3-hexylthiophene) and methanofullerenes" *Adv. Funct. Mater.* **2007**, *17*, 1636.
[58] S. Miller, G. Fanchini, Y.-Y. Lin, C. Li, C.-W. Chen, W.-F. Su, M. Chhowalla, "Investigation of nanoscale morphological changes in organic photovoltaics during solvent vapor annealing" *J. Mater. Chem.* **2008**, *18*, 306.
[59] V. D. Mihailetchi, H. Xie, B. de Boer, L. M. Popescu, J. C. Hummelen, P. W. M. Blom, L. J. A. Koster, "Origin of the enhanced performance in poly(3-hexylthiophene): [6,6]-phenyl C[sub 61]-butyric acid methyl ester solar cells upon slow drying of the active layer" *Appl. Phys. Lett.* **2006**, *89*, 012107.
[60] M. T. Dang, J. D. Wuest, "Using volatile additives to alter the morphology and performance of active layers in thin-film molecular photovoltaic devices incorporating bulk heterojunctions" *Chem. Soc. Rev.* **2013**, *42*, 9105.
[61] H.-H. Liao, L.-M. Chen, Z. Xu, G. Li, Y. Yang, "Highly efficient inverted polymer solar cell by low temperature annealing of Cs_2CO_3 interlayer" *Appl. Phys. Lett.* **2008**, *92*, 173303.
[62] J. K. Lee, W. L. Ma, C. J. Brabec, J. Yuen, J. S. Moon, J. Y. Kim, K. Lee, G. C. Bazan, A. J. Heeger, "Processing additives for improved efficiency from bulk heterojunction solar cells" *J. Am. Chem. Soc.* **2008**, *130*, 3619.
[63] Y. Yao, J. Hou, Z. Xu, G. Li, Y. Yang, "Effects of solvent mixtures on the nanoscale phase separation in polymer solar cells" *Adv. Funct. Mater.* **2008**, *18*, 1783.
[64] J. T. Rogers, K. Schmidt, M. F. Toney, E. J. Kramer, G. C. Bazan, "Structural order in bulk heterojunction films prepared with solvent additives" *Adv. Mater.* **2011**, *23*, 2284.
[65] S. Lou, J. Szarko, T. Xu, L. Yu, T. Marks, L. Chen, "Effects of additives on the morphology of solution phase aggregates formed by active layer components of high-efficiency organic solar cells" *J. Am. Chem. Soc.* **2011**, *133*, 20661.

[66] D. Angmo, S. a. Gevorgyan, T. T. Larsen-Olsen, R. R. Søndergaard, M. Hösel, M. Jørgensen, R. Gupta, G. U. Kulkarni, F. C. Krebs, "Scalability and stability of very thin, roll-to-roll processed, large area, indium-tin-oxide free polymer solar cell modules" *Org. Electron.* **2013**, *14*, 984.
[67] A. Elschner, S. Kirchmeyer, W. Lovenich, U. Merker, K. Reuter, *PEDOT: Principles and Applications of an Intrinsically Conductive Polymer*, CRC Press, Boca Raton, FL **2011**.
[68] X. Crispin, F. L. E. Jakobsson, A. Crispin, P. C. M. Grim, P. Andersson, A. Volodin, C. van Haesendonck, M. Van der Auweraer, W. R. Salaneck, M. Berggren, "The origin of the high conductivity of poly(3,4-ethylenedioxythiophene)−poly(styrenesulfonate) (PEDOT−PSS) plastic electrodes" *Chem. Mater.* **2006**, *18*, 4354.
[69] S. H. Ahn, L. J. Guo, "Large-area roll-to-roll and roll-to-plate nanoimprint lithography: a step toward high-throughput application of continuous nanoimprinting" *ACS nano* **2009**, *3*, 2304.
[70] M.-G. Kang, M.-S. Kim, J. Kim, L. J. Guo, "Organic solar cells using nanoimprinted transparent metal electrodes" *Adv. Mater.* **2008**, *20*, 4408.
[71] J.-Y. Lee, S. T. Connor, Y. Cui, P. Peumans, "Solution-processed metal nanowire mesh transparent electrodes" *Nano Lett.* **2008**, *8*, 689.
[72] J. Krantz, M. Richter, S. Spallek, E. Spiecker, C. J. Brabec, "Solution-processed metallic nanowire electrodes as indium tin oxide replacement for thin-film solar cells" *Adv. Funct. Mater.* **2011**, *21*, 4784.
[73] J. Krantz, T. Stubhan, M. Richter, S. Spallek, I. Litzov, G. J. Matt, E. Spiecker, C. J. Brabec, "Spray-coated silver nanowires as top electrode layer in semitransparent P3HT:PCBM-based organic solar cell devices" *Adv. Funct. Mater.* **2013**, *23*, 1711.
[74] S. Bae, H. Kim, Y. Lee, X. Xu, J.-S. Park, Y. Zheng, J. Balakrishnan, T. Lei, H. R. Kim, Y. I. Song, Y.-J. Kim, K. S. Kim, B. Ozyilmaz, J.-H. Ahn, B. H. Hong, S. Iijima, "Roll-to-roll production of 30-inch graphene films for transparent electrodes" *Nat. Nanotechnol.* **2010**, *5*, 574.
[75] V. D. Mihailetchi, P. W. M. Blom, J. C. Hummelen, M. T. Rispens, "Cathode dependence of the open-circuit voltage of polymer:fullerene bulk heterojunction solar cells" *J. Appl. Phys.* **2003**, *94*, 6849.
[76] K. M. O'Malley, C.-Z. Li, H.-L. Yip, A. K. Y. Jen, "Enhanced open-circuit voltage in high performance polymer/fullerene bulk-heterojunction solar cells by cathode modification with a C60 surfactant" *Adv. Energy Mater.* **2012**, *2*, 82.
[77] L.-M. Chen, Z. Xu, Z. Hong, Y. Yang, "Interface investigation and engineering - achieving high performance polymer photovoltaic devices" *J. Mater. Chem.* **2010**, *20*, 2575.
[78] R. Steim, F. R. Kogler, C. J. Brabec, "Interface materials for organic solar cells" *J. Mater. Chem.* **2010**, *20*, 2499.
[79] H.-L. Yip, A. K. Y. Jen, "Recent advances in solution-processed interfacial materials for efficient and stable polymer solar cells" *Energy Environ. Sci.* **2012**, *5*, 5994.
[80] R. Po, C. Carbonera, A. Bernardi, N. Camaioni, "The role of buffer layers in polymer solar cells" *Energy Environ. Sci.* **2011**, *4*, 285.
[81] L. Vayssieres, "Growth of arrayed nanorods and nanowires of ZnO from aqueous solutions" *Adv. Mater.* **2003**, *15*, 464.

[82] M. S. White, D. C. Olson, S. E. Shaheen, N. Kopidakis, D. S. Ginley, "Inverted bulk-heterojunction organic photovoltaic device using a solution-derived ZnO underlayer" *Appl. Phys. Lett.* **2006**, *89*, 143517.
[83] J. Gilot, I. Barbu, M. M. Wienk, R. a. J. Janssen, "The use of ZnO as optical spacer in polymer solar cells: Theoretical and experimental study" *Appl. Phys. Lett.* **2007**, *91*, 113520.
[84] S. K. Hau, H.-L. Yip, N. S. Baek, J. Zou, K. O'Malley, A. K. Y. Jen, "Air-stable inverted flexible polymer solar cells using zinc oxide nanoparticles as an electron selective layer" *Appl. Phys. Lett.* **2008**, *92*, 253301.
[85] A. K. K. Kyaw, X. W. Sun, C. Y. Jiang, G. Q. Lo, D. W. Zhao, D. L. Kwong, "An inverted organic solar cell employing a sol-gel derived ZnO electron selective layer and thermal evaporated MoO[sub 3] hole selective layer" *Appl. Phys. Lett.* **2008**, *93*, 221107.
[86] C. Waldauf, M. Morana, P. Denk, P. Schilinsky, K. Coakley, S. A. Choulis, C. J. Brabec, "Highly efficient inverted organic photovoltaics using solution based titanium oxide as electron selective contact" *Appl. Phys. Lett.* **2006**, *89*, 233517.
[87] A. Hayakawa, O. Yoshikawa, T. Fujieda, K. Uehara, S. Yoshikawa, "High performance polythiophene/fullerene bulk-heterojunction solar cell with a TiO_x hole blocking layer" *Appl. Phys. Lett.* **2007**, *90*, 163517.
[88] K. Lee, J. Y. Kim, S. H. Park, S. H. Kim, S. Cho, A. J. Heeger, "Air-stable polymer electronic devices" *Adv. Mater.* **2007**, *19*, 2445.
[89] G. K. Mor, K. Shankar, M. Paulose, O. K. Varghese, C. a. Grimes, "High efficiency double heterojunction polymer photovoltaic cells using highly ordered TiO_2 nanotube arrays" *Appl. Phys. Lett.* **2007**, *91*, 152111.
[90] R. Steim, S. A. Choulis, P. Schilinsky, C. J. Brabec, "Interface modification for highly efficient organic photovoltaics" *Appl. Phys. Lett.* **2008**, *92*, 093303.
[91] V. Shrotriya, G. Li, Y. Yao, C.-W. Chu, Y. Yang, "Transition metal oxides as the buffer layer for polymer photovoltaic cells" *Appl. Phys. Lett.* **2006**, *88*, 073508.
[92] M. Y. Chan, C. S. Lee, S. L. Lai, M. K. Fung, F. L. Wong, H. Y. Sun, K. M. Lau, S. T. Lee, "Efficient organic photovoltaic devices using a combination of exciton blocking layer and anodic buffer layer" *J. Appl. Phys.* **2006**, *100*, 94506.
[93] S. Han, W. S. Shin, M. Seo, D. Gupta, S.-J. Moon, S. Yoo, "Improving performance of organic solar cells using amorphous tungsten oxides as an interfacial buffer layer on transparent anodes" *Org. Electron.* **2009**, *10*, 791.
[94] C. Tao, S. Ruan, G. Xie, X. Kong, L. Shen, F. Meng, C. Liu, X. Zhang, W. Dong, W. Chen, "Role of tungsten oxide in inverted polymer solar cells" *Appl. Phys. Lett.* **2009**, *94*, 043311.
[95] K. Takanezawa, K. Tajima, K. Hashimoto, "Efficiency enhancement of polymer photovoltaic devices hybridized with ZnO nanorod arrays by the introduction of a vanadium oxide buffer layer" *Appl. Phys. Lett.* **2008**, *93*, 063308.
[96] J.-S. Huang, C.-Y. Chou, M.-Y. Liu, K.-H. Tsai, W.-H. Lin, C.-F. Lin, "Solution-processed vanadium oxide as an anode interlayer for inverted polymer solar cells hybridized with ZnO nanorods" *Org. Electron.* **2009**, *10*, 1060.
[97] M. D. Irwin, D. B. Buchholz, A. W. Hains, R. P. H. Chang, T. J. Marks, "p-Type semiconducting nickel oxide as an efficiency-enhancing anode interfacial layer in polymer bulk-heterojunction solar cells" *Proc. Natl. Acad. Sci.* **2008**, *105*, 2783.

[98] A. W. Hains, T. J. Marks, "High-efficiency hole extraction/electron-blocking layer to replace poly(3,4-ethylenedioxythiophene):poly(styrene sulfonate) in bulk-heterojunction polymer solar cells" *Appl. Phys. Lett.* **2008**, *92*, 023504.
[99] A. W. Hains, J. Liu, A. B. F. Martinson, M. D. Irwin, T. J. Marks, "Anode interfacial tuning via electron-blocking/hole-transport layers and indium tin oxide surface treatment in bulk-heterojunction organic photovoltaic cells" *Adv. Funct. Mater.* **2010**, *20*, 595.
[100] A. W. Hains, C. Ramanan, M. D. Irwin, J. Liu, M. R. Wasielewski, T. J. Marks, "Designed bithiophene-based interfacial layer for high-efficiency bulk-heterojunction organic photovoltaic cells. Importance of interfacial energy level matching" *ACS Appl. Mater. Interfaces* **2010**, *2*, 175.
[101] Y. Sun, S.-C. Chien, H.-L. Yip, Y. Zhang, K.-S. Chen, D. F. Zeigler, F.-C. Chen, B. Lin, A. K. Y. Jen, "Chemically doped and cross-linked hole-transporting materials as an efficient anode buffer layer for polymer solar cells" *Chem. Mater.* **2011**, *23*, 5006.
[102] Y. Sun, M. Wang, X. Gong, J. H. Seo, B. B. Y. Hsu, F. Wudl, A. J. Heeger, "Polymer bulk heterojunction solar cells: function and utility of inserting a hole transport and electron blocking layer into the device structure" *J. Mater. Chem.* **2011**, *21*, 1365.
[103] S. K. M. Jönsson, E. Carlegrim, F. Zhang, W. R. Salaneck, M. Fahlman, "Photoelectron spectroscopy of the contact between the cathode and the active layers in plastic solar cells: the role of LiF" *Jpn. J. Appl. Phys.* **2005**, *44*, 3695.
[104] T. M. Brown, R. H. Friend, I. S. Millard, D. J. Lacey, J. H. Burroughes, F. Cacialli, "LiF/Al cathodes and the effect of LiF thickness on the device characteristics and built-in potential of polymer light-emitting diodes" *Appl. Phys. Lett.* **2000**, *77*, 3096.
[105] G. Li, C. W. Chu, V. Shrotriya, J. Huang, Y. Yang, "Efficient inverted polymer solar cells" *Appl. Phys. Lett.* **2006**, *88*, 253503.
[106] J. Huang, Z. Xu, Y. Yang, "Low-work-function surface formed by solution-processed and thermally deposited nanoscale layers of cesium carbonate" *Adv. Funct. Mater.* **2007**, *17*, 1966.
[107] J. Luo, H. Wu, C. He, A. Li, W. Yang, Y. Cao, "Enhanced open-circuit voltage in polymer solar cells" *Appl. Phys. Lett.* **2009**, *95*, 043301.
[108] S.-I. Na, S.-H. Oh, S.-S. Kim, D.-Y. Kim, "Efficient organic solar cells with polyfluorene derivatives as a cathode interfacial layer" *Org. Electron.* **2009**, *10*, 496.
[109] S.-H. Oh, S.-I. Na, J. Jo, B. Lim, D. Vak, D.-Y. Kim, "Water-soluble polyfluorenes as an interfacial layer leading to cathode-independent high performance of organic solar cells" *Adv. Funct. Mater.* **2010**, *20*, 1977.
[110] Y. Zhao, Z. Xie, C. Qin, Y. Qu, Y. Geng, L. Wang, "Enhanced charge collection in polymer photovoltaic cells by using an ethanol-soluble conjugated polyfluorene as cathode buffer layer" *Sol. Energy Mater. Sol. Cells* **2009**, *93*, 604.
[111] F. Zhang, M. Ceder, O. Inganäs, "Enhancing the photovoltage of polymer solar cells by using a modified cathode" *Adv. Mater.* **2007**, *19*, 1835.
[112] F.-C. Chen, S.-C. Chien, "Nanoscale functional interlayers formed through spontaneous vertical phase separation in polymer photovoltaic devices" *J. Mater. Chem.* **2009**, *19*, 6865.
[113] Y. Zhou, F. Li, S. Barrau, W. Tian, O. Inganäs, F. Zhang, "Inverted and transparent polymer solar cells prepared with vacuum-free processing" *Sol. Energy Mater. Sol. Cells* **2009**, *93*, 497.

[114] C. He, C. Zhong, H. Wu, R. Yang, W. Yang, F. Huang, G. C. Bazan, Y. Cao, "Origin of the enhanced open-circuit voltage in polymer solar cells via interfacial modification using conjugated polyelectrolytes" *J. Mater. Chem.* **2010**, *20*, 2617.
[115] J. W. Jung, J. W. Jo, W. H. Jo, "Enhanced performance and air stability of polymer solar cells by formation of a self-assembled buffer layer from fullerene-end-capped poly(ethylene glycol)" *Adv. Mater.* **2011**, *23*, 1782.
[116] C.-Z. Li, C.-C. Chueh, H.-L. Yip, K. M. O'Malley, W.-C. Chen, A. K.-Y. Jen, "Effective interfacial layer to enhance efficiency of polymer solar cells via solution-processed fullerene-surfactants" *J. Mater. Chem.* **2012**, *22*, 8574.
[117] J. Y. Kim, S. H. Kim, H. H. Lee, K. Lee, W. Ma, X. Gong, A. J. Heeger, "New architecture for high-efficiency polymer photovoltaic cells using solution-based titanium oxide as an optical spacer" *Adv. Mater.* **2006**, *18*, 572.
[118] S. K. Hau, H.-L. Yip, A. K. Y. Jen, "A review on the development of the inverted polymer solar cell architecture" *Polym. Rev.* **2010**, *50*, 474.
[119] S. K. Hau, H.-L. Yip, K. Leong, A. K. Y. Jen, "Spraycoating of silver nanoparticle electrodes for inverted polymer solar cells" *Org. Electron.* **2009**, *10*, 719.
[120] F. C. Krebs, N. Espinosa, M. Hösel, R. R. Søndergaard, M. Jørgensen, "25th anniversary article: rise to power - OPV-based solar parks" *Adv. Mater.* **2014**, *26*, 29.
[121] F. C. Krebs, S. A. Gevorgyan, J. Alstrup, "A roll-to-roll process to flexible polymer solar cells: model studies, manufacture and operational stability studies" *J. Mater. Chem.* **2009**, *19*, 5442.
[122] A. Hadipour, B. Deboer, P. Blom, "Device operation of organic tandem solar cells" *Org. Electron.* **2008**, *9*, 617.
[123] G. Dennler, M. C. Scharber, T. Ameri, P. Denk, K. Forberich, C. Waldauf, C. J. Brabec, "Design rules for donors in bulk-heterojunction tandem solar cells? Towards 15 % energy-conversion efficiency" *Adv. Mater.* **2008**, *20*, 579.
[124] A. Hadipour, B. de Boer, P. W. M. Blom, "Organic tandem and multi-junction solar cells" *Adv. Funct. Mater.* **2008**, *18*, 169.
[125] T. Ameri, G. Dennler, C. Lungenschmied, C. J. Brabec, "Organic tandem solar cells: A review" *Energy Environ. Sci.* **2009**, *2*, 347.
[126] S. Sista, Z. Hong, L.-M. Chen, Y. Yang, "Tandem polymer photovoltaic cells—current status, challenges and future outlook" *Energy Environ. Sci.* **2011**, *4*, 1606.
[127] J. You, L. Dou, Z. Hong, G. Li, Y. Yang, "Recent trends in polymer tandem solar cells research" *Prog. Polym. Sci.* **2013**, *38*, 1909.
[128] J. You, L. Dou, K. Yoshimura, T. Kato, K. Ohya, T. Moriarty, K. Emery, C.-C. Chen, J. Gao, G. Li, Y. Yang, "A polymer tandem solar cell with 10.6% power conversion efficiency" *Nat. Commun.* **2013**, *4*, 1446.
[129] W. Gaynor, J.-Y. Lee, P. Peumans, "Fully solution-processed inverted polymer solar cells with laminated nanowire electrodes" *ACS Nano* **2010**, *4*, 30.
[130] S. K. Hau, H.-L. Yip, J. Zou, A. K.-Y. Jen, "Indium tin oxide-free semi-transparent inverted polymer solar cells using conducting polymer as both bottom and top electrodes" *Org. Electron.* **2009**, *10*, 1401.
[131] J. Huang, G. Li, Y. Yang, "A Semi-transparent plastic solar cell fabricated by a lamination process" *Adv. Mater.* **2008**, *20*, 415.
[132] X. Wang, T. Ishwara, W. Gong, M. Campoy-Quiles, J. Nelson, D. D. C. Bradley, "High-performance metal-free solar cells using stamp transfer printed vapor phase

polymerized poly(3,4-ethylenedioxythiophene) top anodes" *Adv. Funct. Mater.* **2012**, *22*, 1454.
[133] Y. Xia, K. Sun, J. Ouyang, "Highly conductive poly(3,4-ethylenedioxythiophene):poly(styrene sulfonate) films treated with an amphiphilic fluoro compound as the transparent electrode of polymer solar cells" *Energy Environ. Sci.* **2012**, *5*, 5325.
[134] Y. Zhou, H. Cheun, S. Choi, C. Fuentes-Hernandez, B. Kippelen, "Optimization of a polymer top electrode for inverted semitransparent organic solar cells" *Org. Electron.* **2011**, *12*, 827.
[135] H. Zhou, L. Yang, W. You, "Rational design of high performance conjugated polymers for organic solar cells" *Macromolecules* **2012**, *45*, 607.
[136] H. Bronstein, R. S. Ashraf, Y. Kim, A. J. P. White, T. Anthopoulos, K. Song, D. James, W. Zhang, I. McCulloch, "Synthesis of a novel fused thiophene-thieno[3,2-b]thiophene-thiophene donor monomer and co-polymer for use in OPV and OFETs" *Macromol. Rapid Commun.* **2011**, *32*, 1664.
[137] H. Bronstein, D. S. Leem, R. Hamilton, P. Woebkenberg, S. King, W. Zhang, R. S. Ashraf, M. Heeney, T. D. Anthopoulos, J. D. Mello, I. McCulloch, "Indacenodithiophene- co -benzothiadiazole copolymers for high performance solar cells or transistors via alkyl chain optimization" *Macromolecules* **2011**, *44*, 6649.
[138] S.-H. Chan, C.-P. Chen, T.-C. Chao, C. Ting, C.-S. Lin, B.-T. Ko, "Synthesis, characterization, and photovoltaic properties of novel semiconducting polymers with thiophene−phenylene−thiophene (TPT) as coplanar units" *Macromolecules* **2008**, *41*, 5519.
[139] C.-Y. Chang, Y.-J. Cheng, S.-H. Hung, J.-S. Wu, W.-S. Kao, C.-H. Lee, C.-S. Hsu, "Combination of molecular, morphological, and interfacial engineering to achieve highly efficient and stable plastic solar cells" *Adv. Mater.* **2012**, *24*, 549.
[140] C.-P. Chen, S.-H. Chan, T.-C. Chao, C. Ting, B.-T. Ko, "Low-bandgap poly(thiophene-phenylene-thiophene) derivatives with broaden absorption spectra for use in high-performance bulk-heterojunction polymer solar cells" *J. Am. Chem. Soc.* **2008**, *130*, 12828.
[141] Y.-J. Cheng, C.-H. Chen, Y.-S. Lin, C.-Y. Chang, C.-S. Hsu, "Ladder-type nonacyclic structure consisting of alternate thiophene and benzene units for efficient conventional and inverted organic photovoltaics" *Chem. Mater.* **2011**, *23*, 5068.
[142] Y.-J. Cheng, S.-W. Cheng, C.-Y. Chang, W.-S. Kao, M.-H. Liao, C.-S. Hsu, "Diindenothieno[2,3-b]thiophene arene for efficient organic photovoltaics with an extra high open-circuit voltage of 1.14 ev" *Chem. Commun.* **2012**, *48*, 3203.
[143] Y.-J. Cheng, J.-S. Wu, P.-I. Shih, C.-Y. Chang, P.-C. Jwo, W.-S. Kao, C.-S. Hsu, "Carbazole-based ladder-type heptacylic arene with aliphatic side chains leading to enhanced efficiency of organic photovoltaics" *Chem. Mater.* **2011**, *23*, 2361.
[144] Z. Fei, R. S. Ashraf, Z. Huang, J. Smith, R. J. Kline, P. D'Angelo, T. D. Anthopoulos, J. R. Durrant, I. McCulloch, M. Heeney, "Germaindacenodithiophene based low band gap polymers for organic solar cells" *Chem. Commun.* **2012**, *48*, 2955.
[145] I. McCulloch, R. S. Ashraf, L. Biniek, H. Bronstein, C. Combe, J. E. Donaghey, D. I. James, C. B. Nielsen, B. C. Schroeder, W. Zhang, "Design of semiconducting indacenodithiophene polymers for high performance transistors and solar cells" *Acc. Chem. Res.* **2012**, *45*, 714.

[146] B. C. Schroeder, R. S. Ashraf, S. Thomas, A. J. P. White, L. Biniek, C. B. Nielsen, W. Zhang, Z. Huang, P. S. Tuladhar, S. E. Watkins, T. D. Anthopoulos, J. R. Durrant, I. McCulloch, "Synthesis of novel thieno[3,2-b]thienobis(silolothiophene) based low bandgap polymers for organic photovoltaics" *Chem. Commun.* **2012**, *48*, 7699.
[147] J.-Y. Wang, S. K. Hau, H.-L. Yip, J. a. Davies, K.-S. Chen, Y. Zhang, Y. Sun, A. K. Y. Jen, "Benzobis(silolothiophene)-based low bandgap polymers for efficient polymer solar cells " *Chem. Mater.* **2011**, *23*, 765.
[148] J.-S. Wu, Y.-J. Cheng, M. Dubosc, C.-H. Hsieh, C.-Y. Chang, C.-S. Hsu, "Donor-acceptor polymers based on multi-fused heptacyclic structures: synthesis, characterization and photovoltaic applications" *Chem. Commun.* **2010**, *46*, 3259.
[149] C.-Y. Yu, C.-P. Chen, S.-H. Chan, G.-W. Hwang, C. Ting, "Thiophene/phenylene/thiophene-based low-bandgap conjugated polymers for efficient near-infrared photovoltaic applications" *Chem. Mater.* **2009**, *21*, 3262.
[150] Q. Zheng, B. J. Jung, J. Sun, H. E. Katz, "Ladder-type oligo-p-phenylene-containing copolymers with high open-circuit voltages and ambient photovoltaic activity" *J. Am. Chem. Soc.* **2010**, *132*, 5394.
[151] D. Hertel, U. Scherf, H. Bässler, "Charge carrier mobility in a ladder-type conjugated polymer" *Adv. Mater.* **1998**, *10*, 1119.
[152] J. Roncali, "Molecular engineering of the band gap of π-conjugated systems: facing technological applications" *Macromol. Rapid Commun.* **2007**, *28*, 1761.
[153] C. Schwarz, H. Bässler, I. Bauer, J.-m. Koenen, E. Preis, U. Scherf, A. Köhler, "Does conjugation help exciton dissociation? a study on poly(p-phenylene)s in planar heterojunctions with C60 or TNF" *Adv. Mater.* **2012**, *24*, 922.
[154] X. Wang, H. Luo, Y. Sun, M. Zhang, X. Li, G. Yu, Y. Liu, Y. Li, H. Wang, "Narrow band gap D-A copolymer of indacenodithiophene and diketopyrrolopyrrole with deep HOMO level: Synthesis and application in field-effect transistors and polymer solar cells" *J. Polym. Sci., Part A: Polym. Chem.* **2012**, *50*, 371.
[155] Y. Zhang, J. Zou, H.-L. Yip, K.-S. Chen, D. F. Zeigler, Y. Sun, A. K. Y. Jen, "Indacenodithiophene and quinoxaline-based conjugated polymers for highly efficient polymer solar cells" *Chem. Mater.* **2011**, *23*, 2289.
[156] W. Zhang, J. Smith, S. E. Watkins, R. Gysel, M. McGehee, A. Salleo, J. Kirkpatrick, S. Ashraf, T. Anthopoulos, M. Heeney, I. McCulloch, "Indacenodithiophene semiconducting polymers for high-performance, air-stable transistors" *J. Am. Chem. Soc.* **2010**, *132*, 11437.
[157] Y.-C. Chen, C. Y. Yu, Y. L. Fan, L. I. Hung, C. P. Chen, C. Ting, "Low-bandgap conjugated polymer for high efficient photovoltaic applications" *Chem. Commun.* **2010**, *46*, 6503.
[158] R. S. Ashraf, Z. Chen, D. S. Leem, H. Bronstein, W. Zhang, B. Schroeder, Y. Geerts, J. Smith, S. Watkins, T. D. Anthopoulos, H. Sirringhaus, J. C. de Mello, M. Heeney, I. McCulloch, "Silaindacenodithiophene semiconducting polymers for efficient solar cells and high-mobility ambipolar transistors" *Chem. Mater.* **2011**, *23*, 768.
[159] M. Zhang, X. Guo, X. Wang, H. Wang, Y. Li, "Synthesis and photovoltaic properties of D–A copolymers based on alkyl-substituted indacenodithiophene donor unit" *Chem. Mater.* **2011**, *23*, 4264.

[160] K.-S. Chen, Y. Zhang, H.-L. Yip, Y. Sun, J. a. Davies, C. Ting, C.-P. Chen, A. K. Y. Jen, "Highly efficient indacenodithiophene-based polymeric solar cells in conventional and inverted device configurations" *Org. Electron.* **2011**, *12*, 794.
[161] Y. Sun, S.-C. Chien, H.-L. Yip, K.-S. Chen, Y. Zhang, J. a. Davies, F.-C. Chen, B. Lin, A. K. Y. Jen, "Improved thin film morphology and bulk-heterojunction solar cell performance through systematic tuning of the surface energy of conjugated polymers" *J. Mater. Chem.* **2012**, *22*, 5587.
[162] Y. Sun, S.-C. Chien, H.-L. Yip, Y. Zhang, K.-S. Chen, D. F. Zeigler, F.-C. Chen, B. Lin, A. K. Y. Jen, "High-mobility low-bandgap conjugated copolymers based on indacenodithiophene and thiadiazolo[3,4-c]pyridine units for thin film transistor and photovoltaic applications" *J. Mater. Chem.* **2011**, *21*, 13247.
[163] J.-Y. Wang, S. K. Hau, H.-L. Yip, J. a. Davies, K.-S. Chen, Y. Zhang, Y. Sun, A. K. Y. Jen, "Benzobis(silolothiophene)-based low bandgap polymers for efficient polymer solar cells †" *Chem. Mater.* **2011**, *23*, 765.
[164] Y. Zhang, S.-C. Chien, K.-S. Chen, H.-L. Yip, Y. Sun, J. a. Davies, F.-C. Chen, A. K. Y. Jen, "Increased open circuit voltage in fluorinated benzothiadiazole-based alternating conjugated polymers" *Chem. Commun.* **2011**, *47*, 11026.
[165] Y. Zhang, J. Zou, H.-L. Yip, K.-S. Chen, J. A. Davies, Y. Sun, A. K. Y. Jen, "Synthesis, characterization, charge transport, and photovoltaic properties of dithienobenzoquinoxaline- and dithienobenzopyridopyrazine-based conjugated polymers" *Macromolecules* **2011**, *44*, 4752.
[166] Y. Zhang, J. Zou, H.-L. Yip, Y. Sun, J. a. Davies, K.-S. Chen, O. Acton, A. K. Y. Jen, "Conjugated polymers based on C, Si and N-bridged dithiophene and thienopyrroledione units: synthesis, field-effect transistors and bulk heterojunction polymer solar cells" *J. Mater. Chem.* **2011**, *21*, 3895.
[167] a. Gadisa, W. Mammo, L. M. Andersson, S. Admassie, F. Zhang, M. R. Andersson, O. Inganäs, "A new donor–acceptor–donor polyfluorene copolymer with balanced electron and hole mobility" *Adv. Funct. Mater.* **2007**, *17*, 3836.
[168] D. Kitazawa, N. Watanabe, S. Yamamoto, J. Tsukamoto, "Quinoxaline-based π-conjugated donor polymer for highly efficient organic thin-film solar cells" *Appl. Phys. Lett.* **2009**, *95*, 053701.
[169] L. J. Lindgren, F. Zhang, M. Andersson, S. Barrau, S. Hellström, W. Mammo, E. Perzon, O. Inganäs, M. R. Andersson, "Synthesis, characterization, and devices of a series of alternating copolymers for solar cells" *Chem. Mater.* **2009**, *21*, 3491.
[170] F. Zhang, J. Bijleveld, E. Perzon, K. Tvingstedt, S. Barrau, O. Inganäs, M. R. Andersson, "High photovoltage achieved in low band gap polymer solar cells by adjusting energy levels of a polymer with the LUMOs of fullerene derivatives" *J. Mater. Chem.* **2008**, *18*, 5468.
[171] E. Zhou, J. Cong, K. Tajima, K. Hashimoto, "Synthesis and photovoltaic properties of donor−acceptor copolymers based on 5,8-dithien-2-yl-2,3-diphenylquinoxaline" *Chem. Mater.* **2010**, *22*, 4890.
[172] J. Zaumseil, H. Sirringhaus, "Electron and ambipolar transport in organic field-effect transistors" *Chem. Rev.* **2007**, *107*, 1296.
[173] D. Di Nuzzo, G.-J. a. H. Wetzelaer, R. K. M. Bouwer, V. S. Gevaerts, S. C. J. Meskers, J. C. Hummelen, P. W. M. Blom, R. a. J. Janssen, "Simultaneous open-circuit voltage enhancement and short-circuit current loss in polymer: fullerene solar cells

correlated by reduced quantum efficiency for photoinduced electron transfer" *Adv. Energy Mater.* **2013**, *3*, 85.
[174] E. T. Hoke, K. Vandewal, J. a. Bartelt, W. R. Mateker, J. D. Douglas, R. Noriega, K. R. Graham, J. M. J. Fréchet, A. Salleo, M. D. McGehee, "Recombination in polymer:fullerene solar cells with open-circuit voltages approaching and exceeding 1.0 V" *Adv. Energy Mater.* **2013**, *3*, 220.
[175] N. C. Miller, S. Sweetnam, E. T. Hoke, R. Gysel, C. E. Miller, J. a. Bartelt, X. Xie, M. F. Toney, M. D. McGehee, "Molecular packing and solar cell performance in blends of polymers with a bisadduct fullerene" *Nano Lett.* **2012**, *12*, 1566.
[176] G. F. Burkhard, E. T. Hoke, M. D. McGehee, "Accounting for interference, scattering, and electrode absorption to make accurate internal quantum efficiency measurements in organic and other thin solar cells" *Adv. Mater.* **2010**, *22*, 3293.
[177] H.-Y. Chen, J. Hou, S. Zhang, Y. Liang, G. Yang, Y. Yang, L. Yu, Y. Wu, G. Li, "Polymer solar cells with enhanced open-circuit voltage and efficiency" *Nat. Photonics* **2009**, *3*, 649.
[178] M. Liedtke, A. Sperlich, H. Kraus, A. Baumann, C. Deibel, M. J. M. Wirix, J. Loos, C. M. Cardona, V. Dyakonov, "Triplet exciton generation in bulk-heterojunction solar cells based on endohedral fullerenes" *J. Am. Chem. Soc.* **2011**, *133*, 9088.
[179] D. Veldman, S. C. J. Meskers, R. A. J. Janssen, "The energy of charge-transfer states in electron donor-acceptor blends: insight into the energy losses in organic solar cells" *Adv. Funct. Mater.* **2009**, *19*, 1939.
[180] G. J. Dutton, W. Jin, J. E. Reutt-Robey, S. W. Robey, "Ultrafast charge-transfer processes at an oriented phthalocyanine/C60 interface" *Phys. Rev. B* **2010**, *82*, 073407.
[181] N. Giebink, B. Lassiter, G. Wiederrecht, M. Wasielewski, S. Forrest, "Ideal diode equation for organic heterojunctions. II. The role of polaron pair recombination" *Phys. Rev. B* **2010**, *82*, 155306.
[182] L. J. A. Koster, S. E. Shaheen, J. C. Hummelen, "Pathways to a new efficiency regime for organic solar cells" *Adv. Energy Mater.* **2012**, *2*, 1246.
[183] D. Veldman, O. Ipek, S. C. Meskers, J. Sweelssen, M. M. Koetse, S. C. Veenstra, J. M. Kroon, S. S. van Bavel, J. Loos, R. A. Janssen, "Compositional and electric field dependence of the dissociation of charge transfer excitons in alternating polyfluorene copolymer/fullerene blends" *J. Am. Chem. Soc.* **2008**, *130*, 7721.
[184] S. Westenhoff, I. A. Howard, J. M. Hodgkiss, K. R. Kirov, H. A. Bronstein, C. K. Williams, N. C. Greenham, R. H. Friend, "Charge recombination in organic photovoltaic devices with high open-circuit voltages" *J. Am. Chem. Soc.* **2008**, *130*, 13653.
[185] C. W. Schlenker, K.-S. Chen, H.-L. Yip, C.-Z. Li, L. R. Bradshaw, S. T. Ochsenbein, F. Ding, X. S. Li, D. R. Gamelin, A. K. Y. Jen, D. S. Ginger, "Polymer triplet energy levels need not limit photocurrent collection in organic solar cells" *J. Am. Chem. Soc.* **2012**, *134*, 19661.
[186] J. J. Benson-Smith, H. Ohkita, S. Cook, J. R. Durrant, D. D. C. Bradley, J. Nelson, "Charge separation and fullerene triplet formation in blend films of polyfluorene polymers with [6,6]-phenyl C61 butyric acid methyl ester" *Dalton Trans.* **2009**, 10000.
[187] S. Cook, H. Ohkita, J. R. Durrant, Y. Kim, J. J. Benson-Smith, J. Nelson, D. D. C. Bradley, "Singlet exciton transfer and fullerene triplet formation in polymer-fullerene blend films" *Appl. Phys. Lett.* **2006**, *89*, 101128.

[188] H. Ohkita, S. Cook, Y. Astuti, W. Duffy, M. Heeney, S. Tierney, I. McCulloch, D. D. C. Bradley, J. R. Durrant, "Radical ion pair mediated triplet formation in polymer-fullerene blend films" *Chem. Commun.* **2006**, *100*, 3939.
[189] R. C. Coffin, J. Peet, J. Rogers, G. C. Bazan, "Streamlined microwave-assisted preparation of narrow-bandgap conjugated polymers for high-performance bulk heterojunction solar cells" *Nat. Chem.* **2009**, *1*, 657.
[190] E. Wang, L. Wang, L. Lan, C. Luo, W. Zhuang, J. Peng, Y. Cao, "High-performance polymer heterojunction solar cells of a polysilafluorene derivative" *Appl. Phys. Lett.* **2008**, *92*, 033307.
[191] H. Y. Chen, J. Hou, A. E. Hayden, H. Yang, K. N. Houk, Y. Yang, "Silicon atom substitution enhances interchain packing in a thiophene-based polymer system" *Adv. Mater.* **2010**, *22*, 371.
[192] M. C. Scharber, M. Koppe, J. Gao, F. Cordella, M. A. Loi, P. Denk, M. Morana, H. J. Egelhaaf, K. Forberich, G. Dennler, R. Gaudiana, D. Waller, Z. Zhu, X. Shi, C. J. Brabec, "Influence of the bridging atom on the performance of a low-bandgap bulk heterojunction solar cell" *Adv. Mater.* **2010**, *22*, 367.
[193] F. Zhang, K. G. Jespersen, C. Björström, M. Svensson, M. R. Andersson, V. Sundström, K. Magnusson, E. Moons, A. Yartsev, O. Inganäs, "Influence of solvent mixing on the morphology and performance of solar cells based on polyfluorene copolymer/fullerene blends" *Adv. Funct. Mater.* **2006**, *16*, 667.
[194] M.-H. Chen, J. Hou, Z. Hong, G. Yang, S. Sista, L.-M. Chen, Y. Yang, "Efficient polymer solar cells with thin active layers based on alternating polyfluorene copolymer/fullerene bulk heterojunctions" *Adv. Mater.* **2009**, *21*, 4238.
[195] S. C. Price, A. C. Stuart, L. Yang, H. Zhou, W. You, "Fluorine substituted conjugated polymer of medium band gap yields 7% efficiency in polymer−fullerene solar cells" *J. Am. Chem. Soc.* **2011**, *133*, 4625.
[196] B. C. Schroeder, Z. Huang, R. S. Ashraf, J. Smith, P. D'Angelo, S. E. Watkins, T. D. Anthopoulos, J. R. Durrant, I. McCulloch, "Silaindacenodithiophene-based low band gap polymers - the effect of fluorine substitution on device performances and film morphologies" *Adv. Funct. Mater.* **2012**, *22*, 1663.
[197] H. Zhou, L. Yang, A. C. Stuart, S. C. Price, S. Liu, W. You, "Development of fluorinated benzothiadiazole as a structural unit for a polymer solar cell of 7 % efficiency" *Angew. Chem. Int. Ed.* **2011**, *50*, 2995.
[198] N. S. Baek, S. K. Hau, H.-L. Yip, O. Acton, K.-S. Chen, A. K. Y. Jen, "High performance amorphous metallated π-conjugated polymers for field-effect transistors and polymer solar cells" *Chem. Mater.* **2008**, *20*, 5734.
[199] H. Bronstein, Z. Chen, R. S. Ashraf, W. Zhang, J. Du, J. R. Durrant, P. Shakya Tuladhar, K. Song, S. E. Watkins, Y. Geerts, M. M. Wienk, R. A. Janssen, T. Anthopoulos, H. Sirringhaus, M. Heeney, I. McCulloch, "Thieno[3,2-b]thiophene-diketopyrrolopyrrole-containing polymers for high-performance organic field-effect transistors and organic photovoltaic devices" *J. Am. Chem. Soc.* **2011**, *133*, 3272.
[200] I. McCulloch, M. Heeney, C. Bailey, K. Genevicius, I. Macdonald, M. Shkunov, D. Sparrowe, S. Tierney, R. Wagner, W. Zhang, M. L. Chabinyc, R. J. Kline, M. D. McGehee, M. F. Toney, "Liquid-crystalline semiconducting polymers with high charge-carrier mobility" *Nat. Mater.* **2006**, *5*, 328.

[201] Y.-X. Xu, C.-C. Chueh, H.-L. Yip, F.-Z. Ding, Y.-X. Li, C.-Z. Li, X. Li, W.-C. Chen, A. K.-Y. Jen, "Improved charge transport and absorption coefficient in indacenodithieno[3,2-b]thiophene-based ladder-type polymer leading to highly efficient polymer solar cells." *Adv. Mater.* **2012**, *24*, 6356.
[202] C. J. Brabec, M. Heeney, I. McCulloch, J. Nelson, "Influence of blend microstructure on bulk heterojunction organic photovoltaic performance" *Chem. Soc. Rev.* **2011**, *40*, 1185.
[203] R. Giridharagopal, D. S. Ginger, "Characterizing Morphology in Bulk Heterojunction Organic Photovoltaic Systems" *J. Phys. Chem. Lett.* **2010**, *1*, 1160.
[204] C. Groves, O. G. Reid, D. S. Ginger, "Heterogeneity in polymer solar cells: local morphology and performance in organic photovoltaics studied with scanning probe microscopy" *Acc. Chem. Res.* **2010**, *43*, 612.
[205] R. S. Ruoff, D. S. Tse, R. Malhotra, D. C. Lorents, "Solubility of C60 in a variety of solvents" *J. Phys. Chem.* **1993**, *97*, 3379.
[206] C. N. Hoth, P. Schilinsky, S. A. Choulis, C. J. Brabec, "Printing highly efficient organic solar cells" *Nano Lett.* **2008**, *8*, 2806.
[207] C.-D. Park, T. A. Fleetham, J. Li, B. D. Vogt, "High performance bulk-heterojunction organic solar cells fabricated with non-halogenated solvent processing" *Org. Electron.* **2011**, *12*, 1465.
[208] B. Schmidt-Hansberg, M. Sanyal, N. Grossiord, Y. Galagan, M. Baunach, M. F. G. Klein, A. Colsmann, P. Scharfer, U. Lemmer, H. Dosch, J. Michels, E. Barrena, W. Schabel, "Investigation of non-halogenated solvent mixtures for high throughput fabrication of polymer–fullerene solar cells" *Sol. Energy Mater. Sol. Cells* **2012**, *96*, 195.
[209] T. R. Andersen, T. T. Larsen-Olsen, B. Andreasen, A. P. L. Böttiger, J. E. Carlé, M. Helgesen, E. Bundgaard, K. Norrman, J. W. Andreasen, M. Jørgensen, F. C. Krebs, "Aqueous processing of low-band-gap polymer solar cells using roll-to-roll methods" *ACS Nano* **2011**, *5*, 4188.
[210] N. Espinosa, R. García-Valverde, A. Urbina, F. C. Krebs, "A life cycle analysis of polymer solar cell modules prepared using roll-to-roll methods under ambient conditions" *Sol. Energy Mater. Sol. Cells* **2011**, *95*, 1293.
[211] Q. Qiao, J. T. McLeskey, "Water-soluble polythiophene/nanocrystalline TiO_2 solar cells" *Appl. Phys. Lett.* **2005**, *86*, 153501.
[212] D. W. Acton, J. F. Barker, "In situ biodegradation potential of aromatic hydrocarbons in anaerobic groundwaters" *J. Contam. Hydrol.* **1992**, *9*, 325.
[213] S. Nilsson, A. Bernasik, A. Budkowski, E. Moons, "Morphology and phase segregation of spin-casted films of polyfluorene/PCBM blends" *Macromolecules* **2007**, *40*, 8291.
[214] G. Li, V. Shrotriya, Y. Yao, Y. Yang, "Investigation of annealing effects and film thickness dependence of polymer solar cells based on poly(3-hexylthiophene)" *J. Appl. Phys.* **2005**, *98*, 043704.
[215] H. Lu, B. Akgun, T. P. Russell, "Morphological characterization of a low-bandgap crystalline polymer:PCBM bulk heterojunction solar cells" *Adv. Energy Mater.* **2011**, *1*, 870.
[216] S. C. Price, A. C. Stuart, L. Yang, H. Zhou, W. You, "Fluorine substituted conjugated polymer of medium band gap yields 7% efficiency in polymer-fullerene solar cells" *J. Am. Chem. Soc.* **2011**, *133*, 4625.

[217] C. Chibbaro, M. Zimbone, G. Litrico, P. Baeri, M. L. Lo Trovato, F. Aleo, "A general and precise method to evaluate the series resistance of photovoltaic cells from I-V characteristics" *J. Appl. Phys.* **2011**, *110*, 044505.
[218] X. Yang, J. K. J. van Duren, R. A. J. Janssen, M. A. J. Michels, J. Loos, "Morphology and thermal stability of the active layer in poly(p-phenylenevinylene)/methanofullerene plastic photovoltaic devices" *Macromolecules* **2004**, *37*, 2151.
[219] H. Hoppe, M. Niggemann, C. Winder, J. Kraut, R. Hiesgen, A. Hinsch, D. Meissner, N. S. Sariciftci, "Nanoscale morphology of conjugated polymer/fullerene-based bulk- heterojunction solar cells" *Adv. Funct. Mater.* **2004**, *14*, 1005.
[220] M. T. Rispens, A. Meetsma, R. Rittberger, C. J. Brabec, N. S. Sariciftci, J. C. Hummelen, "Influence of the solvent on the crystal structure of PCBM and the efficiency of MDMO-PPV:PCBM 'plastic' solar cells" *Chem. Commun.* **2003**, 2116.
[221] M. a. Ruderer, S. Guo, R. Meier, H.-Y. Chiang, V. Körstgens, J. Wiedersich, J. Perlich, S. V. Roth, P. Müller-Buschbaum, "Solvent-Induced Morphology in Polymer-Based Systems for Organic Photovoltaics" *Adv. Funct. Mater.* **2011**, *21*, 3382.
[222] M.-S. Su, C.-Y. Kuo, M.-C. Yuan, U. S. Jeng, C.-J. Su, K.-H. Wei, "Improving device efficiency of polymer/fullerene bulk heterojunction solar cells through enhanced crystallinity and reduced grain boundaries induced by solvent additives" *Adv. Mater.* **2011**, 3315.
[223] J. C. Bijleveld, A. P. Zoombelt, S. G. J. Mathijssen, M. M. Wienk, M. Turbiez, D. M. de Leeuw, R. A. J. Janssen, "Poly(diketopyrrolopyrrole-terthiophene) for ambipolar logic and photovoltaics" *J. Am. Chem. Soc.* **2009**, *131*, 16616.
[224] C. Piliego, T. W. Holcombe, J. D. Douglas, C. H. Woo, P. M. Beaujuge, J. M. J. Fréchet, "Synthetic control of structural order in N-alkylthieno[3,4-c]pyrrole-4,6-dione-based polymers for efficient solar cells" *J. Am. Chem. Soc.* **2010**, *132*, 7595.
[225] Y. Sun, C. Cui, H. Wang, Y. Li, "Efficiency enhancement of polymer solar cells based on poly(3-hexylthiophene)/indene-C70 bisadduct via methylthiophene additive" *Adv. Energy Mater.* **2011**, *1*, 1058.
[226] C. V. Hoven, X.-D. Dang, R. C. Coffin, J. Peet, T.-Q. Nguyen, G. C. Bazan, "Patternable solution-crystallized organic transistors with high charge carrier mobility" *Adv. Energy Mater.* **2010**, *22*, E63.
[227] K. N. Semenov, N. a. Charykov, V. a. Keskinov, A. K. Piartman, A. a. Blokhin, A. a. Kopyrin, "Solubility of light fullerenes in organic solvents" *J. Chem. Eng. Data* **2010**, *55*, 13.
[228] Y. Zhang, Y. Matsuo, C.-Z. Li, H. Tanaka, E. Nakamura, "A scalable synthesis of methano[60]fullerene and congeners by the oxidative cyclopropanation reaction of silylmethylfullerene" *J. Am. Chem. Soc.* **2011**, *133*, 8086.
[229] C. Z. Li, Y. Matsuo, T. Niinomi, Y. Sato, E. Nakamura, "Face-to-face C6F5-[60]fullerene interaction for ordering fullerene molecules and application to thin-film organic photovoltaics" *Chem. Commun.* **2010**, *46*, 8582.
[230] R. R. Lunt, J. B. Benziger, S. R. Forrest, "Relationship between crystalline order and exciton diffusion length in molecular organic semiconductors" *Adv. Mater.* **2010**, *22*, 1233.

[231] S. R. Scully, M. D. McGehee, "Effects of optical interference and energy transfer on exciton diffusion length measurements in organic semiconductors" *J. Appl. Phys.* **2006**, *100*, 034907.
[232] D. E. Markov, E. Amsterdam, P. W. M. Blom, A. B. Sieval, J. C. Hummelen, "Accurate measurement of the exciton diffusion length in a conjugated polymer using a heterostructure with a side-chain cross-linked fullerene layer" *J. Phys. Chem. A* **2005**, *109*, 5266.
[233] T. Stübinger, W. Brütting, "Exciton diffusion and optical interference in organic donor–acceptor photovoltaic cells" *J. Appl. Phys.* **2001**, *90*, 3632.
[234] R. R. Lunt, N. C. Giebink, A. A. Belak, J. B. Benziger, S. R. Forrest, "Exciton diffusion lengths of organic semiconductor thin films measured by spectrally resolved photoluminescence quenching" *J. Appl. Phys.* **2009**, *105*, 053711.
[235] D. Ginger, N. Greenham, "Photoinduced electron transfer from conjugated polymers to CdSe nanocrystals" *Phys. Rev. B* **1999**, *59*, 10622.
[236] K. M. Noone, N. C. Anderson, N. E. Horwitz, A. M. Munro, A. P. Kulkarni, D. S. Ginger, "Absence of Photoinduced charge transfer in blends of PbSe quantum dots and conjugated polymers" *ACS Nano* **2009**, *3*, 1345.
[237] C. J. Brabec, S. Gowrisanker, J. J. M. Halls, D. Laird, S. Jia, S. P. Williams, "Polymer-fullerene bulk-heterojunction solar cells" *Adv. Mater.* **2010**, *22*, 3839.
[238] G. Li, R. Zhu, Y. Yang, "Polymer solar cells" *Nat. Photonics* **2012**, *6*, 153.
[239] F. C. Krebs, "Fabrication and processing of polymer solar cells: A review of printing and coating techniques" *Sol. Energy Mater. Sol. Cells* **2009**, *93*, 394.
[240] J. Y. Kim, S. H. Kim, H.-H. Lee, K. Lee, W. Ma, X. Gong, A. J. Heeger, "New architecture for high-efficiency polymer photovoltaic cells using solution-based titanium oxide as an optical spacer" *Adv. Mater.* **2006**, *18*, 572.
[241] A. Hadipour, D. Cheyns, P. Heremans, B. P. Rand, "Electrode Considerations for the optical enhancement of organic bulk heterojunction solar cells" *Adv. Energy Mater.* **2011**, *1*, 930.
[242] S. K. Hau, H.-L. Yip, K.-S. Chen, J. Zou, A. K.-Y. Jen, "Solution processed inverted tandem polymer solar cells with self-assembled monolayer modified interfacial layers" *Appl. Phys. Lett.* **2010**, *97*, 253307.
[243] J. You, C.-C. Chen, Z. Hong, K. Yoshimura, K. Ohya, R. Xu, S. Ye, J. Gao, G. Li, Y. Yang, "10.2% power conversion efficiency polymer tandem solar cells consisting of two identical sub-cells" *Adv. Mater.* **2013**, *25*, 3973.
[244] W. Li, A. Furlan, K. H. Hendriks, M. M. Wienk, R. a. J. Janssen, "Efficient tandem and triple-junction polymer solar cells" *J. Am. Chem. Soc.* **2013**, *135*, 5529.
[245] S.-W. Baek, J. Noh, C.-H. Lee, B. Kim, M.-K. Seo, J.-Y. Lee, "Plasmonic forward scattering effect in organic solar cells: a powerful optical engineering method" *Sci. Rep.* **2013**, *3*, 1726.
[246] M.-G. Kang, T. Xu, H. J. Park, X. Luo, L. J. Guo, "Efficiency enhancement of organic solar cells using transparent plasmonic Ag nanowire electrodes" *Adv. Mater.* **2010**, *22*, 4378.
[247] X. Li, W. C. H. Choy, L. Huo, F. Xie, W. E. I. Sha, B. Ding, X. Guo, Y. Li, J. Hou, J. You, Y. Yang, "Dual plasmonic nanostructures for high performance inverted organic solar cells" *Adv. Mater.* **2012**, *24*, 3046.

[248] J. Yang, J. You, C.-C. Chen, W.-C. Hsu, H.-r. Tan, X. W. Zhang, Z. Hong, Y. Yang, "Plasmonic polymer tandem solar cell" *ACS Nano* **2011**, *5*, 6210.
[249] X. Yang, C.-C. Chueh, C.-Z. Li, H.-L. Yip, P. Yin, H. Chen, W.-C. Chen, A. K. Y. Jen, "High-efficiency polymer solar cells achieved by doping plasmonic metallic nanoparticles into dual charge selecting interfacial layers to enhance light trapping" *Adv. Energy Mater.* **2013**, *3*, 666.
[250] S.-I. Na, S.-S. Kim, J. Jo, S.-H. Oh, J. Kim, D.-Y. Kim, "Efficient polymer solar cells with surface relief gratings fabricated by simple soft lithography" *Adv. Funct. Mater.* **2008**, *18*, 3956.
[251] L. Stolz Roman, O. Inganäs, T. Granlund, T. Nyberg, M. Svensson, M. R. Andersson, J. C. Hummelen, "Trapping light in polymer photodiodes with soft embossed gratings" *Adv. Mater.* **2000**, *12*, 189.
[252] D.-H. Ko, J. R. Tumbleston, L. Zhang, S. Williams, J. M. DeSimone, R. Lopez, E. T. Samulski, "Photonic crystal geometry for organic solar cells" *Nano Lett.* **2009**, *9*, 2742.
[253] J. D. Myers, W. Cao, V. Cassidy, S.-H. Eom, R. Zhou, L. Yang, W. You, J. Xue, "A universal optical approach to enhancing efficiency of organic-based photovoltaic devices" *Energy Environ. Sci.* **2012**, *5*, 6900.
[254] J. B. Kim, P. Kim, N. C. Pégard, S. J. Oh, C. R. Kagan, J. W. Fleischer, H. A. Stone, Y.-L. Loo, "Wrinkles and deep folds as photonic structures in photovoltaics" *Nat. Photonics* **2012**, *6*, 327.
[255] N. P. Sergeant, A. Hadipour, B. Niesen, D. Cheyns, P. Heremans, P. Peumans, B. P. Rand, "Design of transparent anodes for resonant cavity enhanced light harvesting in organic solar cells" *Adv. Mater.* **2012**, *24*, 728.
[256] H.-W. Lin, S.-W. Chiu, L.-Y. Lin, Z.-Y. Hung, Y.-h. Chen, F. Lin, K.-T. Wong, "Device engineering for highly efficient top-illuminated organic solar cells with microcavity structures." *Adv. Mater.* **2012**, *24*, 2269.
[257] Y. Long, "Improving optical performance of inverted organic solar cells by microcavity effect" *Appl. Phys. Lett.* **2009**, *95*, 193301.
[258] W. Yu, L. Shen, F. Meng, Y. Long, S. Ruan, W. Chen, "Effects of the optical microcavity on the performance of ITO-free polymer solar cells with WO_3/Ag/WO_3 transparent electrode" *Sol. Energy Mater. Sol. Cells* **2012**, *100*, 226.
[259] J.-F. Salinas, H.-L. Yip, C.-C. Chueh, C.-Z. Li, J.-L. Maldonado, A. K.-Y. Jen, "Optical design of transparent thin metal electrodes to enhance in-coupling and trapping of light in flexible polymer solar cells." *Adv. Mater.* **2012**, *24*, 6362.
[260] Y.-H. Chen, C.-W. Chen, Z.-Y. Huang, W.-C. Lin, L.-Y. Lin, F. Lin, K.-T. Wong, H.-W. Lin, "Microcavity-embedded, colour-tuneable, transparent organic solar cells" *Adv. Mater.* **2014**, *26*, 1129.
[261] Z.-Y. Huang, S.-W. Chiu, C.-W. Chen, Y.-H. Chen, L.-Y. Lin, K.-T. Wong, H.-W. Lin, "Spontaneous formation of light-trapping nano-structures for top-illumination organic solar cells" *Nanoscale* **2014**, *6*, 2316.
[262] D. S. Ghosh, R. Betancur, T. L. Chen, V. Pruneri, J. Martorell, "Semi-transparent metal electrode of Cu–Ni as a replacement of an ITO in organic photovoltaic cells" *Sol. Energy Mater. Sol. Cells* **2011**, *95*, 1228.

[263] S. Schubert, J. Meiss, L. Müller-Meskamp, K. Leo, "Improvement of transparent metal top electrodes for organic solar cells by introducing a high surface energy seed layer" *Adv. Energy Mater.* **2013**, *3*, 438.
[264] C. J. M. Emmott, A. Urbina, J. Nelson, "Environmental and economic assessment of ITO-free electrodes for organic solar cells" *Sol. Energy Mater. Sol. Cells* **2012**, *97*, 14.
[265] A. Kumar, C. Zhou, "The race to replace tin-doped indium oxide: which material will win?" *ACS nano* **2010**, *4*, 11.
[266] V. Bulovi, "Transform-limited, narrow-linewidth lasing action in organic semiconductor microcavities" *Science* **1998**, *279*, 553.
[267] S. Chen, L. Deng, J. Xie, L. Peng, L. Xie, Q. Fan, W. Huang, "Recent developments in top-emitting organic light-emitting diodes." *Adv. Mater.* **2010**, *22*, 5227.
[268] S. Dirr, S. Wiese, H.-H. Johannes, W. Kowalsky, "Organic electro- and photoluminescent microcavity devices" *Adv. Mater.* **1998**, *10*, 167.
[269] I. D. W. Samuel, G. a. Turnbull, "Organic semiconductor lasers." *Chem. Rev.* **2007**, *107*, 1272.
[270] H. F. Wittmann, J. Gruner, R. H. Friend, G. W. C. Spencer, S. C. Moratti, A. B. Holmes, "Microcavity effect in a single-layer polymer light-emitting diode" *Adv. Mater.* **1995**, *7*, 541.
[271] X. Guo, J. Lin, H. Chen, X. Zhang, Y. Fan, J. Luo, X. Liu, "Ultrathin and efficient flexible polymer photovoltaic cells based on stable indium-free multilayer transparent electrodes" *J. Mater. Chem.* **2012**, *22*, 17176.
[272] L. A. A. Pettersson, L. S. Roman, O. Inganäs, "Modeling photocurrent action spectra of photovoltaic devices based on organic thin films" *J. Appl. Phys.* **1999**, *86*, 487.
[273] A. J. Moulé, K. Meerholz, "Minimizing optical losses in bulk heterojunction polymer solar cells" *Appl. Phys. B* **2006**, *86*, 721.
[274] T. Ameri, G. Dennler, C. Waldauf, P. Denk, K. Forberich, M. C. Scharber, C. J. Brabec, K. Hingerl, "Realization, characterization, and optical modeling of inverted bulk-heterojunction organic solar cells" *J. Appl. Phys.* **2008**, *103*, 084506.
[275] M. C. Barr, R. M. Howden, R. R. Lunt, V. Bulović, K. K. Gleason, "Top-illuminated organic photovoltaics on a variety of opaque substrates with vapor-printed poly(3,4-ethylenedioxythiophene) top electrodes and MoO_3 fuffer layer" *Adv. Energy Mater.* **2012**, *2*, 1404.
[276] A. Hübler, B. Trnovec, T. Zillger, M. Ali, N. Wetzold, M. Mingebach, A. Wagenpfahl, C. Deibel, V. Dyakonov, "Printed paper photovoltaic cells" *Adv. Energy Mater.* **2011**, *1*, 1018.
[277] B. O'Connor, K. H. An, K. P. Pipe, Y. Zhao, M. Shtein, "Enhanced optical field intensity distribution in organic photovoltaic devices using external coatings" *Appl. Phys. Lett.* **2006**, *89*, 233502.
[278] G. H. Jung, K. Hong, W. J. Dong, S. Kim, J.-l. Lee, "BCP/Ag/MoO_3 transparent cathodes for organic photovoltaics" *Adv. Energy Mater.* **2011**, *1*, 1023.
[279] J. Meiss, M. Furno, S. Pfuetzner, K. Leo, M. Riede, "Selective absorption enhancement in organic solar cells using light incoupling layers" *J. Appl. Phys.* **2010**, *107*, 053117.
[280] S. Lim, D. Han, H. Kim, S. Lee, S. Yoo, "Cu-based multilayer transparent electrodes: A low-cost alternative to ITO electrodes in organic solar cells" *Sol. Energy Mater. Sol. Cells* **2012**, *101*, 170.

[281] M. W. Rowell, M. D. McGehee, "Transparent electrode requirements for thin film solar cell modules" *Energy Environ. Sci.* **2011**, *4*, 131.
[282] H. Jin, C. Tao, M. Velusamy, M. Aljada, Y. Zhang, M. Hambsch, P. L. Burn, P. Meredith, "Efficient, large area ITO-and-PEDOT-free organic solar cell sub-modules." *Adv. Mater.* **2012**, *24*, 2572.
[283] A. Karpinski, S. Berson, H. Terrisse, M. Mancini-Le Granvalet, S. Guillerez, L. Brohan, M. Richard-Plouet, "Anatase colloidal solutions suitable for inkjet printing: Enhancing lifetime of hybrid organic solar cells" *Sol. Energy Mater. Sol. Cells* **2013**, *116*, 27.
[284] S. Sista, Z. Hong, M.-H. Park, Z. Xu, Y. Yang, "High-efficiency polymer tandem solar cells with three-terminal structure" *Adv. Mater.* **2010**, *22*, E77.
[285] G.-M. Ng, E. L. Kietzke, T. Kietzke, L.-W. Tan, P.-K. Liew, F. Zhu, "Optical enhancement in semitransparent polymer photovoltaic cells" *Appl. Phys. Lett.* **2007**, *90*.
[286] Y.-J. Kang, D.-G. Kim, J.-K. Kim, W.-Y. Jin, J.-W. Kang, "Progress towards fully spray-coated semitransparent inverted organic solar cells with a silver nanowire electrode" *Org. Electron.* **2014**, 10.1016/j.orgel.2014.06.016.
[287] Y. J. Cheng, S. H. Yang, C. S. Hsu, "Synthesis of conjugated polymers for organic solar cell applications" *Chem. Rev.* **2009**, *109*, 5868.
[288] L. Gang, Z. Rui, Y. Yang, "Polymer solar cells" *Nat. Photonics* **2012**, *6*, 153.
[289] T. Ameri, G. Dennler, C. Waldauf, H. Azimi, A. Seemann, K. Forberich, J. Hauch, M. Scharber, K. Hingerl, C. J. Brabec, "Fabrication, optical modeling, and color characterization of semitransparent bulk-heterojunction organic solar cells in an inverted structure" *Adv. Funct. Mater.* **2010**, *20*, 1592.
[290] A. Colsmann, A. Puetz, A. Bauer, J. Hanisch, E. Ahlswede, U. Lemmer, "Efficient semi-transparent organic solar cells with good transparency color perception and rendering properties" *Adv. Energy Mater.* **2011**, *1*, 599.
[291] S. K. Hau, H.-L. Yip, H. Ma, A. K.-Y. Jen, "High performance ambient processed inverted polymer solar cells through interfacial modification with a fullerene self-assembled monolayer" *Appl. Phys. Lett.* **2008**, *93*, 233304.
[292] H.-L. Yip, S. K. Hau, N. S. Baek, A. K. Y. Jen, "Self-assembled monolayer modified ZnO/metal bilayer cathodes for polymer/fullerene bulk-heterojunction solar cells" *Appl. Phys. Lett.* **2008**, *92*, 193313.
[293] J. Zou, H.-L. Yip, Y. Zhang, Y. Gao, S.-C. Chien, K. O'Malley, C.-C. Chueh, H. Chen, A. K. Y. Jen, "High-performance inverted polymer solar cells: device characterization, optical modeling, and hole-transporting modifications" *Adv. Funct. Mater.* **2012**, *22*, 2804.
[294] S. K. Hau, H.-L. Yip, O. Acton, N. S. Baek, H. Ma, A. K.-Y. Jen, "Interfacial modification to improve inverted polymer solar cells" *J. Mater. Chem.* **2008**, *18*.
[295] H. Ma, H. L. Yip, F. Huang, A. K. Y. Jen, "Interface engineering for organic electronics" *Adv. Funct. Mater.* **2010**, *20*, 1371.
[296] H. L. Yip, A. K. Y. Jen, "Recent advances in solution-processed interfacial materials for efficient and stable polymer solar cells" *Energy Environ. Sci.* **2012**, *5*, 5994.
[297] N. Drolet, "Organic photovoltaic: efficiency and lifetime challenges for commercial viability", presented at *2012 MRS Spring Meeting & Exhibit*, San Francisco, CA, Moscone West Convention Center, Marriott Marquis, 2012.

[298] J. Meiss, T. Menke, K. Leo, C. Uhrich, W.-M. Gnehr, S. Sonntag, M. Pfeiffer, M. Riede, "Highly efficient semitransparent tandem organic solar cells with complementary absorber materials" *Appl. Phys. Lett.* **2011**, *99*, 043301.
[299] J.-M. Geusebroek, R. van den Boomgaard, A. W. M. Smeulders, T. Gevers, "Color constancy from physical principles" *Pattern Recogn. Lett.* **2003**, *24*, 1653.
[300] J. Schanda, *Colorimetry: Understanding the CIE System*, John Wiley & Sons, Inc., **2007** 71-73.
[301] Y. Sun, J. H. Seo, C. J. Takacs, J. Seifter, A. J. Heeger, "Inverted polymer solar cells integrated with a low-temperature-annealed sol-gel-derived ZnO Film as an electron transport layer" *Adv. Mater.* **2011**, *23*, 1679.